



TECHNISCHE  
UNIVERSITÄT  
WIEN  
Vienna University of Technology

D I P L O M A R B E I T

Characterisation of interstrip parameters  
on silicon sensors  
for the Belle II vertex detector

ausgeführt am

Institut für Hochenergiephysik  
der Österreichischen Akademie der Wissenschaften

unter Anleitung von

Univ.Doz. Dipl.-Ing. Dr.techn. Manfred KRAMMER

durch

Paul Dolejschi  
Josefstädterstraße, 1080 Wien

1. August 2012

---

Unterschrift

# Abstract

The BELLE II experiment at the SuperKEKB-Factory is designed to investigate CP violation in the quark sector. SuperKEKB is an asymmetric electron-positron collider, colliding 7.0 GeV and 4.0 GeV electrons and positrons. The innermost part of the BELLE II detector consists of a pixel detector (PXD) and the Silicon Vertex Detector (SVD). Both the PXD and the SVD consist of silicon detectors. In this diploma thesis, different electrical measurements on the prototypes of silicon strip detectors for the SVD were performed.

The author employed the Quality Test Center (QTC) at the HEPHY Vienna to develop new measurement methods for silicon strip sensors. The measurements of the *interstrip resistance* and the *interstrip capacitance* are new measurement methods that are subject to be incorporated into future quality assurance at the QTC.

The measurements were performed on barrel sensors from Hamamatsu Photonics and on wedge sensors from Micron Semiconductor. Two differently shaped sensor types are the result of the asymmetry of the SuperKEKB collider. Both sensor types are double sided silicon sensors, for the measurement of which the QTC has been designed. The author has developed three LabView run measurement methods to measure the interstrip resistance and has performed frequency dependent capacitance measurements, also LabView run, to determine the interstrip capacitance. The results of these measurements have been cross checked with specifications given in the *Belle II Technical Design Report* and compared to results of publications of similar measurements by different work groups. In addition, the author has investigated sensor related effects that influence the measurement and has tried to improve the measurement accuracy.

The findings of this diploma thesis will be important for future operation and improvement of the QTC Vienna, in order to perform quality assurance for serial production sensors, destined to be operated in high energy particle experiments all over the world. Also, they lie at the basis of better theoretical understanding of double sided silicon detectors.

Der Belle II Detektor des SuperKEKB Beschleunigers am Forschungszentrum für Hochenergiephysik in Tsukuba, Japan ist speziell für die Beobachtung von CP Verletzenden Prozessen von B-Mesonen ausgelegt. SuperKEKB ist ein Synchrotron, das Elektronen und Positronen auf jeweils 7.0 GeV und 4.0 GeV beschleunigt. Die innersten Schichten des BELLE II Detektors bilden Silizium-Halbleiterdetektoren, sowohl im Pixel Detektor (PXD), als auch im Silicon Vertex Detector (SVD). Hauptaugenmerk dieser Diplomarbeit war es, elektrische Messungen an Prototypen der Siliziumstreifendetektoren für den SVD durchzuführen.

Die Messungen wurden am Quality Test Center (QTC) am Institut für Hochenergiephysik (HEPHY) in Wien durchgeführt. Insbesondere wurden neue Messmethoden entwickelt und getestet. Die Messungen des *Zwischenstreifenwiderstandes* und der *Zwischenstreifenkapazität* wurden speziell für die QTC entwickelt, um aktiv zur zukünftigen Qualitätssicherung von Siliz-

iumdetektoren beizutragen.

Zwei Haupttypen von Sensoren von zwei unterschiedlichen Anbietern waren Gegenstand intensiver messtechnischer Untersuchungen. Aufgrund der Asymmetrie des SuperKEKB Beschleunigers besteht der SVD aus rechteckigen und trapezoiden Sensoren, welche von Hamamatsu Photonics und Micron Semiconductor gefertigt werden und zu den doppelseitigen Siliziumsensoren zählen. Verschiedene LabView-gestützte Messverfahren zur Bestimmung des Zwischenstreifenwiderstandes und frequenzabhängige Kapazitätsmessungen wurden zur Bestimmung der Zwischenstreifenkapazität wurden vom Autor entwickelt und durchgeführt. Die Ergebnisse wurden mit den Spezifikationen aus dem *Belle II Technical Design Report* und anderen Ergebnissen aus der Literatur verglichen. Im Zuge intensiver Messreihen sind auch diverse Sensor-spezifische Messeffekte untersucht und die Grenzen der Messgenauigkeit bestimmt und erweitert worden.

Die Resultate dieser Diplomarbeit werden in die Weiterentwicklung der QTC am HEPHY Wien und zur zukünftigen Qualitätssicherung von Siliziumstreifendetektoren für internationale Experimente der Hochenergiephysik einfließen. Sie liefern Außerdem die Motivation für tiefere theoretische Untersuchungen von doppelseitigen Siliziumstreifendetektoren.



# Contents

|          |   |           |
|----------|---|-----------|
| <b>1</b> | <b>Belle II</b>   | <b>7</b>  |
| 1.1      | Physics Motivation . . . . .  | 7         |
| 1.2      | SuperKEK-B . . . . .  | 7         |
| 1.3      | CP-Violation . . . . .  | 9         |
| 1.4      | The Belle II detector . . . . .                                     | 10        |
| 1.4.1    | Pixel Detector (PXD) . . . . .                                      | 11        |
| 1.4.2    | Silicon Vertex Detector (SVD) . . . . .                             | 12        |
| 1.4.3    | Central Drift Chamber (CDC) . . . . .                               | 12        |
| 1.4.4    | Electromagnetic Calorimeter (ECL) . . . . .                         | 12        |
| 1.4.5    | Kaon and Muon Detection System (KLM) . . . . .                      | 13        |
| 1.4.6    | Particle identification . . . . .                                   | 13        |
| <b>2</b> | <b>Silicon Vertex Detector</b>                                      | <b>15</b> |
| 2.1      | Introduction . . . . .  | 15        |
| 2.2      | Limitations . . . . .   | 15        |
| 2.3      | Detector Layout . . . . .   | 16        |
| 2.3.1    | Ladder design . . . . .   | 17        |
| <b>3</b> | <b>Double Sided Silicon Sensors of the BELLE II Vertex Detector</b> | <b>21</b> |
| 3.1      | Silicon Semiconductors . . . . .                                    | 21        |
| 3.2      | Doping . . . . .  | 23        |
| 3.3      | pn-junction . . . . .   | 26        |
| 3.4      | Working principle of semiconductor detectors . . . . .              | 27        |
| 3.4.1    | Capacitance . . . . .   | 28        |
| 3.4.2    | Segmentation . . . . .  | 28        |
| 3.4.3    | Bias resistor . . . . .   | 29        |
| 3.4.4    | AC coupling . . . . .   | 30        |
| 3.4.5    | Passivation Layer . . . . .   | 30        |
| 3.4.6    | Bond and probe pads . . . . .                                       | 30        |
| 3.4.7    | Metal overhang . . . . .  | 31        |
| 3.4.8    | Guard ring . . . . .  | 31        |
| 3.4.9    | Double sided silicon sensors . . . . .                              | 31        |
| 3.5      | DSSDs for the Belle II detector . . . . .                           | 33        |
| 3.5.1    | Barrel sensors . . . . .  | 34        |
| 3.5.2    | Forward sensors . . . . .   | 34        |

|          |  |           |
|----------|--|-----------|
| <b>4</b> | <b>Quality assurance at HEPHY Vienna</b>             | <b>37</b> |
| 4.1      | The QTC Vienna . . . . .                             | 37        |
| 4.2      | Measurement types . . . . .                          | 39        |
| 4.2.1    | Global scans . . . . .                               | 41        |
| 4.2.2    | Measurements on strips . . . . .                     | 43        |
| <b>5</b> | <b>Standard Measurements performed with the QTC</b>  | <b>47</b> |
| 5.1      | Hamamatsu 2nd batch . . . . .                        | 47        |
| 5.1.1    | Global Measurements . . . . .                        | 47        |
| 5.1.2    | Stripskans . . . . .                                 | 47        |
| 5.2      | Micron . . . . .                                     | 49        |
| 5.2.1    | Global Measurements . . . . .                        | 49        |
| 5.2.2    | Stripskans . . . . .                                 | 49        |
| 5.3      | Conclusion . . . . .                                 | 53        |
| <b>6</b> | <b>Interstrip resistance</b>                         | <b>57</b> |
| 6.1      | Diode characteristics . . . . .                      | 60        |
| 6.2      | Interstrip Resistance Measurements . . . . .         | 64        |
| 6.2.1    | Method 1 . . . . .                                   | 64        |
| 6.2.2    | Method 2 . . . . .                                   | 68        |
| 6.2.3    | Method 3 . . . . .                                   | 72        |
| 6.3      | Conclusion . . . . .                                 | 76        |
| <b>7</b> | <b>Interstrip capacitance</b>                        | <b>81</b> |
| 7.1      | Measurement principle . . . . .                      | 81        |
| 7.1.1    | Frequency dependent capacitance measurement. . . . . | 81        |
| 7.2      | Measurements . . . . .                               | 82        |
| <b>8</b> | <b>Summary and Outlook</b>                           | <b>93</b> |
| <b>A</b> | <b>Stripskans of section 5</b>                       | <b>95</b> |
| A.1      | Hamamatsu 2nd batch . . . . .                        | 95        |
| A.2      | Micron 1st batch . . . . .                           | 99        |

# Chapter 1

## Belle II

### 1.1 Physics Motivation

At the current level of experimental precision, the Standard Model (SM) is one of the best verified physics theories. Its ultimate aim is to explain the basic forces of nature and the interaction between each of the elementary particles.

Physicists today assume that the known matter consists of Leptons and Quarks, while the interactions between those are mediated by so called gauge bosons. They can be regarded as the "force carriers" of the fundamental interactions, which are the strong, the weak and the electromagnetic force. The SM consists of six Leptons and six Quarks. In advance, each of those "fundamental particles" has its associated anti-particle.

Although the SM includes just as much particles as anti-particles, it is without any doubt that the known universe is matter-dominated. To this day, the so called CP-violation is regarded to be responsible for this. The SM describes CP-violation within the Quark sector, but still it falls short to explain the matter-dominated universe, because the observed CP-asymmetry is many orders of magnitude too small.

Future experiments in high energy physics aim to answer questions that still arise from the SM, like the one discussed above. Therefore, complementary approaches are used. On one hand, there is the energy frontier, being dealt with at CERN<sup>1</sup>. On the other hand, and this is where the BELLE II experiment at Super KEK-B shall be introduced, there is the rare/precision frontier<sup>2</sup>. While at the energy frontier new particles may be produced, the approach of the rare/precision frontier is to obtain signatures of new particles through measurements of flavour<sup>3</sup> physics reactions at lower energies. Any deviation from the SM prediction can be interpreted in terms of New Physics (NP) models.

### 1.2 SuperKEK-B

SuperKEKB is an upgrade to the KEKB factory at the High Energy Accelerator Research Organisation (KEK) in Tsukuba, Japan, which has been operating since 1998 and had been shut down in June 2010.

KEK-B was an asymmetric electron-positron collider, consisting of two storage rings for electrons and positrons at the energies of 8.0 GeV and 3.5 GeV, respectively. The circumferential length

---

<sup>1</sup>The ATLAS and CMS experiments at the Large Hadron Collider (LHC)

<sup>2</sup>"rare" and "precision" refer to processes that are strongly suppressed or not allowed

<sup>3</sup>"flavour" is a quantum number related to the weak interaction of quarks

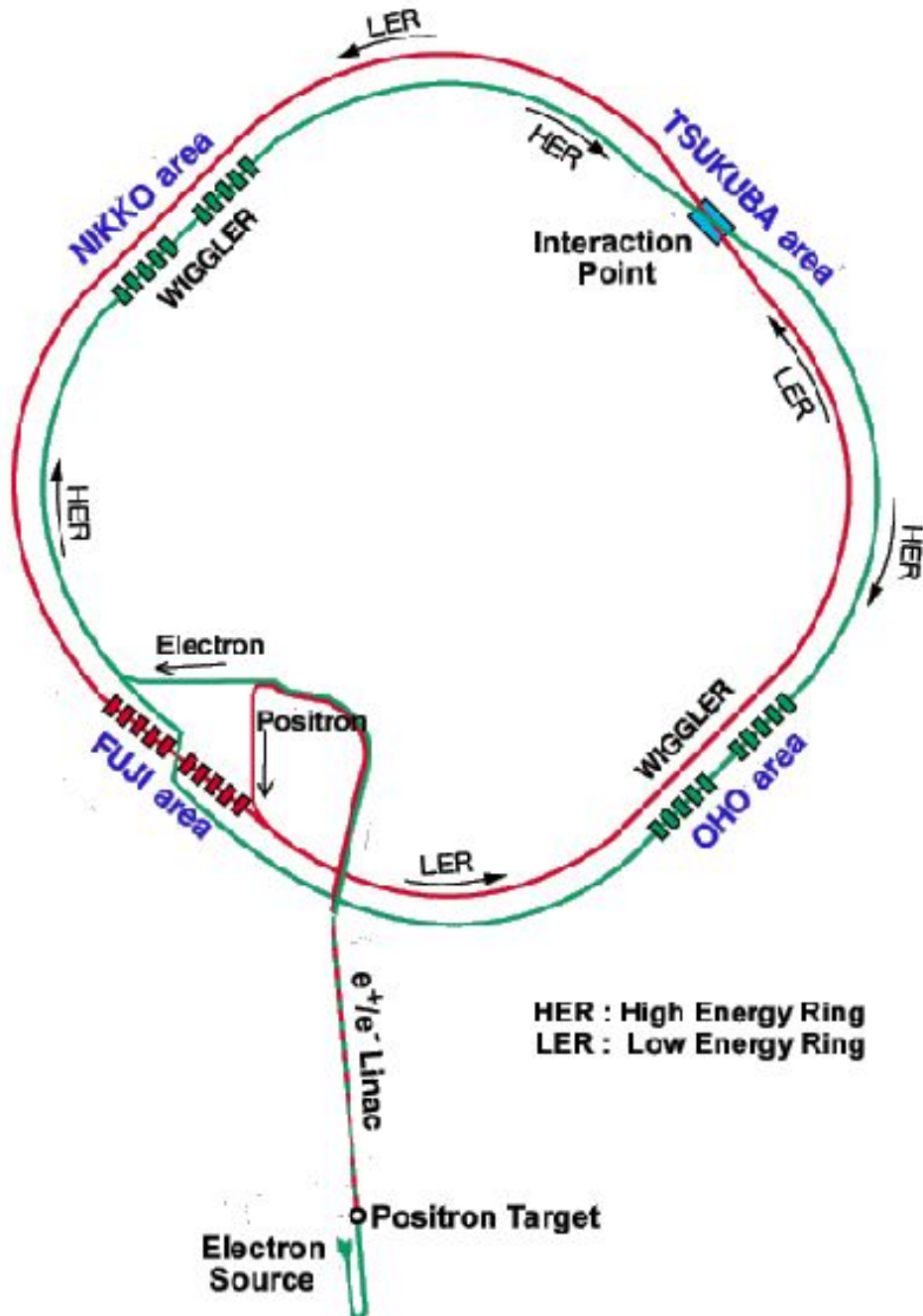


Figure 1.1: The KEKB collider



is 3016 m. It is called B-factory since massive amounts of B-Mesons<sup>4</sup> were produced by means of colliding the electron and the positron beam. After being brought to full energies in a linear accelerator system, the electrons and positrons are injected into the synchrotrons, which are also called HER (High Energy Ring, for 8 GeV electrons) and LER (Low Energy Ring, for the positrons). In the *Tsukuba experimental Hall*, the two beams are brought to collision. Here, around the collision point, the Belle detector is installed.

The KEKB collider was designed to obtain a peak *luminosity* ( $\alpha$ ) of more than  $10^{34} \text{ cm}^{-2} \text{ s}^{-1}$ , which was reached in November 2006<sup>5</sup>. The luminosity of a particle collider is one of the defining parameters of the *rate of reaction*

$$R = \sigma\alpha, \tag{1.1}$$

where  $\sigma$  denotes the cross section of the interaction region at the collision point.

The luminosity is mainly determined by the three fundamental parameters: the total beam current ( $I$ ), the vertical beam-beam parameter ( $\xi_y$ ) and the vertical beta function at the interaction point ( $\beta_y^*$ ).

KEKB-Factory will be upgraded to SuperKEKB using the same tunnel as KEKB. The upgrade is based on the "Nano-Beam" scheme, the basic idea of which is to squeeze the vertical beta function at the Interaction Point ( $\beta_y^*$ ) by minimizing the longitudinal size of the overlap region of the two beams at the interaction point (IP), which generally limits the effective minimum value of ( $\beta_y^*$ ) through the "hourglass effect"[1].

The luminosity goal of SuperKEKB is  $80 * 10^{34}$ , which is 40 times larger than the luminosity of its predecessor, and the fundamental parameters have to be chosen differently than at the old KEKB, especially ( $\beta_y^*$ ) and the beam currents, which will be increased by a factor of more than two.

### 1.3 CP-Violation

As discussed in the first section, violation of CP-symmetry is of highly interest for today's high energy physics. A CP transformation is a combined inversion of charge (C) and parity (P). The C operation reverses the charge of a given particle, thus it turns it into it's antiparticle, while the P operation revolves the direction of all coordinates of the position vector. Naively one would assume that the CP is conserved, but in 1964 Christenson, Cronin, Fitch and Turlay found CP-violation in the decay of K mesons[2].

In terms of the SM, Makoto Kobayashi and Toshihide Maskawa gave a theoretical explanation of CP violation in 1973[3]. The so called Cabibbo-Kobayashi-Maskawa-matrix (CKM), an unitary  $3 \times 3$  matrix, describes the transitions between different generations of quarks, even more importantly, it offers the source of CP-violation.

The SM consists of three generations of leptons and quarks:

$$\begin{pmatrix} \nu_e \\ e \end{pmatrix} \begin{pmatrix} \nu_\mu \\ \mu \end{pmatrix} \begin{pmatrix} \nu_\tau \\ \tau \end{pmatrix} \tag{1.2}$$

$$\begin{pmatrix} u \\ d \end{pmatrix} \begin{pmatrix} c \\ s \end{pmatrix} \begin{pmatrix} t \\ b \end{pmatrix} \tag{1.3}$$

---

<sup>4</sup>Mesons are non-elementary particles consisting of an even number of quarks and antiquarks. The B-Meson is composed of a b-antiquark and either an u- or a d-quark.

<sup>5</sup>A peak luminosity of  $1.712 * 10^{34} \text{ cm}^{-2} \text{ s}^{-1}$  was achieved

To obtain the mass eigenstates, which are linear combinations of the flavour eigenstates, latter are rotated by the CKM Matrix  $V_{CKM}$ :

$$\begin{pmatrix} V_{ud} & V_{us} & V_{ub} \\ V_{cd} & V_{cs} & V_{cb} \\ V_{td} & V_{ts} & V_{tb} \end{pmatrix} \begin{pmatrix} d \\ s \\ b \end{pmatrix} = \begin{pmatrix} d' \\ s' \\ b' \end{pmatrix}. \quad (1.4)$$

The unitarity condition applied to the first and the third columns yields

$$V_{ud}V_{ub}^* + V_{cd}V_{cb}^* + V_{td}V_{tb}^* = 0. \quad (1.5)$$

This relation can be depicted in the complex plane as seen in Figure 1.2. It was the primary

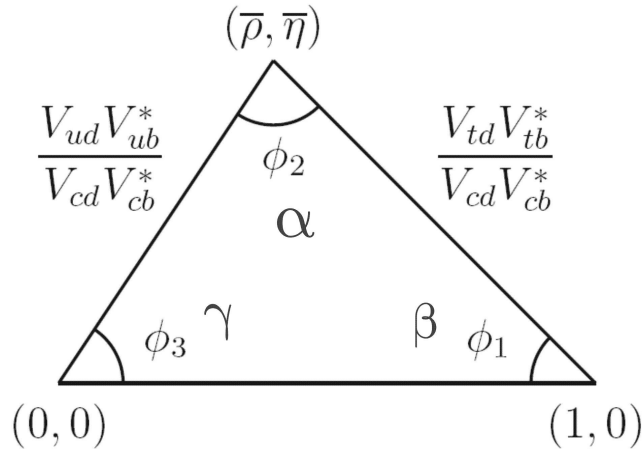


**Figure 1.2:** Unitarity Triangle

motivation of the Belle experiment to get information on the angles of the unitarity triangle by measuring CP violating effects in neutral B meson decays.  $\phi_1$ ,  $\phi_2$  and  $\phi_3$  represent the complex phase of the combinations

$$\phi_1 = \arg \left[ \frac{V_{cd}V_{cb}^*}{V_{td}V_{tb}^*} \right], \phi_2 = \arg \left[ \frac{V_{td}V_{tb}^*}{V_{ud}V_{ub}^*} \right], \phi_3 = \arg \left[ \frac{V_{ud}V_{ub}^*}{V_{cd}V_{cb}^*} \right], \quad (1.6)$$

and therefore are the sources of CP violation.

## 1.4 The Belle II detector

Belle II will bring the investigation of CP violating effects in B meson decays to a completely new level of sensitivity. Moreover, at the Super B factory physicists will not only be able to perform measurements of B meson decays, but charm physics,  $\tau$  lepton physics, spectroscopy and pure electroweak measurements will be performed. Some of the changes to Belle that will lead to an improved performance of Belle II shall now be mentioned [1].

- Just outside the beam pipe, the silicon strip detector is replaced by a two-layer silicon pixel.

- The silicon strip detector extends from just outside the pixel detector to a larger radius than in Belle.
- The central tracking device - a large volume drift chamber - has smaller drift cells than in Belle, starts just outside the expanded silicon strip detector, and extends to a larger radius.
- The Vertex resolution is improved by the excellent spatial resolution of the two innermost pixel detector layers.

Belle II consists of several sub-detector components:

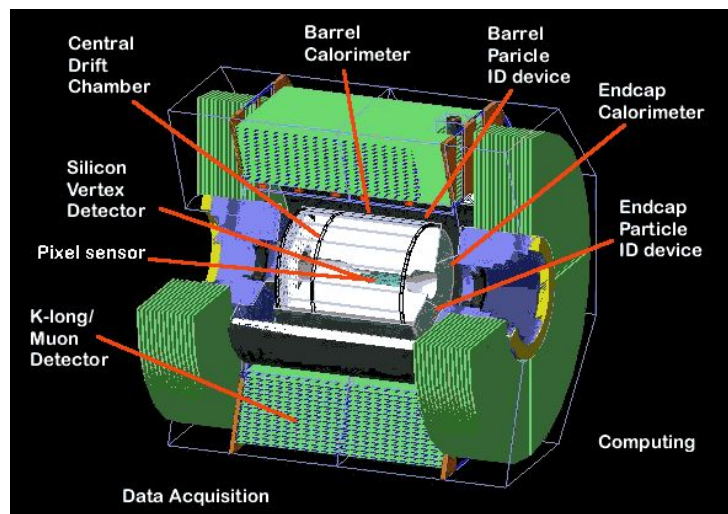


Figure 1.3: The Belle 2 detector and its sub-components

#### 1.4.1 Pixel Detector (PXD)

Due to the high luminosity of SuperKEKB, detectors close to the beam pipe are exposed to extremely high hit rates caused by the beam related background. Because of the large occupancy, the innermost layers of a high precision vertex detector cannot be realized by strip detectors. Therefore, *pixel sensors* are used, because they offer a much larger number of channels and consequently a smaller number of occupancy<sup>6</sup>. At SuperKEKB luminosities strip detectors can be used beyond radii of 40 mm [1].

To keep the material budget low and avoid multiple scattering, for BELLE II very thin pixel sensors are required. Hence, DEPFET (DEPLETED Field Effect Transistor) technology is used which allows for thicknesses down to 50  $\mu\text{m}$ . A DEPFET is a semiconductor detector that combines detection and amplification within one device. The readout electronics, which require active cooling, are located outside the acceptance region and do not contribute to the multiple scattering material budget. Due to internal amplification, the pixel sensors themselves are a low power device and therefore air cooling is sufficient [1].

Consisting of a fully depleted silicon bulk, a DEPFET pixel is equipped with a p-channel MOSFET structure with an internal gate where the electrons created by traversing charged particles, are collected, see figure 1.4. When the transistor is switched on, the electrons accumulated at

<sup>6</sup>The average percentage of strips with a signal above threshold at any trigger [1]

the internal gate modulate the channel current. The removal of collected charges, by a punch-through from a neighboring  $n^+$  contact, is called "clear".

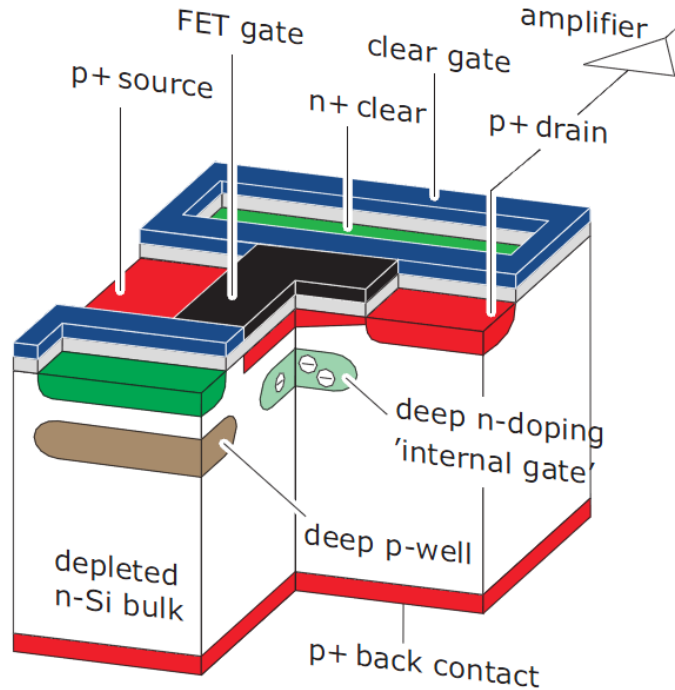


**Figure 1.4:** Operation principle of a DEPFET [1].

### 1.4.2 Silicon Vertex Detector (SVD)

The *silicon vertex detector* will be discussed in section 2.

### 1.4.3 Central Drift Chamber (CDC)

The working principle of a drift chamber is to measure the time between a particle incident and the arrival of the charge carrier cloud at an anode wire. The primary particle incident is determined using a scintillation counter at the entrance of the drift chamber. The spacial resolution of the BELLE II CDC is expected to be  $100 \mu\text{m}$ . The CDC of the BELLE II detector plays three important roles.

- It offers a precise measurement of momentas and tracks of charged particles.
- By measuring of energy loss within it's gas volume, it provides particle identification information. Low energy tracks that don't make it to the particle identification device can be determined by using the CDC alone.
- Last but not least, it provides efficient and reliable trigger signals for charged particles.

### 1.4.4 Electromagnetic Calorimeter (ECL)

The ECL's task is to detect photons from B meson decays. Since they are produced in a wide energy range, from 20 MeV to 4 GeV, a good resolution in energy and position is demanded

and make the ECL a very important part of the Belle II detector. It consists of an array of thallium-doped cesium iodide crystals (CSI(TI)).

A charged particle deposits its whole energy in the crystals and light is emitted, the intensity of which is measured by photodiodes.

#### 1.4.5 Kaon and Muon Detection System (KLM)

The outermost subsystem of the Belle II detector, which the KLM represents, is designated to detect myons and  $K_L^0$  mesons. Both of them are not seen by any other subsystems.  $K_L^0$  mesons because they are electrically neutral, and Myons due to their much bigger mass than electrons. The Belle II KLM is based on Glass-electrode-resistive plate chambers (RPCs). They consist of two parallel plate electrodes with very high bulk resistivity ( $5 \times 10^{12} \Omega$ ), separated by a gas-filled gap. In the strong electric field, an ionizing particle leads to a streamer between the electrodes and the electrode charge in the spot nearest the streamer then flows across the gas-filled gap, momentarily reducing the electric field there[1]. External pickup strips detect the location and time of the local ionisations, multiple layers of charged particle detectors and iron make it possible to discriminate between muons and kaons. The iron plates provide 3.9 interaction lengths or more of material which allow  $K_L$  mesons to shower hadronically.

#### 1.4.6 Particle identification

##### Barrel Region

For the Belle II upgrade, the present time-of-flight (TOF) and aerogel Cherenkov counters<sup>7</sup> in the barrel region of the Belle detector are replaced by time-of-propagation (TOP) counters, where the time-of-propagation of internally reflected photons inside a quartz radiator is measured. The Cherenkov image is then reconstructed from the 3-dimensional information provided by two coordinates (x,y) and precise timing, which is determined by micro-channel plate (MCP) PMTs at the end surfaces of the quartz bar[1].

##### End-Cap

To separate kaons from pions, the proximity-focusing Aerogel Ring-Imaging Cherenkov detector (ARICH) has been designed. It consists of an aerogel radiator, where Cherenkov photons are produced and an array of position sensitive photon detectors including a read-out system, respectively. The length of the detector is fixed to several centimeters to ensure that enough photons (about 10) can be detected for each ring image.

The silica aerogel Cherenkov radiator should be highly transparent in order not to lose photons inside the medium via Rayleigh scattering or absorption[1]. For photon detection, square-shaped HAPDs (hybrid avalanche photon detector) are used. Cherenkov photons enter the HAPD and generate photoelectrons from a photocathode. Afterwards, they are accelerated towards pixelated APDs, where an additional gain of about 40 is achieved.

---

<sup>7</sup>Cherenkov counters utilize the effect of mass-dependent threshold energy of Cherenkov radiation

#### 1.4. *THE BELLE II DETECTOR*

## Chapter 2

# Silicon Vertex Detector

### 2.1 Introduction

The Belle II SVD, as well as the PXD and the CDC, are employed to measure the two B decay vertices for the measurement of mixing-induced CP violation. Low mass, high precision, immunity to background hits, radiation tolerance and long-term stability are the good characteristics that were already provided by Belle's SVD2 and are inherited by the Belle II SVD.

In order to achieve a luminosity of  $8 \times 10^{35} \text{ cm}^{-2} \text{ s}^{-1}$ , small beta functions and low emittances at the IP are demanded and the 4GeV (LER) and 7GeV (HER) colliders fulfill these requirements. These energies result in a Lorentz boost factor of the center-of-mass-system of  $\beta\gamma = 0.28$ , which actually makes about two-thirds of that in Belle. As a matter of fact, the separation of the B vertices in an event at Belle II is smaller than in Belle. To keep the vertex measurement performance of Belle II as good as or better than that of its predecessor, the radius of the beam pipe at the interaction region is supposed to be 10mm. Two thirds of that in KEKB, consequently.[1]

Here are some main characteristics of the Belle II SVD:[1]

- The sensor on rib design was chosen, which means that the sensors are glued to so called *ladders* (See section 2.3.1).
- The inner and outer radii are 38 mm and 140 mm, respectively. They are determined by the radii of the PXD and the CDC.
- The full Belle II angular acceptance of  $17^\circ < \Theta < 150^\circ$  is covered
- The reconstruction of charged tracks is improved compared to the Belle SVD
- Tracks reconstructed in the CDC can be extrapolated with high efficiency to the PXD
- The hit occupancy has to be less than 10%. This is necessary for the association of reconstructed tracks in the CDC with correct hits in the drift chamber. Information from the SVD can also be used to eliminate background hits in the PXD.
- A cooling system is employed to dissipate its heatload

### 2.2 Limitations

The estimated occupancy of the SVD2 in the SuperKEKB environment is shown in figure 2.1. The hit occupancy, according to this estimation, is too high by a factor of ten<sup>1</sup>. Therefore, the

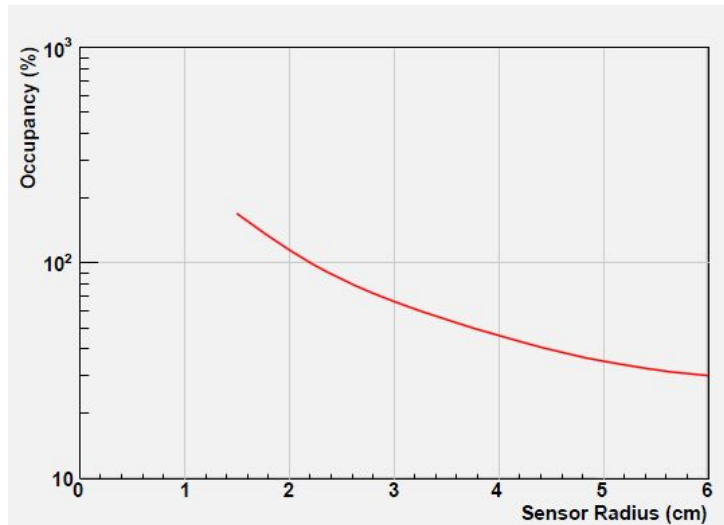


*Figure 2.1: Expected occupancy of the SVD2 at SuperKEKB[1]*

innermost sensor layer of the Belle II SVD is determined to be placed at a radius of 3.8 cm. The outermost layer will be at a radius of 13.5 cm, taking into account that the background level at radii 10cm is too high for a central drift chamber.

Due to high cost and channel count, which would make it difficult to instrument this volume with a PXD, four layers of double-sided silicon strip detectors, fabricated from six inch wafers, are used. The usage of large wafers also helps to keep the overall material budget as low as possible. To achieve a low input capacitance of the APV25 readout chips<sup>2</sup>, the hybrids will be mounted directly onto the DSSDs. The material budget per DSSD ladder will be 0.57% of radiation length after the optimisation of both, the readout chips and the ladders. The DSSD sensor itself will contribute 0.32%. Most particle tracks will suffer multiple scattering, due to the rather low energies of SuperKEKB. Instead of a high precision alignment, which would only be possible with highly energetic cosmic muons whose rate is limited, an overlap of different layers - at the cost of the overall material budget - to facilitate alignment, is permitted. [1].

## 2.3 Detector Layout

Since the radial coverage is almost twice as large as that of the Belle SVD2, a much larger number of wafers in a traditional cylindrical geometry would have to be used. Slanted sensors in the forward region, which result in the lantern shape of the Belle II SVD, have been considered to be a better solution. A trapezoidal shape of the sensors in the forward region is the result, where only one design for all layers is determined to be used. Due to the trapezoidal shape, the sensors in the forward region happen to have non-parallel strips and therefore the slant angle is supposed to vary in such a way that all of the non-parallel strips still intersect with the beam pipe. Because of the windmill structure of the Belle II SVD, this condition cannot exactly be fulfilled. The polar angular acceptance, which is asymmetric and ranges from  $17^\circ$  to  $150^\circ$ , takes account for the forward boost of the center-of-mass frame.

Table 2.1 lists the amount of sensors, ladders, and readout chips for each of the four layers of the Belle II SVD. The achievable sensor size in six-inch wafer technology and the possibilities

<sup>1</sup>a sensor size of  $2.5\text{cm} \times 7.5\text{cm}$  was assumed here

<sup>2</sup>noise considerations and fast shaping are taken into account here



of fitting integer multiples within the acceptance region thereof as well heavily influences the geometry [1].

| Layer | Radius(mm) | Ladders | Sensors/ladder | Sensors | RO chips/sensor | RO chips |
|-------|------------|---------|----------------|---------|-----------------|----------|
| 6     | 140        | 17      | 5              | 85      | 10              | 850      |
| 5     | 115        | 14      | 4              | 56      | 10              | 500      |
| 4     | 80         | 10      | 3              | 30      | 10              | 300      |
| 3     | 38         | 8       | 2              | 16      | 12              | 192      |
| sum   |            | 40      |                | 187     |                 | 1902     |

**Table 2.1:** Geometrical properties of the Belle II SVD [1]

Layer 3 represents the innermost layer of the SVD, layer numbers  $< 3$  would refer to PXD layers.

The chip-on-sensor concept, also called *Origami*, due to the pitch adapters being bent around the sensor edge, will be used on all sensors except for those located at the edge of acceptance. In a windmill structure such as the Belle II SVD, these bent fanout pieces can only be applied at the outer sides, as seen in figure 2.2 [1].

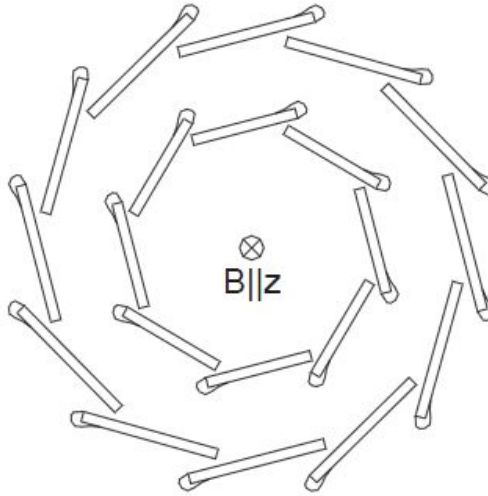


**Figure 2.2:** Cross-section of a windmill structure with Origami modules

### 2.3.1 Ladder design

As B physics is carried out at rather low energies, high precision track measurement is required due to multiple scattering. Consequently a very low mass but stiff mechanical structure is needed. The asymmetry in energy even further complicates the matter, since it leads to an asymmetric detector layout with slanted sensors in the forward region. The angle between the horizontal and the slanted sensors leads to a torque on the structure.

The chip-on-sensor concept (Origami) furthermore limitates the possibilities of how a support structure can be attached. The sensor on rib design is regarded to be the best solution here, with the ribs being made from lightweight matherials in order to keep the material budget as low as possible. Each rib consits of a Rohacell core with thin layers of carbon fiber to guarantee even

### 2.3. DETECTOR LAYOUT

more stiffness. The overall thickness of the ribs is 3.13 mm, with the two CF layer contributing  $65 \mu\text{m}$  each, while the height is 6.5 mm. This results in a "sandwich"- like design of the ribs. The Origami sensors are glued onto two of these composite sandwich carbon fiber ribs (SCFR), which form so called *ladders*, see fig. 2.3. Special care is taken that no bond wires are damaged and shorts are avoided. A 2mm gap between the sensor and the CF ribs is implemented in order to permit any contact of the structure and the sensor and rectangle silhouettes cut in the Rohacell core create the sensor distancing structure (SDS), see fig. 2.4. Table 2.2 shows the

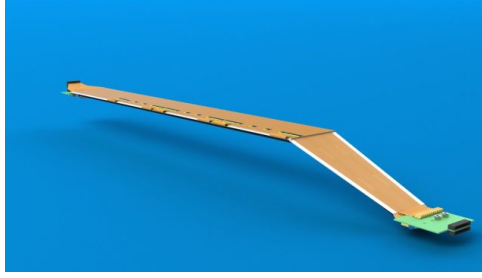


**Figure 2.3:** Ladder with DSSDs mounted on top. View from the trapezoidal shape of the sensors in the slanted forward region.

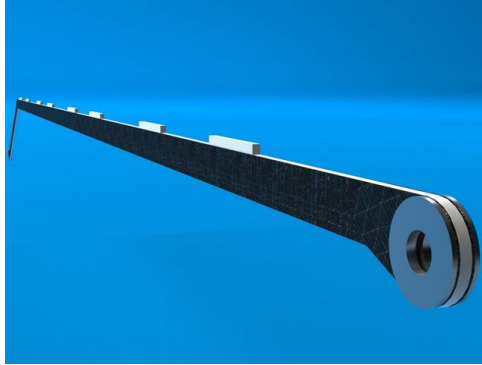


**Figure 2.4:** Composite sandwich rib of layer 6. The Rohacell core is supported by CF layers, SD structures on top.

ladder dimensions. The Ladder of layer 3 is of straight design, thus it does not have a slant angle nor a height.

| Layer | Ladder length(mm) | Ladder height | Slant angle ( $^{\circ}$ ) |
|-------|-------------------|---------------|----------------------------|
| 6     | 645.3             | 50            | 21.1                       |
| 5     | 515.6             | 37            | 17.2                       |
| 4     | 390.4             | 25            | 11.9                       |
| 3     | 262               | 0             | 0                          |

**Table 2.2:** Ladder dimensions [1]

While in the SVD2 of the original Belle detector an extra CF Bridge connected the two ribs of each ladder, mechanical simulations for the Belle II SVD have shown that the stiffness of the DSSDs themselves is sufficient to distribute the loads between the two ribs [1]. Figure 2.5 showcases the results of simulations of the mechanical stability. The sensors suffer from different

CHAPTER 2. SILICON VERTEX DETECTOR

gravitational sags, depending whether the ladder is loaded from above ( $108 \mu\text{m}$ ) or from the side ( $48 \mu\text{m}$ ). Although initially intended, the sags of the horizontal and the vertical position do not equal each other. To achieve this, a Rohacell core width of  $2\text{mm}$  would have been necessary, but the market's standard offer is  $3\text{mm}$ . A mismatch of the coefficient of thermal expansion

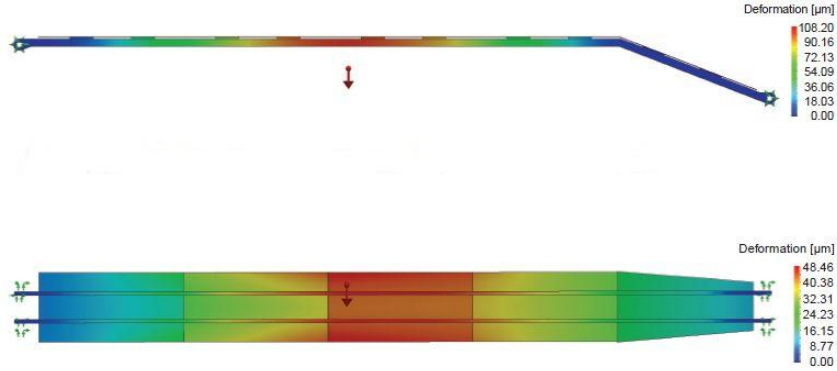


**Figure 2.5:** Gravitational sag of the DSSDs in horizontal and vertical position [1]

(CTE) between materials of different kinds normally would be expected to cause additional mechanical stress on the structure. The CTE of the Rohacell core ( $30 \times 10^{-6} K^{-1}$ ) and the Sensors ( $2.6 \times 10^{-6} K^{-1}$ ) indeed mismatch by a factor of more than 10, while the CTE of the CF layer appears to be negative ( $-0.5 \times 10^{-6} K^{-1}$ ). Still, thermal induced mechanical stress or risk of misaligning is not expected, due to the fact that the contact area of the sensors and the ribs are kept as short as possible ( $20 \text{ mm}$ ) and the total thermal expansion of both, the Rohacell and the CF, is below  $10 \mu\text{m}$  distributed over  $650\text{mm}$ . The Rohacell layers are expected to absorb these small variations in length [1].

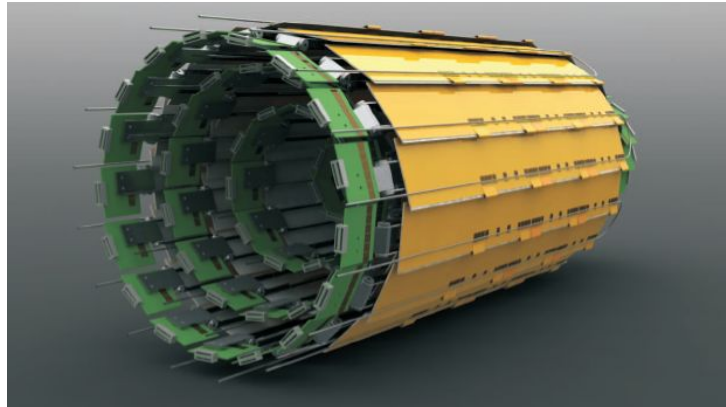


**Figure 2.6:** Rendering of all four layers of the Belle II SVD. Cooling lines and hybrids are also visible. [1]

### 2.3. DETECTOR LAYOUT

## Chapter 3

# Double Sided Silicon Sensors of the BELLE II Vertex Detector

### 3.1 Silicon Semiconductors

Pure Silicon (Si) is the eighth most common element in the universe with atomic number 14 and is located in the fourth main group of the periodic table. Hence, it has 4 covalent-bonded electrons in the outer shells. A pure silicon solid state forms a face centered cubic structure (fcc) with a lattice spacing of  $a = 5.43\text{\AA}$ , as seen in Fig. 3.1.

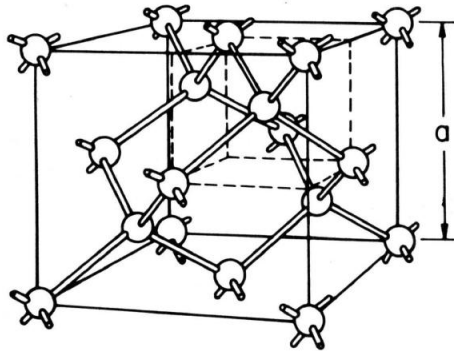


*Figure 3.1: The face centered cubic structure of a silicon unit cell and lattice parameter  $a$  [4]*

Due to the periodic structure of a pure solid state lattice, there is the formation of an electronic band structure. The electrons of periodic lattice atoms only occupy certain energy levels, which are referred to as *energy bands*. In between those bands, there are energy levels which the electrons may not occupy, called *gaps*. The outermost occupied energy band is called *valence band*, while the innermost unoccupied band is called *conduction band*. The gap  $E_G$  between the valence- and the conduction band is the defining parameter of a solid concerning its electrical resistivity. The gap is measured in terms of energy, usually electronvolts. The gap is defined by the difference of the edges of the valence- and the conduction band.

$$E_G = E_C - E_V, \quad (3.1)$$

with  $E_C$  being the lower edge of the conduction band and  $E_V$  denoting the upper edge of the valence band, respectively.

If there is no gap between the valence- and the conduction band or are they overlapping, the

### 3.1. SILICON SEMICONDUCTORS

material is called *conductor*, otherwise, if there's a rather large gap (usually  $> 5\text{eV}$ ), it's considered to be an *insulator*. For *semiconductors* instead, the size of the gap allows the resistance to be temperature or radiation dependent. Fig. 3.2 shows the energy levels and the band gap for different materials. In silicon, the energy gap is **1.12 eV**. This allows electrons to flip from the

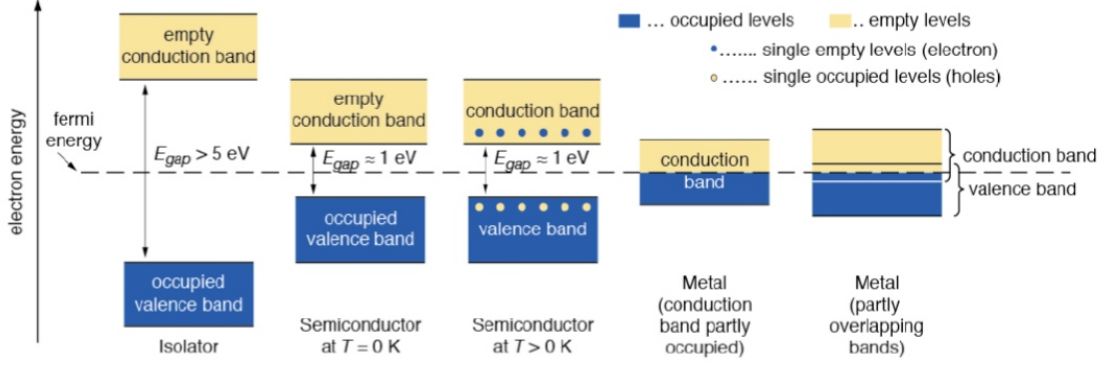


**Figure 3.2:** Valence-, conduction band and energy gap for insulators, semiconductors and conductors[5]

valence band to the conduction band when they are excited by *phonons*. Phonons are collective excitations in solids, also referred to as *quasiparticles*, caused by finite temperatures. This leads to a temperature dependent resistivity, since the number of electrons in the conduction band is temperature dependent.

Electrons in the conduction band can be regarded as free particles, with an *effective mass* which is different from elementary electrons. To obtain the *intrinsic charge carrier concentration*  $n_i$ , which is the number of charge carriers available when thermal equilibrium is reached at a certain temperature, one has to build a convolution of the *state density* for electrons at the bottom of the conduction band and the *occupation probability*.

- The state density  $N(E)$  describes the number of states per interval of energy at each energy level that are available to be occupied by the charge carriers. Within one energy band, these states are continuous.

$$N_e(E) = \frac{(2m_e^*)^{3/2}}{2\pi^2\hbar^3} \sqrt{E - E_C} \quad (3.2)$$

A similar equation holds true for *holes*. When an electron is excited, it leaves behind a hole, which then can be regarded to be a positive charge carrier that translates through the lattice with a corresponding effective mass.

$$N_h(E) = \frac{(2m_h^*)^{3/2}}{2\pi^2\hbar^3} \sqrt{E_V - E} \quad (3.3)$$

- The Fermi-Dirac function  $F(E)$  yields the probability that a certain energy state is occupied, hence it gives the occupation probability.

$$F_e(E) = \frac{1}{1 + \exp\left(\frac{E - E_F}{k_B T}\right)} \quad (3.4)$$

$$F_h(E) = \frac{1}{1 + \exp\left(\frac{E_F - E}{k_B T}\right)} \quad (3.5)$$

## CHAPTER 3. DOUBLE SIDED SILICON SENSORS OF THE BELLE II VERTEX DETECTOR

$E_F$  denotes the *Fermi energy level*. At this energy, the occupation probability is one half. For insulators and semiconductors,  $E_F$  is located in the band gap, while for metals it is in the conduction band.  $T$  and  $k_B$  are the Boltzmann constant and temperature,  $m_*$  is the effective mass of the electrons and holes.

The free electron density can now be written as

$$n = \int_{E_C}^{+\infty} N_e(E) \cdot F_e(E) dx = n_0 \cdot \exp\left(-\frac{E_C - E_F}{k_B T}\right), n_0 = 2 \cdot \left(\frac{2\pi m_*^e k_B T}{\hbar}\right)^{3/2} \quad (3.6)$$

Again, a similar equation holds true for holes.

$$n = \int_{E_0}^{E_V} N_h(E) \cdot F_h(E) dx = n_0 \cdot \exp\left(-\frac{E_F - E_V}{k_B T}\right), p_0 = 2 \cdot \left(\frac{2\pi m_*^h k_B T}{\hbar}\right)^{3/2} \quad (3.7)$$

If under thermal equilibrium the free charge carrier concentration of electrons equals the concentration of holes, the semiconductor is called intrinsic.

$$n_i = n = p \quad (3.8)$$

Thus,  $n_i$  becomes

$$n_i = \sqrt{n \cdot p} = \sqrt{n_0 \cdot p_0} \exp\left(-\frac{E_g}{2k_B T}\right), \quad (3.9)$$

which equals  $1.45 \times 10^{10} \text{ cm}^{-3}$  charge carriers at  $T = 300\text{K}$ .

Furthermore, the Fermi energy level can now be obtained. As mentioned before, for semiconductors it is located in between the valence- and the conduction band, hence in the gap.

$$E_F = \frac{E_C + E_V}{2} + \frac{3}{4} k_B T \ln\left(\frac{m_*^h}{m_*^e}\right) \quad (3.10)$$

### 3.2 Doping

The concentration of free charge carriers in a semiconductor holds responsible for its electrical properties. Equation 3.9 yields that the concentration depends exponentially on the band gap  $E_g$ . By incorporating elements from the neighbouring groups of the periodic table into the silicon lattice, intermediate energy states will occur in the band gap and the Fermi energy level is shifted towards the edges of the valence- or the conduction band.

Elements of group  $\overline{\text{III}}$  of the periodic table provide three, while elements from group  $\overline{\text{V}}$  deliver five electrons for covalent binding. Consequently, two different types of semiconductors can be developed by doping with *acceptors* or *donators*, as shown in figure 3.3.

- N-type semiconductor:  
Atoms that provide one valence electron more than the bulk material are called donators. Within the periodic lattice, a surplus of weakly bound electrons is created. Furthermore, new energy states below, but close to the conduction band are allowed and at room temperature most electrons are excited into the conduction band, which causes the Fermi levels to move up.
- P-type semiconductor:  
Similar considerations hold true for atoms which deliver one valence electron less than the bulk material. Once the acceptor is incorporated into the lattice, the missing negatively

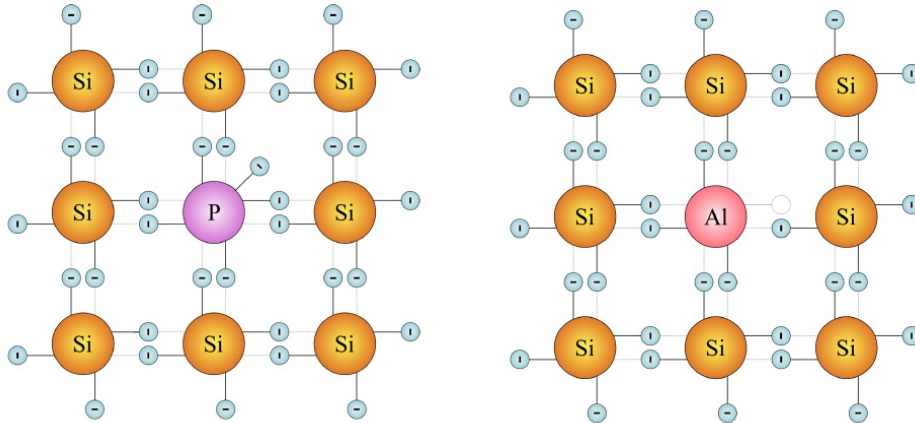


**Figure 3.3:** Doping of a silicon lattice with a group V type element (left) and a group III type element (right). The first one is forming a n-type, the latter is forming a p-type semiconductor [6]

charged electron acts just like a positive charge. New energy levels near the edge of the valence band are created and occupied by electrons from the valence band. The Fermi level moves down.

The above considerations are shown in figure 3.4. Through doping of pure silicon intermediate energy levels are created and the Fermi level shifts towards the edges of the valence- and the conduction band. This leads to an increased concentration of free charge carriers, hence the resistivity

$$\rho = \frac{1}{q_e(n \cdot \mu_e + p \cdot \mu_h)} \quad (3.11)$$

of the bulk material at a given temperature is subject to change.  $q_e$  is the electron charge,  $\mu_e$  and  $\mu_h$  are the mobilities of the charge carriers.  $\rho$  of intrinsic silicon is about  $235k\Omega$ . If the donor atoms are dominant, this equation can be simplified to

$$\rho = \frac{1}{q_e \mu_e N_d}, \quad (3.12)$$

accordingly for acceptor atoms in a p-type semiconductor.

While an undoped semiconductor is called *intrinsic*, a doped semiconductor is called *extrinsic*. In intrinsic semiconductors, for each electron exists a corresponding hole, while in extrinsic semiconductors a surplus of electrons or holes is created, depending on n- or p-type doping, respectively.

Still, these properties are temperature dependent, see fig. 3.5.

- At low temperatures, some electrons are *frozen* at the donor level.
- With increasing temperature all donors become ionized. This is called *extrinsic* region.
- At even higher temperatures, when  $k_B T$  reaches  $E_g$ , the semiconductor becomes intrinsic, because the carrier concentration becomes comparable to the donor concentration.



CHAPTER 3. DOUBLE SIDED SILICON SENSORS OF THE BELLE II VERTEX DETECTOR

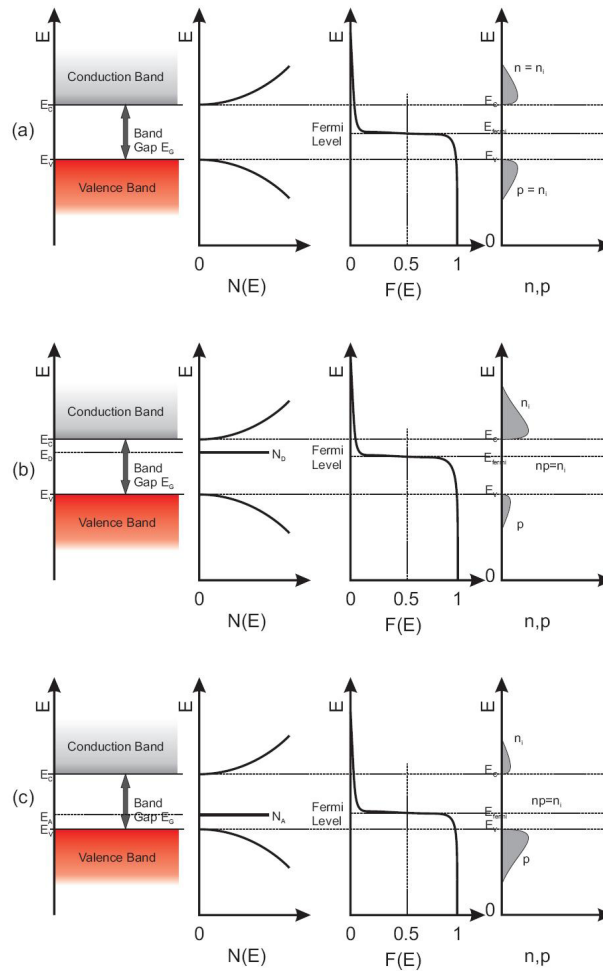


Figure 3.4: State density, Fermi levels and free charge carrier concentration of intrinsic (a), n-type (b) and p-type (c) silicon. [6]

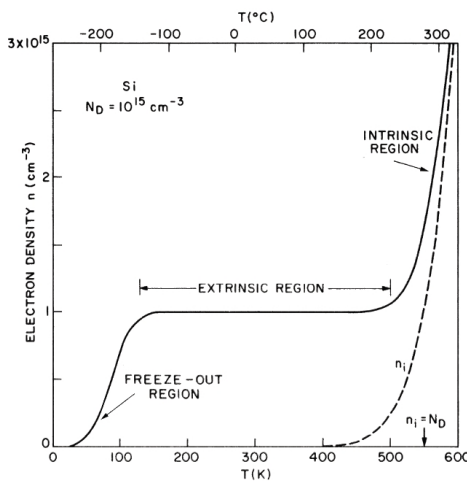
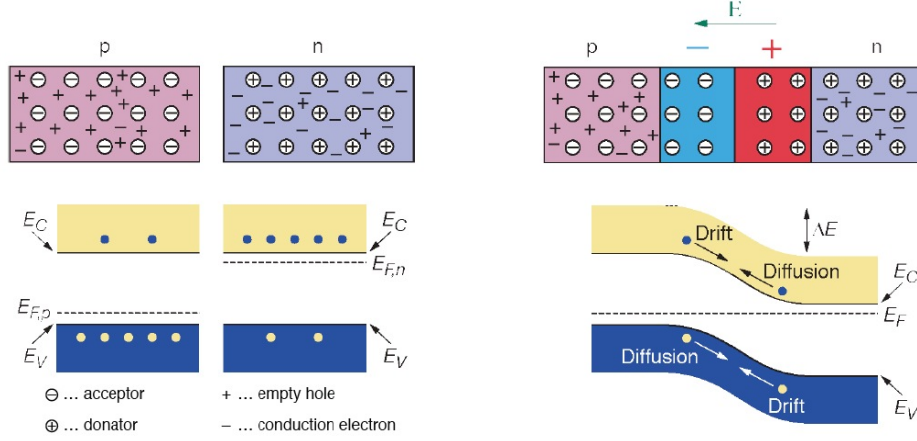


Figure 3.5: Electron density as a function of temperature for a Si sample with a donor concentration of  $10^{15} \text{ cm}^{-3}$ . [9]

### 3.3 pn-junction

A pn-junction is a device that consists of two types of semiconductors, one of which is n-type and the other one is p-type doped. Such a device is also called *Diode* and is one of the most essential semiconductor devices.

When two semiconductors of different types are merged, free charge carriers diffuse into the opposite region and recombine, see fig. 3.6. The ionized dopant atoms, which occupy fixed



**Figure 3.6:** Space charge region and Fermi levels of a pn junction. [5]

lattice positions, create a so called *space charge region (SCR)*. The polarity of the electrical potential which evolves in the SCR, called *built in voltage  $V_{bi}$* , counteracts the diffusion of the free charge carriers. Thus, an equilibrium is reached between the diffusion of the charge carriers, caused by the concentration gradient at the junction, and the drift due to the built in voltage. Otherwise, electrons and holes would distribute themselves homogenously across the diode. Since the SCR is depleted of free charge carriers, it is called *depletion zone*. Regarding the width of the depletion zone in p-type

$$W_p = \sqrt{\frac{2\epsilon_o\epsilon r N_A V_{bi}}{q N_D (N_A + N_D)}} \quad (3.13)$$

and n-type material,

$$W_n = \sqrt{\frac{2\epsilon_o\epsilon r N_D V_{bi}}{q N_A (N_A + N_D)}} \quad (3.14)$$

the width of the SCR is given by

$$W_{SCR} = W_p + W_n = \sqrt{\frac{2\epsilon_o\epsilon r (N_A + N_D) V_{bi}}{q_e N_A N_D}}. \quad (3.15)$$

Also the band structure is subject to change in the SCR. As discussed above, the Fermi level of an extrinsic semiconductor moves up or down, depending on n- or p-type doping, respectively. Once contacted, the Fermi levels of the two different semiconductors still have to line up at thermal equilibrium. Thus, the valence- and conduction band are shifted as well within the SCR, see figure 3.6. This is the explanation for the diffusion and drift from the energy band structure point of view. By applying external *bias* voltages, the potential barrier at the junction

### CHAPTER 3. DOUBLE SIDED SILICON SENSORS OF THE BELLE II VERTEX DETECTOR

can be modified.

Depending on the polarity of the external voltage  $V_{bias}$ , the depletion zone can grow or shrink. If a positive potential is applied on the p-side and negative potential on the n-side,  $V_{bias}$  is called *forward bias*. In the opposite case it is called *reverse bias*. Forward biasing will shrink the width of the depletion zone and increase the potential barrier, while reverse biasing expands it and diminishes the potential barrier. Taking into account an external bias voltage, the width of the depletion zone becomes

$$W_{SCR} = W_p + W_n = \sqrt{\frac{2\epsilon_o\epsilon r(N_A + N_D)(V_{bi} - V_{bias})}{q_e N_D(1 + N_D/N_A)}} + \sqrt{\frac{2\epsilon_o\epsilon r(N_A + N_D)(V_{bi} - V_{bias})}{q_e N_A(1 + N_A/N_D)}} \quad (3.16)$$

$$= \sqrt{\frac{2\epsilon_o\epsilon r}{q_e}(V_{bi} - V_{bias}) \left( \frac{1}{N_D + N_A} \right)}. \quad (3.17)$$

Using equation 3.12 for the resistivity of an extrinsic semiconductor and taking into account the that  $V_{bias} \gg V_{bi}$ , relation 3.17 can also be written as

$$W \approx \sqrt{2\epsilon\epsilon_r\mu\rho|V_{bias}|}. \quad (3.18)$$

The fact that the width of the depletion zone depends on an external bias voltage and therefore can be manipulated is an important feature of pn-junction. Moreover, the width of the SCR can be extended until it reaches the borders of the semiconductor device. The applied voltage, which is necessary to achieve this, is called *full depletion voltage*, since the whole device is now empty of free charge carriers or fully depleted. This lays the basis for the working principle of a silicon strip detector, or semiconductor detectors in general, as will be discussed in more detail in the sections to come.

## 3.4 Working principle of semiconductor detectors

Similar to all other particle detectors, the principle of semiconductor detectors is to detect secondary particles, caused by the interaction of incoming radiation with the detector material. Charged particles interact with the Coulomb field of the lattice Atoms. In a silicon detector with an assumed thickness of  $d = 300\mu m$  within an area of  $A = 1cm^2$ , the amount of  $e^-h^+$  pairs created by interaction with a *minimum ionizing particle (mip)* can be estimated:

$$\frac{dE/dx \cdot d}{I_0} = 3.2 \times 10^4 \quad (3.19)$$

$I_0$  denotes the mean ionization energy, in silicon  $I_0$  is about  $3.62eV$ .  $\frac{dE}{dx}$  is the energy loss per unit length according to the *Bethe-Bloch formula*. For silicon,  $\frac{dE}{dx}$  is about  $3.87MeV/cm$ . As described in section 3.1, the intrinsic charge carrier density in silicon is  $1.45 \times 10^{10}cm^{-3}$ . Accordingly, within the same volume of the detector, there would be

$$n_i \cdot d \cdot A = 4.35 \times 10^8 \quad (3.20)$$

intrinsic charge carriers. Hence, intrinsic charge carriers still would outnumber the charge carriers created by incoming radiation by a magnitude which is 4 orders larger. To this point it becomes clear, that a silicon semiconductor detector has to be operated in *full depletion mode*. Hence, a reverse bias voltage is applied as discussed in section 3.3 whenever a silicon detector is operated.

### 3.4. WORKING PRINCIPLE OF SEMICONDUCTOR DETECTORS

#### 3.4.1 Capacitance

Regarding the standard formula of of a parallel-plate capacitor

$$C = \frac{\epsilon_o \epsilon r A}{d}, \quad (3.21)$$

where  $A$  and  $d$  denote the area and the capacitor thickness, respectively, and equation 3.18, the capacitance of a pn-junction is given by

$$C = \sqrt{\frac{\epsilon_o \epsilon r}{2\mu\rho |V_{bias}|}} \cdot A. \quad (3.22)$$

The voltage at which the SCR reaches the borders of the device is called *full depletion voltage*  $V_{depl}$ . As a matter of fact, the capacitance remains constant once  $V_{bias} \geq V_{depl}$  and is determined only by the intrinsic properties of the bulk material, hence  $\epsilon_o \epsilon r$ ,  $A$  and  $d$  as described in equation 3.21.

A typical  $CV$  curve is shown in Figure 3.7. The capacitance is plotted in the y-axis. Most commonly,  $1/C^2$  is plotted instead of  $C$ , due to better visualization of its theoretical behavior. At  $V = V_{depl}$ , full depletion occurs.  $V_{depl}$  thus thus is indicated by the kink of the  $CV$  curve.

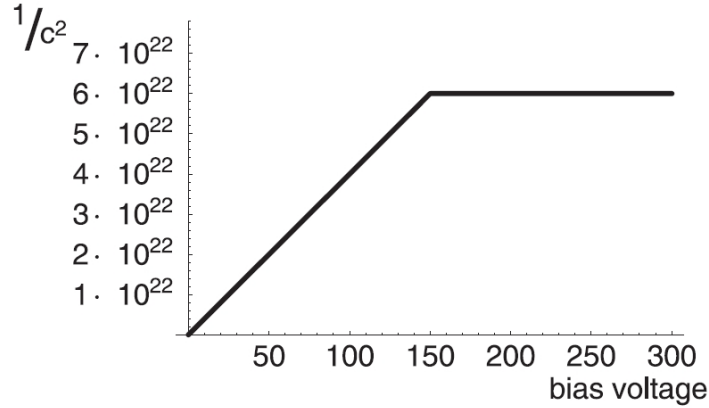


**Figure 3.7:** Theoretical behavior of the capacitance in a silicon detector. The kink indicates full depletion at  $V = V_{depl}$ .

#### 3.4.2 Segmentation

As mentioned above, the working principle of a silicon detector is to collect secondary particles created by incoming primary radiation. If a particle interacts with the detector material, secondary  $e^-h^+$  particles are created, see figure 3.8. These charges drift to the electrodes and create a drift current which is the actual detector signal. Furthermore, the position of the signal shall be deduced. Therefor, for silicon sensors a specific design of the pn-junction is chosen. Usually a very high doped but thin p-region ( $p^+$ ) on a lowly doped n-bulk, together with a highly doped n-region ( $n^{++}$ ) on the back side of the bulk material, builds the basic structure of a silicon sensor. In order to gain position resolution, the  $p^{++}$  region is segmented into many small strips or pixels, also called *implants*, which are read out separately, as shown in figure 3.8. The distance between the different segments is called *strip pitch*, and is usually in the order of  $50 - 200\mu m$ . If the bulk material is n-type, the detector is called n-type detector. For tradition and production reasons, most detectors are n-type. Due to segmentation, the  $p^+$  implants have

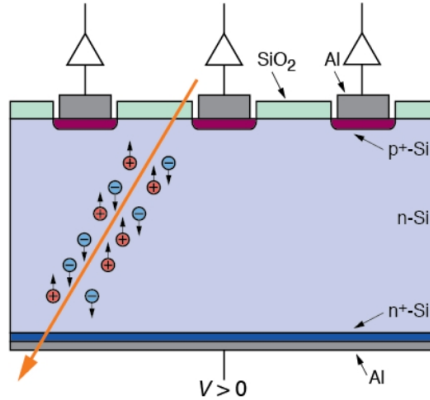


**Figure 3.8:** Secondary  $e^-h^+$  pairs created in the detector material by incoming radiation and being read out on  $p^+$  implants. [5]

a strip- or pixel-like geometry, hence silicon sensors are called *silicon strip-* or *pixel detectors*, respectively.

### 3.4.3 Bias resistor

As discussed in previous sections, a silicon detector has to be operated in full depletion mode. The full depletion voltage  $V_{depl}$  must be applied to the device. Since a typical silicon strip detector (*SSD*) consists of several hundred strips, for practical reasons it is impossible to apply the depletion voltage to each strip separately. While on the backplane  $V_{depl}$  can be applied directly, each of the *strip implants* is connected to a common *bias line* via so called *bias resistors* separately.  $V_{depl}$  is applied to the bias line only and the bias resistors connect each implant to the bias line, see figure 3.10. There are several other methods of biasing, such as *punch through-* and *FOXFET bias*. A bias resistor usually is made of poly-crystalline silicon, hence it is also

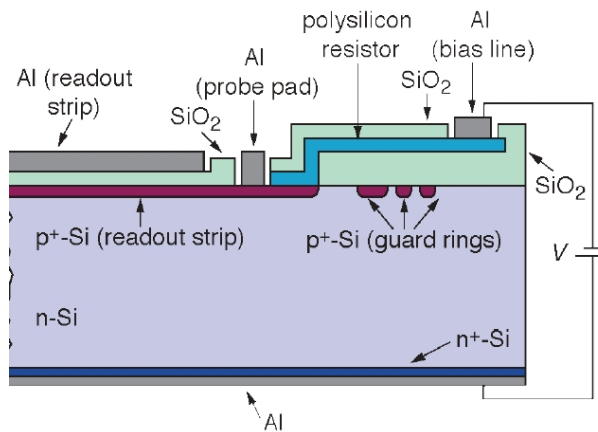


**Figure 3.9:** Cross section of a n-type SSD. [5]

called *poly resistor*. Due to noise considerations during electronic readout, usually very high resistances are chosen. To achieve high resistor values, meander structures are used. However, the resistivity is limited by the production process and the voltage drop across the bias resistor during operation.

### 3.4. WORKING PRINCIPLE OF SEMICONDUCTOR DETECTORS

#### 3.4.4 AC coupling

To block dark current from the readout chain, AC coupling is implemented during the production process. The detector isn't being read out directly at the implant. A  $\text{SiO}_2$  and an aluminium layer are deposited on top of the implant. Together, these three layers form an integrated capacitor which separates the readout circuit from the biasing circuit, see figures 3.9 and 3.10. The  $\text{SiO}_2$  layer has a thickness of usually several hundred  $\text{nm}$ . The capacitances usually are in

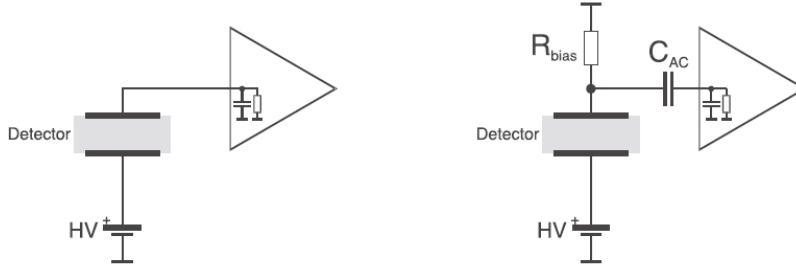


**Figure 3.10:** Equivalent circuits of DC (left) and AC (right) coupled readout schemes. [10]

the range of  $1.2\text{pF cm}^{-1}$  per  $\mu\text{m}$  of implanted strip width [7], depending on the oxide thickness. The readout systems and the silicon sensor interact with each other via the aluminium layer only, if AC coupling is used. Otherwise, if there is no  $\text{SiO}_2$  layer, the sensor is *DC coupled*.

#### 3.4.5 Passivation Layer

To protect the sensor from limited mechanical damages, such as scratches and from chemical interaction with air moisture, the uppermost layer is another silicon dioxide layer with a thickness of about  $1\mu\text{m}$ . At certain areas of the sensor surface, the passivation is etched, to provide an electric contact to the underlying metal layer. This is most commonly the case for certain areas of the bias ring and strips, to be able to apply the bias voltage and to connect the sensor to the readout system. These areas are called *openings*.

#### 3.4.6 Bond and probe pads

To gain electrical access to the strip implants and the metal layer, there are special vias, free from passivation, on the sensor surface. They are called *pads* and their width is about twice as large as the strip width, in order mechanically simplify being contacted by probes. Basically, there are two kinds of pads, which are also shown in figure 3.11:

- DC pads:  
DC pads provide an electrical connection directly to the implant. Thus, their existence is not necessary for detector operation, but they are highly important for the *quality assurance process* of the sensor.
- AC pads:  
Other than DC pads, AC pads are crucial for detector operation. They provide an electrical connection to the readout metal layer. Hence the readout chip is *bonded* to the AC pad area. Therefore, AC pads usually have a larger area than DC pads. Still, some electrical measurements during quality assurance use AC pads.

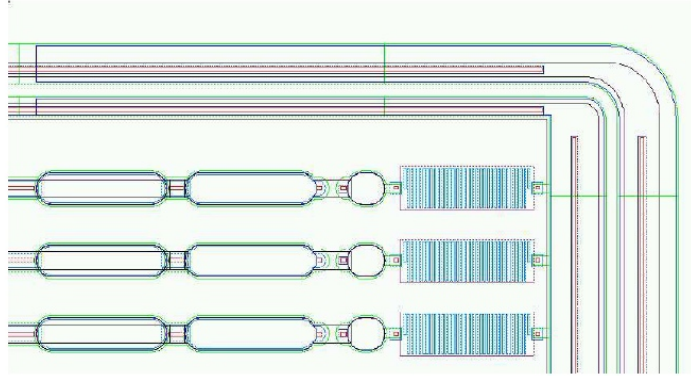


**Figure 3.11:** AC (left) and DC pads (center), meander shaped bias resistors (right) as well as bias and guard ring near the cutting edge of a silicon sensor. [11]

### 3.4.7 Metal overhang

Due to the high bias voltages, HV stability has to be ensured at the pn-junction. Therefore, a technology called *metal overhang* is put into place. The aluminium metal layer usually is a few  $\mu\text{m}$  wider than the implants below, in order to keep the maximum field density from the edges of the implant, see figure 3.12. Because of the metal overhang, the field maximum is moved to

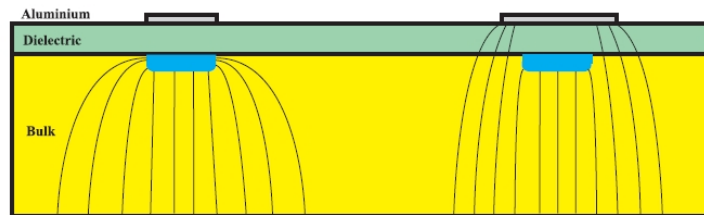


**Figure 3.12:** Metal overhang and field lines.[6]

the metal strips, while dielectric layer now is being penetrated by that maximum. Due to the lack of free charge carriers within the dielectric, a HV breakthrough is not possible, hence the HV stability is improved significantly.

### 3.4.8 Guard ring

HV usually is applied to the back side of the sensor, hence to the backplane, while the bias ring on the front side is grounded. Beside metal overhang technology,  $n^+$  implantation is used around the guard ring to the cutting edge of the sensor. The  $n^+$  ring follows the HV potential of the  $n^+$  backplane, thus it propagates the HV of the backplane to the front side of the sensor. This helps to avoid surface currents through the cut region from the backplane to the active area of the sensor and reduces dark currents. The guard ring is kept floating in order to smoothly adjust the electric field from GND to HV and therefore avoid HV breakdowns towards the sensor edges.

### 3.4.9 Double sided silicon sensors

So far the working principle and some important features have been discussed of *single sided* silicon detectors only. On single sided sensors, only one side of the device can be used for

### 3.4. WORKING PRINCIPLE OF SEMICONDUCTOR DETECTORS

readout and determination of the position of an event, since only one side consists of segmented implants, while the  $n^+$  backplane in fact is only used for biasing. Due to the strip geometry of the segmented implants, only one coordinate can be measured at a time by a single sided sensor. Within a particle detector that consists of single sided strip sensors only, a second layer of sensors is always required in order to measure the second coordinate. Consequently, this results in a higher material budget, which is to the disadvantage of the whole system.

By segmentation of the  $n^+$  backplane, the sensor becomes *double sided*. If the  $n^+$  strips are orthogonal to the  $p^+$  strips on the other side, two coordinates can be measured at a time and material budget can be minimized. Figure 3.13 shows the basic scheme of a double sided silicon detector (*DSSD*). Biasing and guard rings are not shown in figure 3.13. All considerations

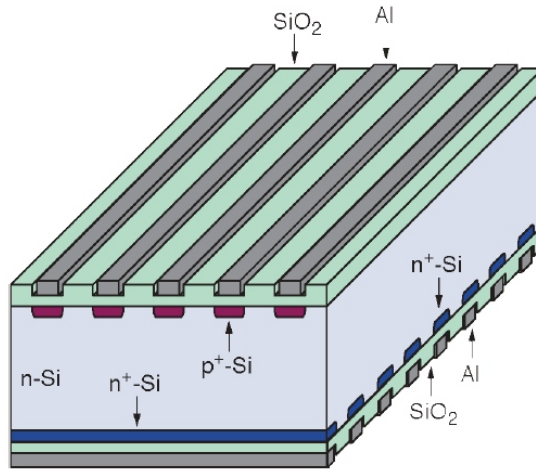


**Figure 3.13:** Double sided silicon detector with orthogonal strips. [5]

described in sections 3.4.1 to 3.4.8 basically hold true for the  $n^+$  side of the sensor, which is now segmented too. Nevertheless, there's one major difference to the  $p^+$  side, resulting from the different polarity.

Since on the  $n$  side  $n^+$  segments are implanted in a  $n$  type semiconductor material, the electrical separation of the strips becomes more complicated, due to the formation of a so called *accumulation layer*, see figure 3.14.

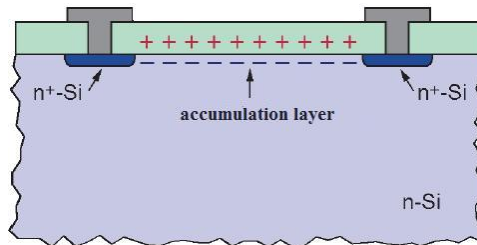


**Figure 3.14:** Accumulation layer beneath oxide. [5]

Within the  $SiO_2$  layer, there are static *positive* oxide charges, which attract electrons from the  $n$ -type bulk beneath. These electrons form an accumulation layer underneath the oxide, hence, as shown in figure 3.14, there is no more electrical separation of the  $n^+$  implants. Consequently, there can be no more position resolution, which in fact is a direct result of strip segmentation. Due to the low resistivity, caused by the accumulation layer, charges spread over



CHAPTER 3. DOUBLE SIDED SILICON SENSORS OF THE BELLE II VERTEX DETECTOR

many strips and any information on the coordinate of the interaction is lost.

The solution to this problem is to artificially interrupt the accumulation layer, using *p-stop* or *p-spray* technology, see figure 3.15.

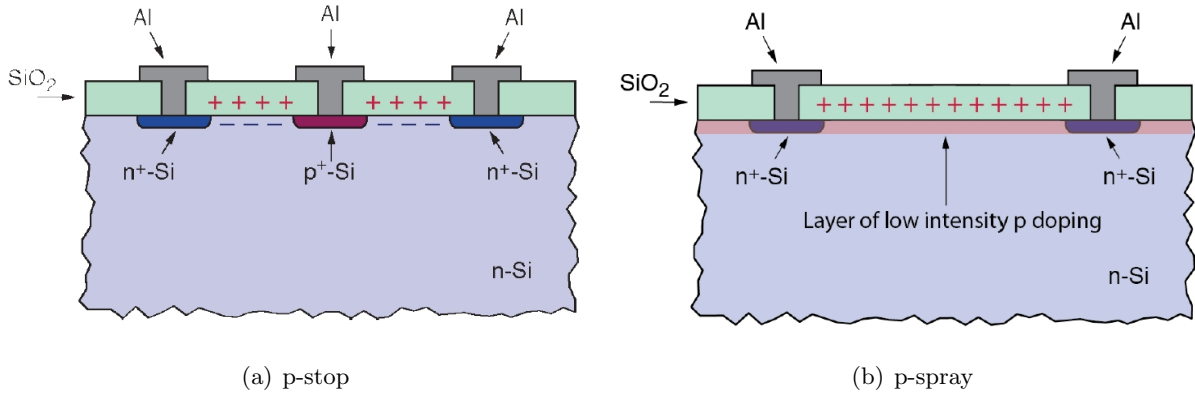


**Figure 3.15:** *p-stop* (a) and *p-spray* (b) technology, disrupting the accumulation layer. [5]

Due to the accumulation layer, the *interstrip resistance* decreases dramatically ( $k\Omega$ ). By using *p-stop* or *p-spray* technology, electrical separation between the segments is reassured and the interstrip resistance again is in the order of ( $G\Omega$ ).

While *p<sup>+</sup>-stop* technology uses an extra implant or *blocking electrode*, which interrupts the accumulation layer, *p<sup>+</sup>-spray* means that an extra layer of p-doped silicon is implanted beneath the oxide.

### Ghost hits

Double sided sensors are able to measure the two-dimensional position of an incoming particle. In case of two particles hitting the detector at the same time, however, *ghost hits* appear. The situation is shown in figure 3.16. *Pixel detectors* produce unambiguous hits. This type of silicon

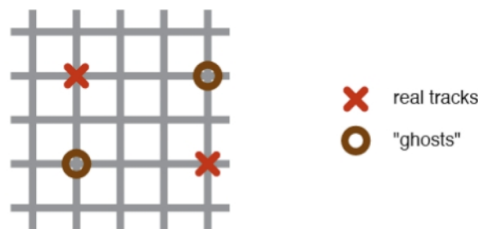


**Figure 3.16:** *Ghost hits on a double sided silicon detector.* [5]

sensors is used in the innermost layer of particle detectors in collision experiments. They require a large number of readout channels and electrical connections.

## 3.5 DSSDs for the Belle II detector

As described in section 2.3, due to the lantern shape of the Belle II silicon vertex detector (*SVD*), it consists of several layers of barrel and trapezoidal shaped silicon sensors, with the latter being attached to the slanted forward region of the *SVD*. Since multiple scattering is the

most important issue for Belle II, the largest available sensors are to be used and in order to minimize the material budget, double sided silicon sensors are chosen. The bulk material will be n-type and have a thickness of approximately  $300 \mu\text{m}$ . Wafer processing facilities are capable of producing six inch wafers, thus the sensors will be about 12 cm long and have a width of approximately 6 cm. [1]

While Hamamatsu Photonics will be producing the barrel sensors, Micron Semiconductor will be manufacturing the trapezoidal sensors for the forward part.

Both barrel and trapezoidal DSSDs will be AC coupled (see sec. 3.4.4) with integrated bias resistors (see sec. 3.4.3).

### 3.5.1 Barrel sensors

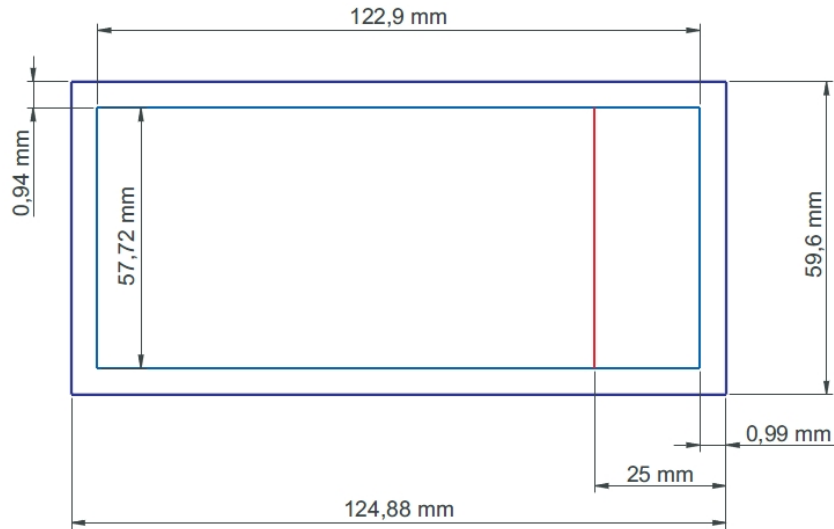


**Figure 3.17:** Geometry of barrel sensors for layers 4 to 6. Dark blue: outer dimensions. Light blue: inner active area. [1]

Since the barrel sensors used in layer 3 of the SVD are smaller and have different strip pitches and strip numbers, two kinds of barrel sensors will be produced by Hamamatsu Photonics. To this day, the small sensors of layer three have not been ordered yet. Figure 3.17 shows the geometric dimensions of the barrel sensors of layer 4 to 6, the main sensor parameters are stated in table 3.1. In table 3.2, electrical parameters of the rectangular sensors are summed up.

### 3.5.2 Forward sensors

To minimize material budget while still covering the forward acceptance region of the SVD, the sensors are slanted and trapezoidal in order to form a conical shape.

The strip-pitch on the p-side varies, resulting in a fan shape of the strips. On the n-side, strips are perpendicular to the central strip of the p-side. Actually, p-stop technology is featured here, as described in section 3.4.9.

Figure 3.18 shows the geometrical properties of the forward sensors, tables 3.3 and 3.4 state the sensor parameters. [1]

CHAPTER 3. DOUBLE SIDED SILICON SENSORS OF THE BELLE II VERTEX DETECTOR

| Quantity                     | large sensor                    | small sensor                    | wedge sensor                 |
|------------------------------|---------------------------------|---------------------------------|------------------------------|
| # strips p-side              | 768                             | 768                             | 768                          |
| # strips n-side              | 512                             | 768                             | 512                          |
| # intermediate strips p-side | 767                             | 767                             | 767                          |
| # intermediate strips n-side | 511                             | 767                             | 511                          |
| pitch p-side                 | 75 $\mu m$                      | 50 $\mu m$                      | 75...50 $\mu m$              |
| pitch n-side                 | 240 $\mu m$                     | 160 $\mu m$                     | 240 $\mu m$                  |
| area (total)                 | 7442.85 mm <sup>2</sup>         | 5048.9 mm <sup>2</sup>          | 6382.6 mm <sup>2</sup>       |
| area (active)                | 7029.88 mm <sup>2</sup> (94.5%) | 4737.80 mm <sup>2</sup> (93.8%) | 5890 mm <sup>2</sup> (92.3%) |

**Table 3.1:** Basic parameters of rectangular and wedge sensors

| Quantity                         | rectangular   | wedge  |
|----------------------------------|---|--|
| base material                    | Si n-type, 8k $\Omega cm$                                 | Si n-type, 8k $\Omega cm$  |
| full depletion voltage (FD)      | < 120V  | 40V( <i>typ.</i> ), 70V( <i>max.</i> )                             |
| operation voltage                | ns  | FD...2 $\times$ FD   |
| breakdown voltage                | $\geq FD + 50V$   | $\geq 2.5 \times FD$   |
| bias resistor                    | 4M $\Omega$ ( <i>min.</i> ), 10M $\Omega$ ( <i>typ.</i> ) | 10M $\Omega$ ( <i>min.</i> ), 15 $\pm$ 5M $\Omega$ ( <i>max.</i> ) |
| coupling capacitance             | > 100pF   | ns   |
| breakdown voltage of AC coupling | > 20V   | ns   |
| bias leakage current at FD       | 1 $\mu A$ ( <i>typ.</i> ), 10 $\mu A$ ( <i>max.</i> )     | ns   |
| interstrip resistance p-side     | ns  | 100M $\Omega$ ( <i>min.</i> ), 1G $\Omega$ ( <i>typ.</i> )         |
| interstrip resistance n-side     | ns  | 10M $\Omega$ ( <i>min.</i> ), 100M $\Omega$ ( <i>typ.</i> )        |

**Table 3.2:** Electrical parameters of rectangular and wedge sensors

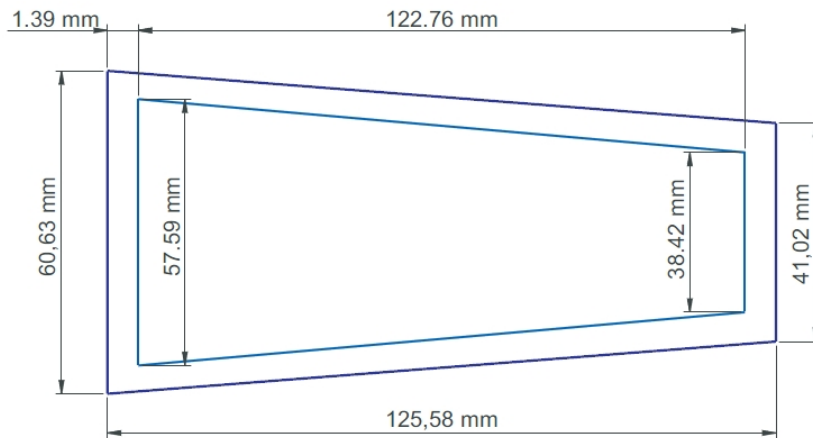


**Figure 3.18:** Geometry of the trapezoidal sensors in the forward region. Dark blue: outer dimensions. Light blue: inner active area. [1]

### 3.5. DSSDS FOR THE BELLE II DETECTOR

## Chapter 4

# Quality assurance at HEPHY Vienna

Before being mounted onto the ladders (see sec. 2.3), the silicon sensors have to be tested carefully and it has to be assured that certain specifications and requirements are fulfilled. At first, the sensors are tested by the vendors themselves before they are delivered. Still, additional quality assurance is done at several *quality test centers (QTC)* around the world, depending on the work groups involved. For the BELLE II sensors HEPHY Vienna is the only place where quality assurance is done.

At the HEPHY Vienna, such a QTC has been operated for many years and quality assurance had been done for the *CMS Tracker*.

Similar, the silicon sensors for the BELLE II SVD are being qualified at the QTC Vienna. One has to distinguish between tests on prototype sensors and mass production. While for the latter, only randomized tests will be performed, prototypes will undergo full quality assurance. Not only this means that full scale tests will be performed, but also that each of the prototypes will be tested. The QTC Vienna and the measurement procedures being performed will be discussed in detail in the following sections.

### 4.1 The QTC Vienna

The QTC is a full scale automated setup, designed for electrical measurements on silicon sensors, run by *LabView* software. See figure 4.1 for an overview of the whole setup. It consists of a light tight box where the sensor is put on vacuum support. A motorized XYZ-table is operated to precisely move the sensor, down to a  $\mu\text{m}$  scale, if necessary. It can be controlled either semi-automatically by using a joystick, or completely automated, run by Lab View software. Various micro positioners, each of which is holding a needle, are used to contact the bias lines, AC and DC pads of the sensors (see sec. 3.4.6). Two positioners on the right are used for *biasing*, being switched in parallel and contacted to the bias line. Parallel switching reduces the risk losing contact if one positioner mismatches. Both positioners are mounted onto the XYZ-table, providing bias voltage also during a movement of the sensor.

On the left hand side of the sensors, there are two or more *fixed* positioners. Their purpose is to contact AC and DC pads, in order to perform electrical measurements on the individual strips. By moving the XYZ-table with the sensor on top of it, each strip can be approached separately. A microscope is used by the operator to contact the needles to the bias line and the pads, since this has to be done manually on a  $\mu\text{m}$  scale, at the beginning of the measurements.

Before a measurement run can be started, an *alignment procedure* has to be completed. Each sensor type has different geometry (see sec. 3.5). The LabView software reads a so called *pad file*, which

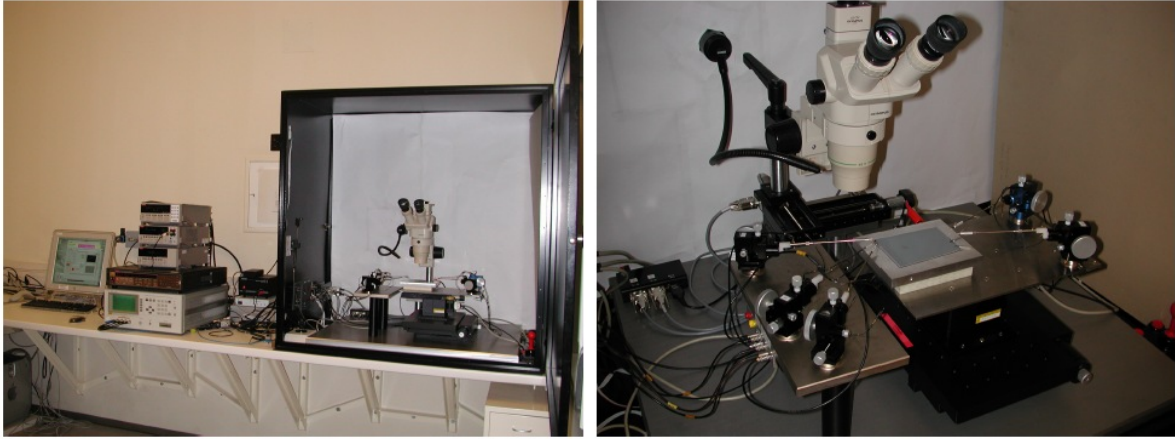


**Figure 4.1:** Overview of the QTC at the HEPHY Vienna. Instruments and computer (left), light tight box, containing the XYZ-table, positioners, sensor and the microscope (right). [6]

provides the information on strip numbers and strip pitch. Usually, each sensor type shares its own pad file. The operator has to perform 3 steps during the alignment procedure:

1. Place the sensor onto the vacuum table. The XYZ-table moves to *reference point 1*. Now the operator manually adjusts the needle to the pad, which was chosen to be "reference point 1", according to the pad file.
2. Now the XYZ-table automatically moves to "reference point 2", again according to the pad file. The operator places the same needle onto the pad which was chosen to be "reference point 2". Since the needle mustn't be moved once the alignment procedure has been started, the table now can be moved semi-automatically by using a joystick.
3. The same procedure is repeated for a third reference point.

Once the alignment procedure has been completed successfully, the XYZ-table can move automatically and approach any strip demanded by the operator. The table performs three steps when approaching a strip on the sensor: It moves down several mm, losing contact, performs a XY movement until it reaches the coordinate of the desired strip number and then lifts up again, re-establishing contact with the probe pad.

The instruments used for the QTC are shown in more detail in figure 4.2. Together with the XYZ-table they are operated automatically by LabView software, using the IEEE488 (GPIB) interface bus. In order to make possible current measurement precisions down to  $pA$  range, Triax cables and connectors are used, whenever instrument limitations allow it. The five instruments seen in figure 4.2, from top to bottom, are [6]:

- Switching matrix frame: Keithley 7001 equipped with two 7153 matrix cards (  $5 \times 4$  contacts)
- Secondary source measure unit (SMU2): Keithley 2410
- Electrometer (EL): Keithley 6514
- Primary source measure unit (SMU): Keithley 237

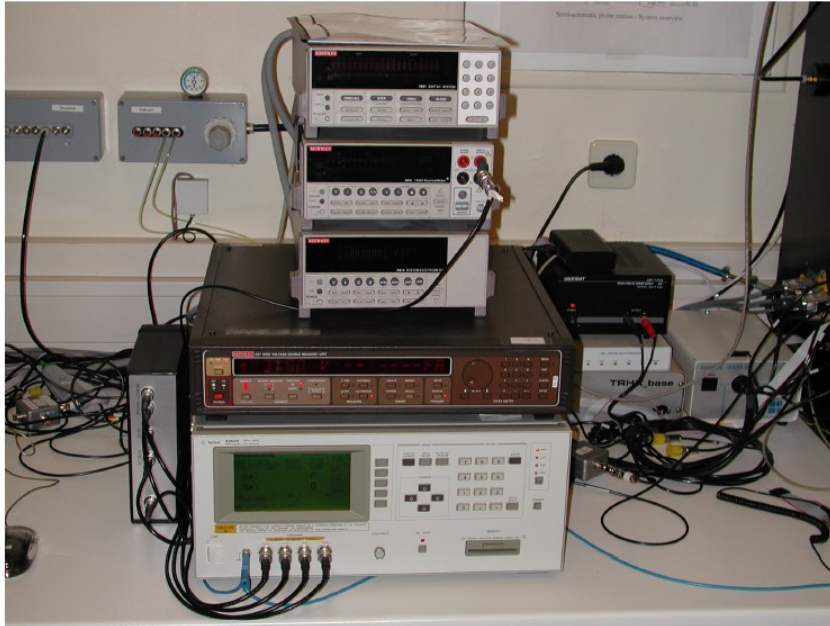


*Figure 4.2: Instruments of the QTC.*

- High frequency (HF) capacitance meter (LCR): Agilent 4284A

The purpose of the switching matrix is to connect the probes in the light tight box to the instruments. Since for each individual measurement that is performed, different combinations of the instruments are necessary, the switching system provides a flexible solution to this problem. Once the alignment procedure has been done, the operator chooses the measurements he wants to be performed, and the matrix automatically switches between different measurement configurations.

The bias voltage (see sec. 3.4, 3.4) is supplied by the primary SMU, K-237, while the other instruments are used in various ways to measure electrical properties of the sensors. This will be described in more detail in the sections to come.

Some additional devices, supporting the measurement process are:

- A self made decoupling box. Via a high pass filter, high DC bias voltages are separated from the LCR-meter inputs.
- The THRX system is used to monitor temperature and humidity in the light tight measurement box [12].
- A cold-light source with fiber optics illuminates the sensor surface while the operator manually adjusts the probes to the pads.
- Humidity in the measurement box can be controlled by compressed air and air conditioning regulates overall room temperature.

## 4.2 Measurement types

Each type of measurement requires its own configuration of probe needles and instruments, hence a specific matrix configuration. The functional schematic of the switching matrix is shown in figure 4.3.

### Switching System

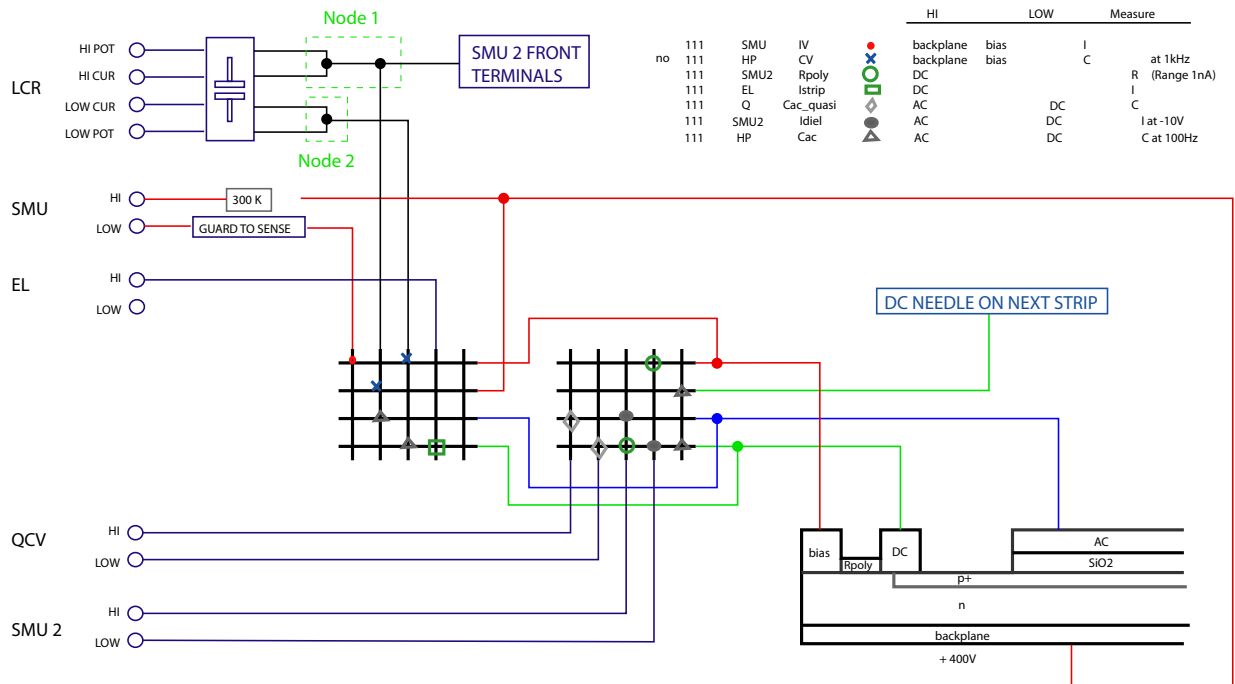


Figure 4.3: Switching matrix functional schematic.



- The central matrices represent the two 7153 matrix cards with  $5 \times 4$  contacts each and the way they are connected to the probe needles on the sensor and to the instruments.
- At the bottom right a cross section of the sensor is shown, with the possible contact areas (AC and DC pads, bias line and backplane) clearly visible, as well as the implant and the bias resistor. Also the "DC pad of the next strip" is shown, since it is required for some measurements.

The coloured wires indicate the probe needles. Usually there are five needles being used:

- Red: bias needles
  - Green: DC needles. There are two DC needles, contacting neighboring strips.
  - Blue: AC needle
- To the left, the instruments of the measurement bench are shown, and how they are connected to the switching system

Since there are two two-dimensional switching matrices, three indexes are required to determine a specific switching configuration. The first index refers to the matrix, the second one to the row and the third to the column.  $(1,1,1)$  for example means, that on the first matrix (the left one) contact (1,1) is closed, hence, *SMU low* is connected to the bias line via one of the bias needles, see figure 4.3. Only one connection is not optional. The bias needle providing the HV is permanently connected to the backplane

Basically, there are two kinds of measurement types being performed on the sensors: *Global scans* and *strip scans*. Both types use the switching scheme described above.

#### 4.2.1 Global scans

In global scans, the capacitance and the dark current in reverse bias mode of the whole sensor are qualified. These are the most fundamental measurements being performed, by means of which the overall quality of the sensor can be estimated.

To be more specific, an *IV* and a *CV* curve are taken. If the pn-junctions work properly or the overall manufacturing of the sensor is of good quality, these curves have characteristic shape. Otherwise, it is presumed that the sensor is defective. This is especially the case if the dark current in reverse bias mode exceeds certain limits.

##### Global IV curve

This is the most fundamental and usually first measurement that is performed in a sensor.

The instrument used for this measurement is the *primary SMU (SMU I) K-237*, which generally is responsible for supplying the bias voltage and depleting the sensor. Thus, it also measures the dark current. Consequently, by utilizing the SMU I an *IV* curve of the sensor can be taken. The matrix configuration necessary for this measurement is  $(1,1,1)$ . As can be seen in figure 4.3,  $(1,1,1)$  connects the low output of the SMU I to the bias line, and the high output to the backplane. As described in section 3.4.8, HV is always applied to the backplane, while the bias line is grounded. Thus,  $(1,1,1)$  is also the common configuration for biasing a sensor and is permanently closed during other measurements.

When taking a global *IV* curve, the bias voltage slowly is ramped, usually in 5 V steps from zero to several hundred Volts. At each step, after a delay of 2 s, the detector current is measured. The delay is important, since the detector capacitance and the shunt resistor act as a RC-network. An example of a global *IV* curve is shown in figure 4.4.

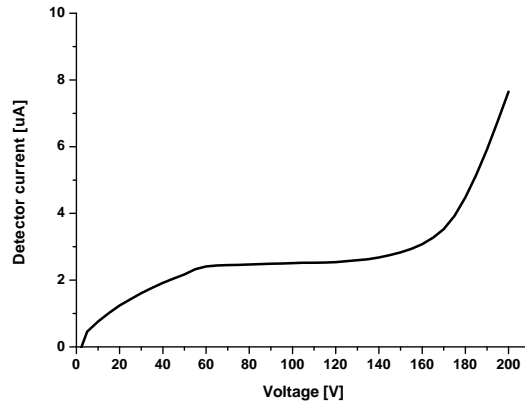


*Figure 4.4: Example of a global IV curve.*

### Global CV curve

By measuring a CV curve, the depletion voltage can be determined. Similar to the IV curve, SMU I is used to ramp the bias voltage in 5 steps. At each step, the *LCR-meter Agilent 4284A* measures the capacitance of sensor bulk. As already described in section 3.4.1, the result usually

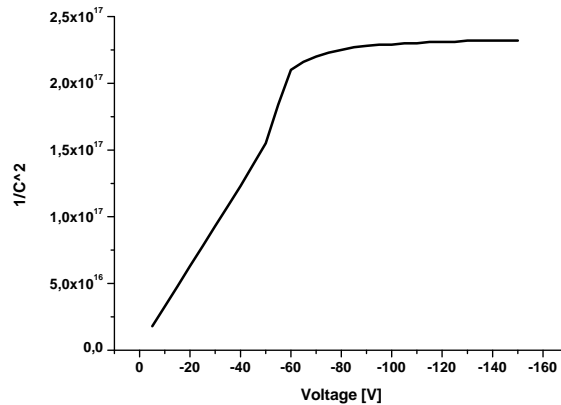


*Figure 4.5: Example of a global CV curve*

is plotted with  $1/C^2$  on the Y-Axis, to better visualize its behavior, see figure 4.5. The kink indicates the full depletion voltage  $V_{depl}$ .

The CV measurement is more complicated than the IV measurement. At first, SMU I has to ramp a potential on the sensor. This happens similar to the procedure described above, using the (1,1,1) connection according to the switching scheme, see figure 4.3. After the the voltage has been applied, the LCR meter is supposed to measure the capacitance of the sensor bulk. Therefor, channels (1,2,2) and (1,1,3) are closed. Since now the low terminal of both the LCR-meter and SMU I would be connected to the bias line, the low terminal SMU one has to be disconnected during the capacitance measurement of the LCR-meter. Otherwise, a short would be created in the LCR-meter and the SMU I. This is the only measurement where the (1,1,1) connection is disconnected. Meanwhile, SMU I is grounded externally, bypassing the switching

system

The LCR-meter determines the capacitance of a DUT<sup>1</sup> by applying an AC voltage and measuring the phase of the current. The signals across the DUT are [13]:

$$V_{DUT} = \frac{Z_X}{R_{SO} + Z_X} \times V_{Osc} \quad (4.1)$$

and

$$I_{DUT} = \frac{V_{Osc}}{R_{SO} + Z_X} \times V_{Osc}, \quad (4.2)$$

where  $V_{Osc}$  denotes the oscillator voltage level and  $R_{SO}$  the source resistor of the LCR-meter (100Ω).  $V_{DUT}$ ,  $I_{DUT}$  and  $Z_X$  are the voltage and current levels and the impedance of the DUT, respectively.

When knowing the impedance, equation 4.3 finally yields the capacitance.

$$Z_X = R_p + iX = R_p - i \frac{1}{2\pi f C} \quad (4.3)$$

Where  $i$  is the imaginary unit and  $R_p$  is the parallel resistance to the capacitance of the equivalent circuit.

Due to the fact that during a global CV measurement, the low terminal of LCR-meter is connected to the bias line, instead of the low terminal of the SMU I, while the HV on the backplane is still applied. Since the maximum input voltage level on the terminals of the LCR-meter is 40 V and the HV on the backplane is several hundred Volts, a *decoupling box* is used.

It acts as a high-pass filter to the AC voltage of the LCR-meter and keeps the bias voltage away from the terminals.

#### 4.2.2 Measurements on strips

For more detailed investigations on silicon sensors, *strip scans* are performed. Certain electrical properties are tested on each individual strip. These properties are:

- The dark current of the implants, or the *strip leakage current*.
- The actual value of the polysilicon resistors.
- The *coupling capacitance* between the metal layer and the implant (see section 3.4.4).
- The current across the dielectric.

During each measurement, the sensor is *overdepleted*<sup>2</sup>, hence (1,1,1) of the switching system remains closed during all measurements. The bias voltage  $V_{bias}$  is applied before the measurement run and not shut down until the *strip scan* has been finished.

#### Strip leakage current

The single strip leakage current is measured because the *signal to noise ratio* suffers from noisy strips. Hence, strip leakage currents as low as possible are demanded. Furthermore, the homogenous distribution of strip currents over the whole sensor is also a quality feature.

For measuring the single strip current, the probe needle attached to the DC pad has to be

---

<sup>1</sup>DUT: Device Under Test

<sup>2</sup>Overdepleted:  $V_{bias} = V_{depl} + 20\%$

connected to the Keithley 6514 electrometer. According to the switching scheme, see figure 4.3, this means that contact (1,4,4) has to be closed. Since the electrometer is grounded, it bypasses the normal current path of the strip current, which would be through the bias resistor to the bias line. The bias resistor is in the order of  $M\Omega$ , while the internal resistance of the electrometer is neglectable.

Typical strip leakage currents are several hundred pA to 5 nA.

### Bias resistor

As described in section 3.4.3, there are certain limits for the bias resistor due to noise considerations of the readout electronics.

The Keithley 2410 SMU II is used for measuring the bias resistor, contacts (2,4,3) and (2,1,4) have to be closed by the switching system, see figure 4.3. This connects the DC needle to high terminal of the SMU II and the bias needle, grounding the bias line, to the low terminal. Hence, the SMU II can make an resistance measurement of the bias resistor, since the bias resistor is the connection between the implant, to which the DC pad is directly connected, and the bias line.

### Coupling capacitance

The capacitance between the  $p^+$  implant and the aluminium metal layer across the  $\text{SiO}_2$  dielectric is called coupling capacitance, see section 3.4.4. To determine its value, the high frequency capacitance meter Agilent 4284A (LCR-meter) is used. According to the switching system, see figure 4.3, connections (1,2,2) and (1,3,3) have to be closed, in order to connect the AC needle, which contacts the metal layer via the AC pad, to the high terminal of the LCR-meter and the bias needle, grounding the bias line, to the low terminal.

The measurement works similar to the measurement of the global capacitance, as described in section 4.2.1, besides the fact that a smaller frequency is used (100 Hz). This is done with respect to the strip length, which can be up to 12 cm.<sup>3</sup>

Furthermore, a second DC needle (*DC 2*) is shorted with the *DC 1* needle. The DC 2 needle is

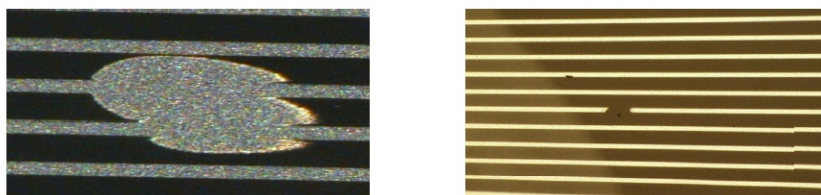


**Figure 4.6:** Single strip failures on sensors. An "open" is shown on the left, a "short" on the right. [6]

contacted to the next consecutive strip. The purpose of this method is to detect failures of the metal layers of the individual strips, see figure 4.6. A *short* increases the coupling capacitance, if the measurement includes the DC 2 needle. The active area of the capacitor is increased if two strips are shorted by the metal layer.

An *open* decreases the active area of the capacitor, hence the capacitance measured.

<sup>3</sup>Depending on the strip length and the frequency, only a small part of the implant contributes to the measurement, see sec. 7

### Dielectric current

The most severe damage of a single strip is if there is a short between the metal layer and the implant. This is called *pinhole*. In order to detect pinholes, it is not sufficient to measure the coupling capacitance only. Hence, an additional measurement is demanded. The low terminal of the SMU II is connected to the bias line, while the high terminal is connected to the AC pad. The switching configuration used is (2,3,3) and (2,4,4), see figure 4.3. This allows the SMU II to apply a voltage between the metal layer and the implant, while measuring current. Usually this voltage is 10 V. This is a more secure method to assure that there is no short, hence ohmic connection through the oxide.

On a normal strip the current measured of the SMU II usually is below 0.5 nA. If there appears to be a pinhole, the SMU most commonly is driven into compliance (100 nA). Consequently, pinholes can easily be detected by this method.

### Stripcans

The results of the measurements described above are plotted over the strip numbers. An example of such a strip scan is shown in figure 4.7.

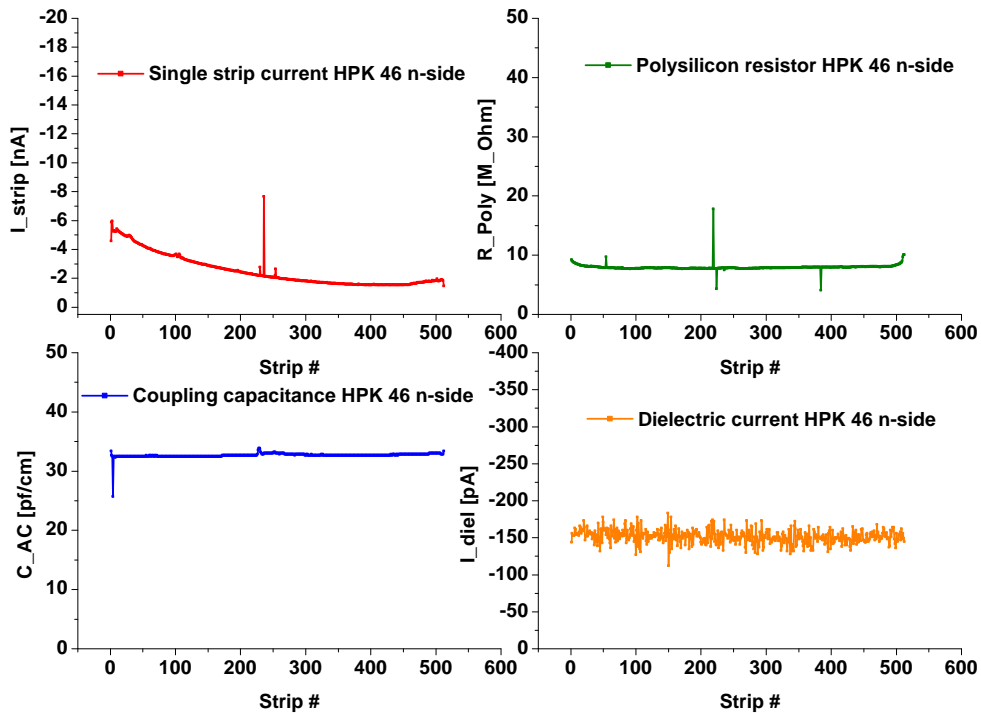


*Figure 4.7: Single strip measurement results plotted over stripnumber.*

Usually the quantities measured are called:

- single strip current:  $I_{strip}$
- polysilicon resistor:  $R_{poly}$

## 4.2. MEASUREMENT TYPES

- coupling capacitance:  $C_{AC}$
- current across dielectric:  $I_{diel}$

## Chapter 5

# Standard Measurements performed with the QTC

Stripskans and global measurements, as described in the previous section, were performed on several batches of Hamamatsu barrel- and Micron wedge sensors. These sensors are prototypes for the Belle II SVD and not destined to be operated as sensors in any experiments at all.

Together with long term and radiation tests these measurements offer important information on the basic quality and expected performance of the sensors.

Hamamatsu delivered three batches of prototype sensors. Due to experiment schedules, for the following results only the second batch of Hamamatsu sensors and only the first batch of Micron sensors (which was the only one available at the time the measurements were performed) have been taken into consideration.

### 5.1 Hamamatsu 2nd batch

#### 5.1.1 Global Measurements

The results shown in figure 5.1 and figure 5.2 show the global IV and CV curves of the sensors

- HPK 46,
- HPK 47 and
- HPK 48.

Clearly the sensors listed above meet the specifications shown in table 3.2.

#### 5.1.2 Stripskans

Table 5.1 shows the averaged values for each quantity on the n-sides of Hamamatsu sensors 46, 47, and 48. The p-side stripskans are summed up in Table 5.2. A notable result is that there are almost no pinholes, either on the n-sides nor on the p-sides. Also hardly any noisy strips were detected.

The areas of the aluminium metal layers differ by a factor of two, hence the coupling capacitance on the p-sides should be only half the capacitance of the n-sides. This is proven perfectly by this measurement.

The corresponding plots to these measurements are found in the appendix.

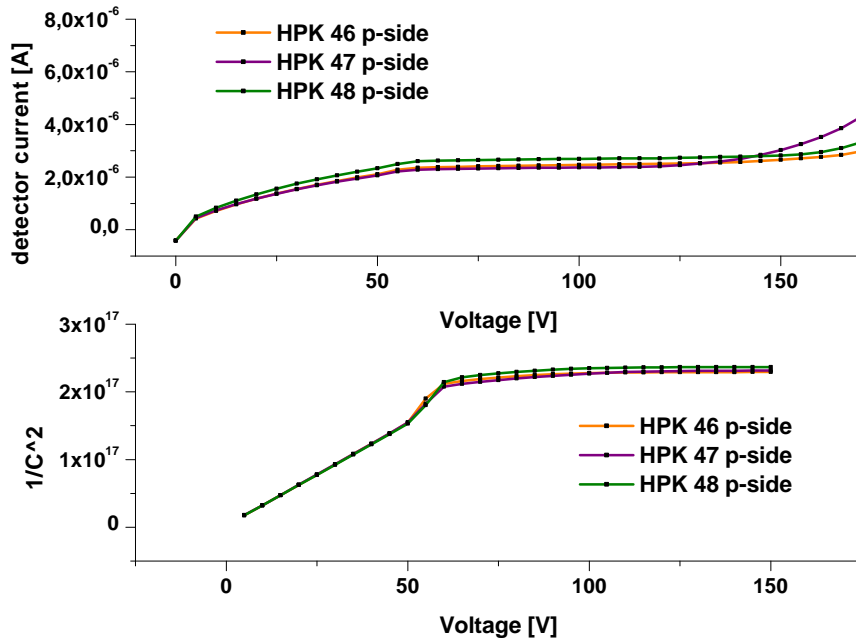


Figure 5.1: Global IV (top) and CV (bottom) plots of p-sides of Hamamatsu sensors HPK 46, 47 and 48.

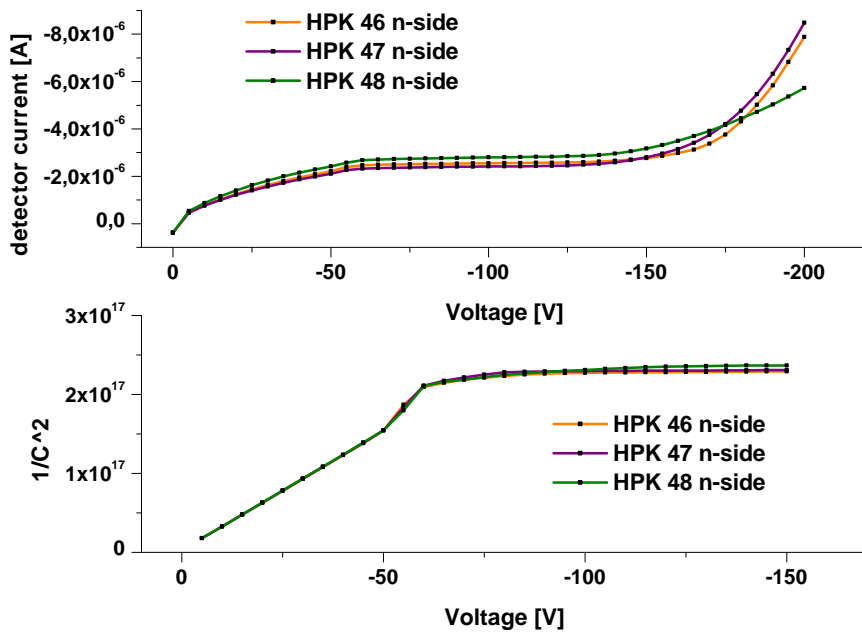


Figure 5.2: Global IV (top) and CV (bottom) plots of n-sides of Hamamatsu sensors HPK 46, 47 and 48.



| n-sides average        | $I_{strip}$         | $R_{poly}$                | $C_{AC}$             | $I_{diel}$           |
|------------------------|---------------------|---------------------------|----------------------|----------------------|
| HPK 46                 | $-2.40 \pm 1.1$ nA  | $7.90 \pm 0.6$ M $\Omega$ | $32.7 \pm 0.4$ pf/cm | $-151.5 \pm 9.3$ pA  |
| HPK 47                 | $-2.35 \pm 1.15$ nA | $8.8 \pm 1.3$ M $\Omega$  | $32.8 \pm 1.6$ pf/cm | $-150.6 \pm 9.2$ pA  |
| HPK 48                 | $-2.45 \pm 1.25$ nA | $8.2 \pm 0.1$ M $\Omega$  | $32.1 \pm 1.6$ pf/cm | $-139.5 \pm 15.5$ pA |
| mean value             | -2.44 nA            | 8.34 M $\Omega$           | 32.5 pf/cm           | -147.2 pA            |
| standard deviation (?) | 1.17 nA             | 0.7 M $\Omega$            | 1.2 pf/cm            | 11.4 pA              |
| bad strips %           | 0.00 %              | 0.98 %                    | 0.20 %               | 0.00 %               |

**Table 5.1:** Averaged n-side stripscan results of Hamamatsu sensors HPK 46, 47 and 48.

| p-sides average        | $I_{strip}$        | $R_{poly}$                | $C_{AC}$             | $I_{diel}$           |
|------------------------|--------------------|---------------------------|----------------------|----------------------|
| HPK 46                 | $1.58 \pm 0.38$ nA | $11.0 \pm 1.0$ M $\Omega$ | $17.2 \pm 0.5$ pf/cm | $-142.1 \pm 10.5$ pA |
| HPK 47                 | $1.63 \pm 0.42$ nA | $10.8 \pm 0.8$ M $\Omega$ | $17.2 \pm 0.3$ pf/cm | $-145.8 \pm 9.1$ pA  |
| HPK 48                 | $1.62 \pm 0.41$ nA | $10.8 \pm 0.3$ M $\Omega$ | $17.2 \pm 0.3$ pf/cm | $-141.4 \pm 14.4$ pA |
| mean value             | 1.61 nA            | 10.88 M $\Omega$          | 17.2 pf/cm           | -143.1 pA            |
| standard deviation (?) | 0.23 nA            | 0.44 M $\Omega$           | 0.21 pf/cm           | 6.68 pA              |
| bad strips %           | 0.04 %             | 0.26 %                    | 1.82 %               | 0.09 %               |

**Table 5.2:** Averaged p-side stripscan results of Hamamatsu sensors HPK 46, 47 and 48.

## 5.2 Micron

Thirteen wedge sensors, designed for the forward region of the Belle II SVD, were qualified at the QTC Vienna and the results will be summed up in the following section. The sensors tested were:

- Micron 2
- Micron 5
- Micron 6
- Micron 9
- Micron 10
- Micron 11
- Micron 12
- Micron 15
- Micron 17
- Micron 18
- Micron 22
- Micron 23
- Micron 24

### 5.2.1 Global Measurements

The global IV and CV curves are summed up in figures 5.3 to 5.6. Again the specifications of table 3.2 are met perfectly, although breakdown of one sensor (Micron 22) occurs already at 150V, which is quite below breakdown voltage of the other sensors ( $> 200V$ ), but still below the breakdown voltage specified.

### 5.2.2 Stripskans

Complete stripskans were performed as well on the Micron sensors listed above. In tables 5.3 and 5.4 the average values are listed.

Similar to Hamamatsu, only few strips with high leakage current were found as well as pinholes, although compared to the n-sides, on p-sides the amount of bad strips is slightly higher, especially

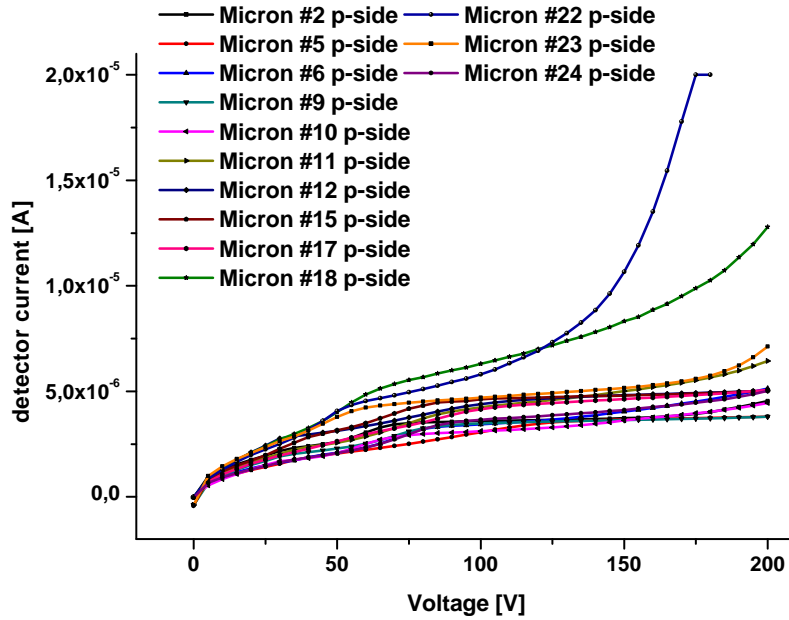


Figure 5.3: Global IV plots of p-sides of Micron sensors.

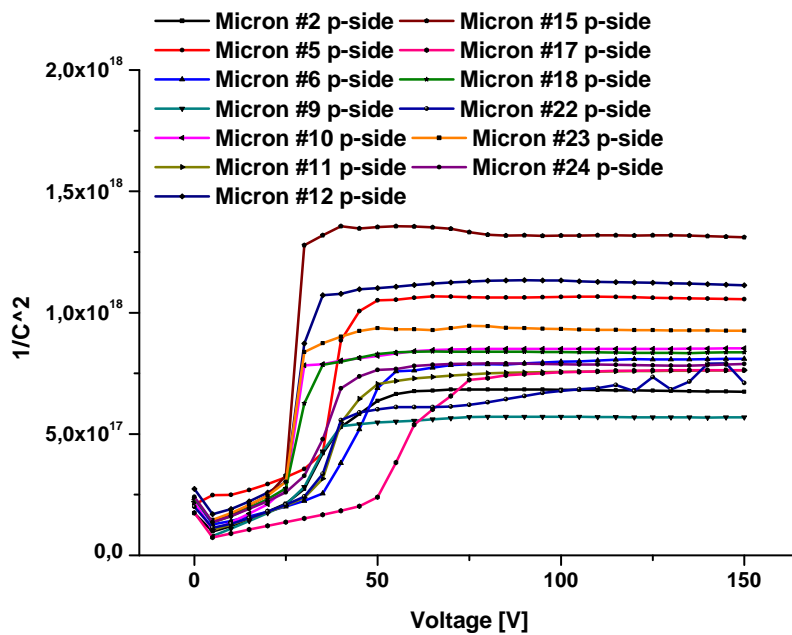


Figure 5.4: Global CV plots of p-sides of Micron sensors.

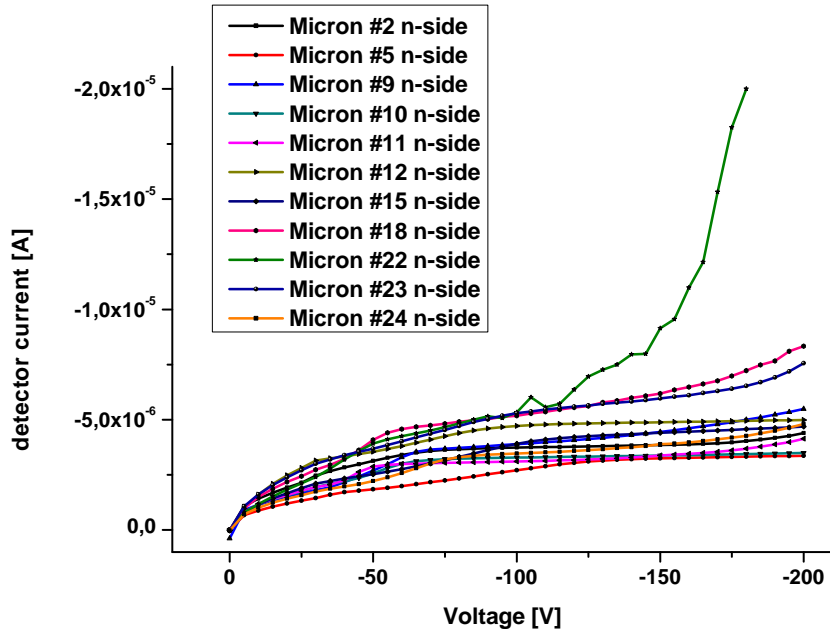


Figure 5.5: Global IV plots of n-sides of Micron sensors.

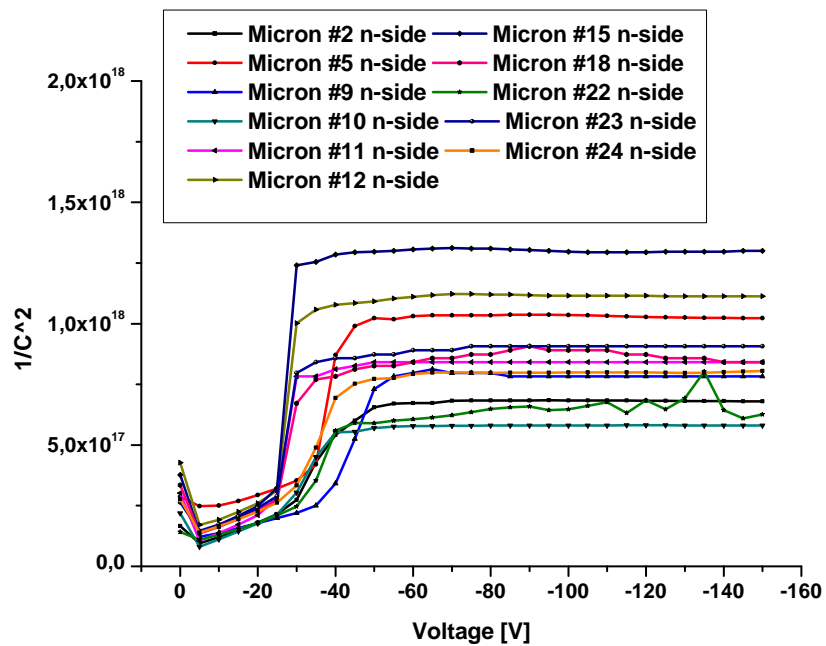


Figure 5.6: Global CV plots of n-sides of Micron sensors.

concerning high strip currents and bad  $R_{poly}$  values.

The corresponding plots to these measurements are found in the appendix.

| n-sides average        | $I_{strip}$         | $R_{poly}$                | $C_{AC}$             | $I_{diel}$           |
|------------------------|---------------------|---------------------------|----------------------|----------------------|
| Micron #2              | $-3.73 \pm 0.68$ nA | $37.8 \pm 3.9$ M $\Omega$ | $30.2 \pm 0.2$ pf/cm | $-160.2 \pm 15.4$ pA |
| Micron #5              | $-2.97 \pm 0.59$ nA | $43.2 \pm 6.3$ M $\Omega$ | $29.4 \pm 0.3$ pf/cm | $-194.9 \pm 8.3$ pA  |
| Micron #6              | $-3.64 \pm 0.85$ nA | $40.5 \pm 3.9$ M $\Omega$ | $31.1 \pm 0.5$ pf/cm | $-183.7 \pm 11.4$ pA |
| Micron #9              | $-3.2 \pm 0.58$ nA  | $33.6 \pm 2.9$ M $\Omega$ | $29.7 \pm 0.2$ pf/cm | $-213.0 \pm 10.9$ pA |
| Micron #10             | $-3.22 \pm 0.60$ nA | $46.0 \pm 4.2$ M $\Omega$ | $29.2 \pm 0.3$ pf/cm | $-145.7 \pm 8.3$ pA  |
| Micron #11             | $-3.92 \pm 0.66$ nA | $41.5 \pm 5.1$ M $\Omega$ | $29.6 \pm 0.3$ pf/cm | $-147.3 \pm 8.8$ pA  |
| Micron #12             | $-4.51 \pm 0.70$ nA | $51.4 \pm 3.9$ M $\Omega$ | $29.1 \pm 0.2$ pf/cm | $-152.6 \pm 8.3$ pA  |
| Micron #15             | $-3.65 \pm 0.60$ nA | $64.4 \pm 7.5$ M $\Omega$ | $30.5 \pm 0.3$ pf/cm | $-143.2 \pm 10.4$ pA |
| Micron #17             | $-3.63 \pm 0.58$ nA | $47.4 \pm 6.0$ M $\Omega$ | $30.1 \pm 0.2$ pf/cm | $-218.4 \pm 9.4$ pA  |
| Micron #18             | $-4.33 \pm 1.23$ nA | $41.0 \pm 4.4$ M $\Omega$ | $29.3 \pm 0.2$ pf/cm | $-162.7 \pm 14.7$ pA |
| Micron #22             | $-4.26 \pm 0.86$ nA | $28.9 \pm 2.5$ M $\Omega$ | $29.2 \pm 0.3$ pf/cm | $-150.1 \pm 14.5$ pA |
| Micron #23             | $-4.25 \pm 0.63$ nA | $44.1 \pm 5.1$ M $\Omega$ | $28.7 \pm 0.2$ pf/cm | $-144.3 \pm 9.1$ pA  |
| Micron #24             | $-3.34 \pm 0.85$ nA | $40.5 \pm 7.0$ M $\Omega$ | $29.6 \pm 0.3$ pf/cm | $-162.7 \pm 10.4$ pA |
| mean value             | -3.75 nA            | 43.1 M $\Omega$           | 29.7 pf/cm           | -167.7 pA            |
| standard deviation (?) | 0.85 nA             | 4.84 M $\Omega$           | 0.27 pf/cm           | 10.8 pA              |
| # bad strips %         | 0.27 %              | 1.05 %                    | 0.12 %               | 0.27 %               |

**Table 5.3:** Averaged n-side stripscan results of Micron sensors.

| p-sides average        | $I_{strip}$        | $R_{poly}$                | $C_{AC}$             | $I_{diel}$           |
|------------------------|--------------------|---------------------------|----------------------|----------------------|
| Micron #2              | $2.20 \pm 0.40$ nA | $37.9 \pm 3.1$ M $\Omega$ | $16.0 \pm 0.4$ pf/cm | $-160.0 \pm 9.1$ pA  |
| Micron #5              | $2.35 \pm 0.58$ nA | $62.0 \pm 7.7$ M $\Omega$ | $11.4 \pm 0.9$ pf/cm | $-153.6 \pm 11.8$ pA |
| Micron #6              | $2.01 \pm 0.35$ nA | $45.4 \pm 3.6$ M $\Omega$ | $15.9 \pm 0.6$ pf/cm | $-203.1 \pm 21.8$ pA |
| Micron #9              | $2.25 \pm 0.34$ nA | $33.7 \pm 2.7$ M $\Omega$ | $14.8 \pm 0.9$ pf/cm | $-258.3 \pm 30.1$ pA |
| Micron #10             | $1.71 \pm 0.60$ nA | $37.5 \pm 5.5$ M $\Omega$ | $16.9 \pm 0.1$ pf/cm | $-208.4 \pm 10.3$ pA |
| Micron #11             | $3.15 \pm 0.78$ nA | $39.3 \pm 2.0$ M $\Omega$ | $15.7 \pm 0.2$ pf/cm | $-188.3 \pm 12.1$ pA |
| Micron #12             | $2.75 \pm 0.47$ nA | $51.4 \pm 4.3$ M $\Omega$ | $15.6 \pm 0.1$ pf/cm | $-169.7 \pm 14.3$ pA |
| Micron #15             | $1.76 \pm 0.45$ nA | $45.6 \pm 4.4$ M $\Omega$ | $16.8 \pm 0.1$ pf/cm | $-149.5 \pm 11.8$ pA |
| Micron #17             | $2.08 \pm 0.50$ nA | $34.8 \pm 2.2$ M $\Omega$ | $13.1 \pm 1.2$ pf/cm | $-154.2 \pm 12.5$ pA |
| Micron #18             | $3.82 \pm 0.67$ nA | $47.4 \pm 4.3$ M $\Omega$ | $14.9 \pm 0.4$ pf/cm | $-169.4 \pm 22.3$ pA |
| Micron #22             | $2.72 \pm 0.86$ nA | $39.7 \pm 4.4$ M $\Omega$ | $16.7 \pm 0.9$ pf/cm | $-197.1 \pm 17.8$ pA |
| Micron #23             | $2.57 \pm 0.76$ nA | $44.9 \pm 7.2$ M $\Omega$ | $17.0 \pm 0.7$ pf/cm | $-162.7 \pm 12.5$ pA |
| Micron #24             | $2.57 \pm 0.42$ nA | $46.1 \pm 4.9$ M $\Omega$ | $14.2 \pm 0.6$ pf/cm | $-195.3 \pm 15.8$ pA |
| mean value             | 2.46 nA            | 43.5 M $\Omega$           | 15.3 pf/cm           | -182.3 pA            |
| standard deviation (?) | 0.42 nA            | 4.31 M $\Omega$           | 0.50 pf/cm           | 15.6 pA              |
| # bad strips %         | 1.50 %             | 1.95 %                    | 0.66 %               | 0.53 %               |

**Table 5.4:** Averaged p-side stripscan of Micron sensors.

### 5.3 Conclusion

On the Hamamatsu sensors of the 2nd batch no pinhole was found and the amount of noisy strips is clearly below 1%. The results are satisfactory to the requirements listed in table 3.2. It is also remarkable the detector current and capacitance hardly differ among the three sensors tested, as can be seen in figures 5.1 and 5.2. At 100 V, the dark current of each sensor is below  $4 \mu\text{A}$ .

The Micron sensors also meet the requirements of table 3.2 with the exception of the poly resistor, which on both sides is clearly above  $40 \text{ M}\Omega$ . For determining the amount of erroneous strips in tables 5.3 and 5.4, this was not taken into consideration. The poly resistance is considered to be erroneous if it differs dramatically from the average values of an individual sensor. Also, there are more noisy strips and pinholes on Micron sensors, especially on p-sides and in contrast to the Hamamatsu batch the detector currents and capacitances of differ more significantly, as seen in figures 5.3 to 5.6. On some of the Micron sensors the dark current at 100 V is above  $4 \mu\text{A}$ .

On both Hamamatsu and Micron sensors, the n-side strip leakage current is higher than on the p-side and there is trend for lower strip numbers to have a higher leakage current on Hamamatsu sensors. On Micron sensors, n-side strip current increases with growing strip number, on p-sides no such features were found. See figures 5.7 to 5.10.

The most important results from these measurements are that basically all the specifications of tables 3.1 and 3.2 are satisfied and that the number erroneous strips is clearly below 1% on Hamamatsu sensors and below  $\approx 2\%$  on Micron sensors.

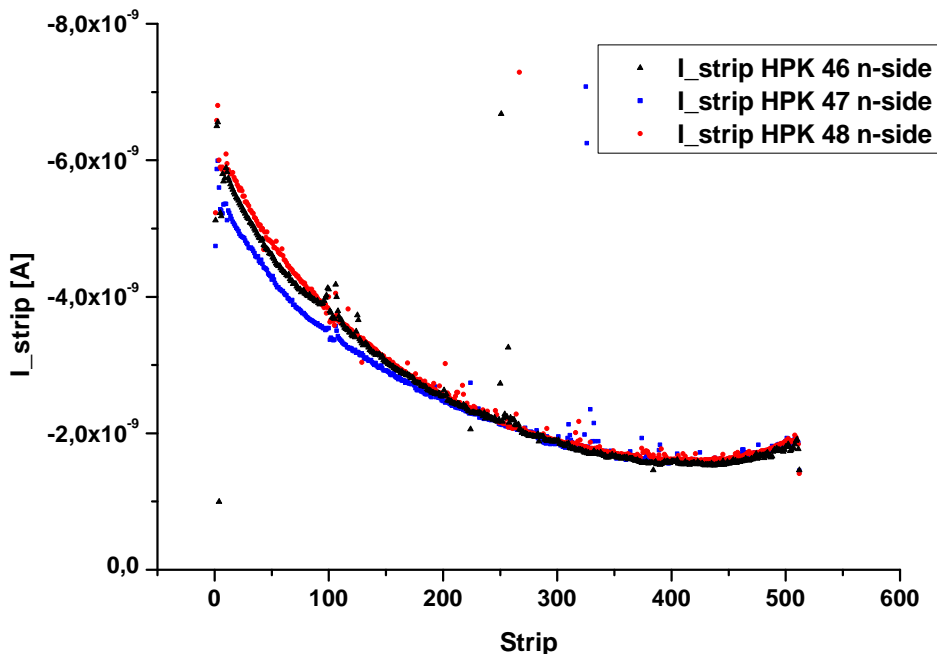


Figure 5.7: Strip leakage current on HPK n-sides.

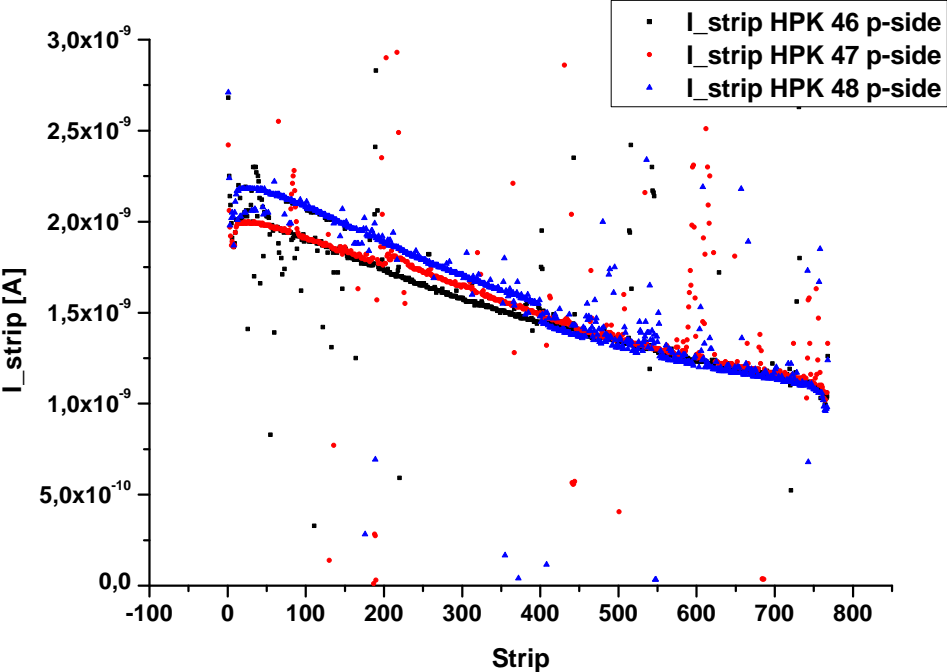


Figure 5.8: Strip leakage current on HPK p-sides.

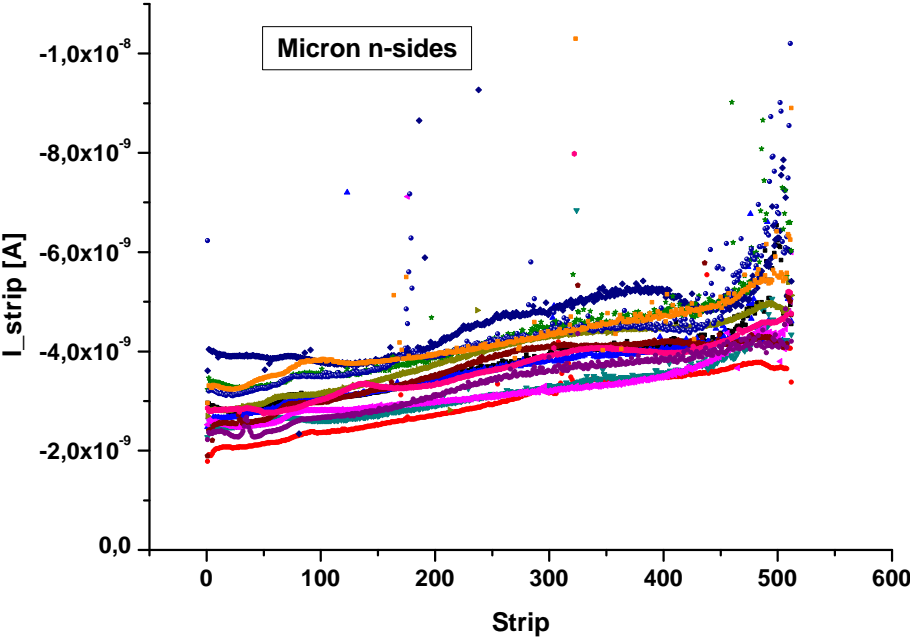
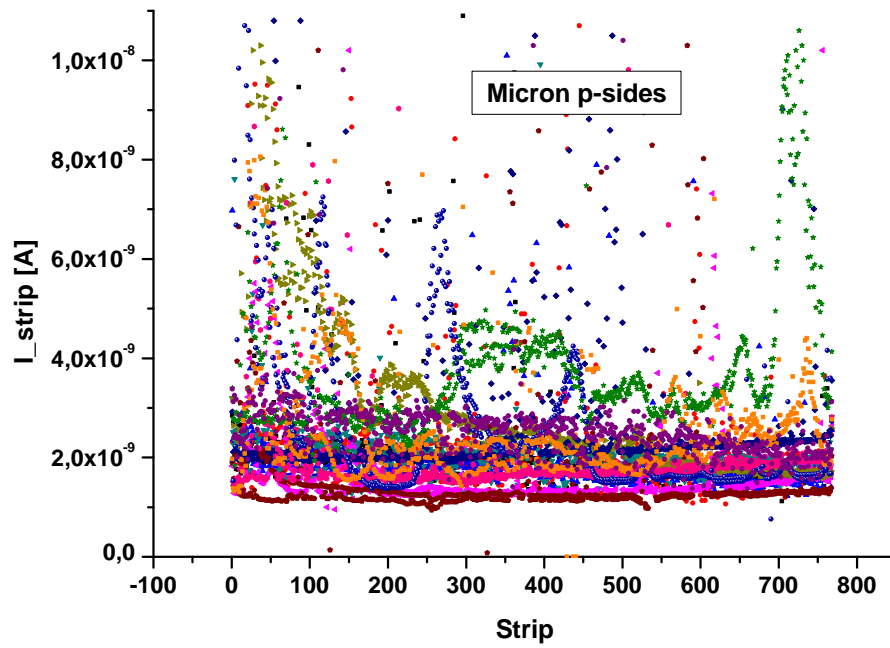


Figure 5.9: Strip leakage current on Micron n-sides.



*Figure 5.10: Strip leakage current on Micron p-sides.*

### 5.3. CONCLUSION



## Chapter 6

# Interstrip resistance

Measuring the *interstrip resistance* is a new method introduced to the QTC Vienna.

The interstrip resistance is defined as the resistance between the strip implants. Large values are desired here, because the charge separation between the individual strips is important for spacial resolution of the detector.

The expected values are above several hundreds of giga  $\Omega$ , which calls for a special measurement method, since the bias resistors, which are in the orders of several tens of mega  $\Omega$ , are in parallel to the interstrip resistance. The equivalent circuit is shown in figure 6.1. According to the

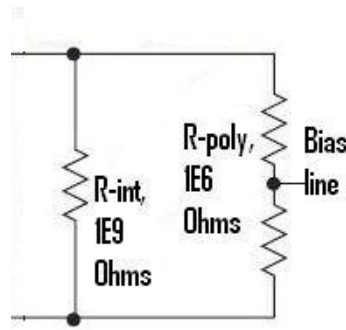


**Figure 6.1:** Equivalent circuit of the interstrip measurement.

formula of a parallel network

$$\frac{1}{R_{tot}} = \frac{1}{R_1} + \frac{1}{R_2}, \quad (6.1)$$

where  $R_2$  denotes the series connection of the two poly resistors, hence

$$R_2 = R_{poly1} + R_{poly2}, \quad (6.2)$$

the total resistance of such a network is

$$R_{tot} = \frac{R_1 \cdot R_2}{R_1 + R_2}. \quad (6.3)$$

Considering the orders of magnitude, this equation becomes

$$R_{tot} \approx \frac{10^9 \cdot 10^6}{10^9 + 10^6} \approx \frac{10^{15}}{10^9} \approx 10^6. \quad (6.4)$$

Furthermore, the source voltage used for this measurement shouldn't exceed certain limits. Since the bias voltage usually is in the order of  $10^2$  Volts, the voltage for the resistance measurement is desired to be kept as low as possible, around 0.5 to 3 Volts, in order to not disrupt the electric field strength near the measurement point. The HV is applied on the backplane, while the bias line is grounded (see sec 3.4). If an additional potential is applied on a DC pad, the effective bias voltage of this very strip is subject to change.

Considering a typical interstrip resistance of about  $100 \times 10^9$  Ohms, this means that the accuracy of the measurement circle must be good enough to detect currents down to  $1 \times 10^{-12}$  Amperes. Due to this restrictions a special measurement method has been developed. Instead of using one SMU only to perform a conventional resistance measurement between two strips, measuring the equivalent circuit shown in figure 6.1, the electrometer is employed as well to measure the pA currents separately.

The idea is to use SMU II to ramp a potential on the DC pad of any strip while measuring the current on the DC pad of the neighbouring strip. Therefore, the electrometer is connected to the DC pad of an arbitrary strip (*Strip X*), hence connection (1,4,4) is closed by the switching system (see figure 4.3). As shown in figure 6.2, the low terminal of the SMU II is grounded (by connecting it to the bias line), while the high terminal is connected to the DC pad of *strip X+1*, which corresponds to connections (2,1,4) and (2,4,3), respectively. Because of the voltage being

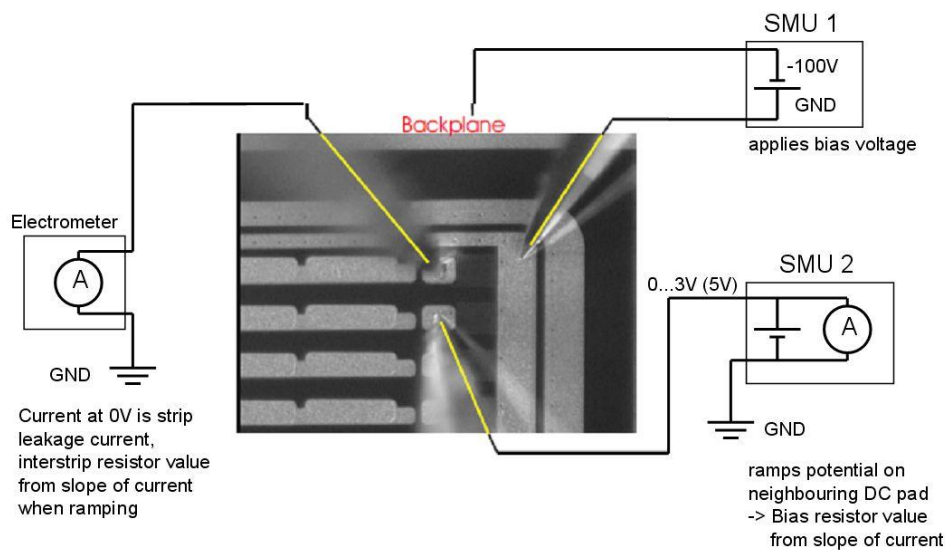


**Figure 6.2:** Configuration for interstrip measurement.

ramped by SMU II, the potential of strip X+1 is subject to change. Since the potential of strip X remains unchanged, there is a current flow between strip X and strip X+1. Furthermore, additional current also flows through the bias resistor of strip X+1, caused by the additional voltage drop of the SMU II. This current can be measured by the SMU II simultaneously.

Thus, the current of strip X, which is detected by the electrometer, is the sum of the regular strip leakage current and the additional current arising from the potential difference caused by the voltage ramp of the SMU II on the neighbouring strip. For each voltage step the current is measured resulting in an IV curve, the inverted slope of which represents the value of the interstrip resistance between strip X and strip X+1. The value at 0 Volts is the normal strip leakage current of strip X. Simultaneously, a similar IV curve is taken by the SMU II, representing the current through the bias resistor of strip X+1.

All in all, this method allows to determine the interstrip resistance, the bias resistor and the

strip leakage current all at once while no additional probe needles to the ones used during the previously used standard measurements are demanded.

The whole measurement procedure is run by LabView software and completely included in the usual stripscan measurement routine. Figure 6.3 shows the measurement circuit in more detail.

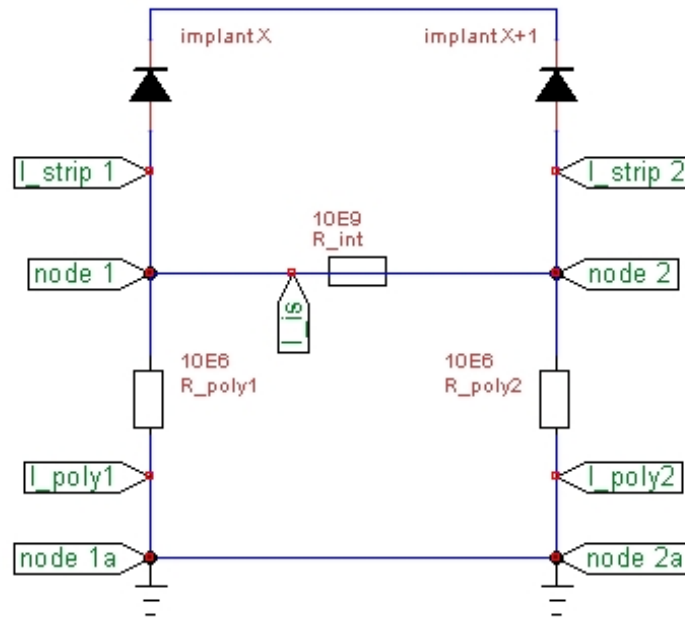


Figure 6.3: Circuit of interstrip resistance measurement.

- implant X: pn junction of strip X
- implant X+1: pn junction of strip X+1
- $I_{poly1}$  and  $I_{poly2}$ : current through the poly resistors of strips X and X+1
- $R_{int}$ : interstrip resistance
- $I_{is}$ : interstrip current
- $R_{poly1}$  and  $R_{poly2}$ : poly resistors of strips X and X+1

The electrometer contacts the DC pad of strip X represented by "node 1", while the SMU II ramps a potential between "node 2" and "node 2a". "Node 1" is grounded as soon as contacted by the electrometer, "node 1a" and "node 2a" are grounded permanently since they represent the bias line. The resulting potential difference between node 1 and node 2 leads to a current flow between them, limited by the interstrip resistance  $R_{int}$ , adding to the permanent strip leakage current  $I_{strip1}$ .

From Kirchhoff's circuit laws it becomes clear, that this measurement method can only be successful if the strip leakage currents  $I_{strip1}$  and  $I_{strip2}$  remain unchanged while the SMU II applies a voltage to node 2, although theoretically this can never be fulfilled. Calculating the whole network of a silicon strip sensor, consisting of several hundred mirror images of the circuit shown in figure 6.3, would demand the knowledge of each diode characteristic. However, simulation based, more theoretically studies of silicon strip detectors are not scheduled to be performed as part of the quality assurance tests at the QTC. A conventional resistance measurement between node 1 and node 2 (as described by formulas 6.1 - 6.4) would even be complicating the matter,

since this requires the SMU II to be floating between node 1 and 2. Hence, the quantities involved in the circuit would be even more subject to change.

## 6.1 Diode characteristics

As mentioned in the previous section, it is more or less presumed that  $I_{strip1}$  and  $I_{strip2}$  remain constant during the measurement. Since an additional voltage, applied to an arbitrary strip, changes the effective bias voltage of this very strip, the diode characteristic of the strip implant is of interest.

Similar to global IV curves, IV curves of each individual strip implants were taken. Since the detectors are operated in reverse bias mode, saturation is expected to be reached at a certain voltage resulting in the typical leakage current of the strip implant. An example is shown in figure 6.4. This example strip shows perfect diode behaviour. At about 60 V saturation is

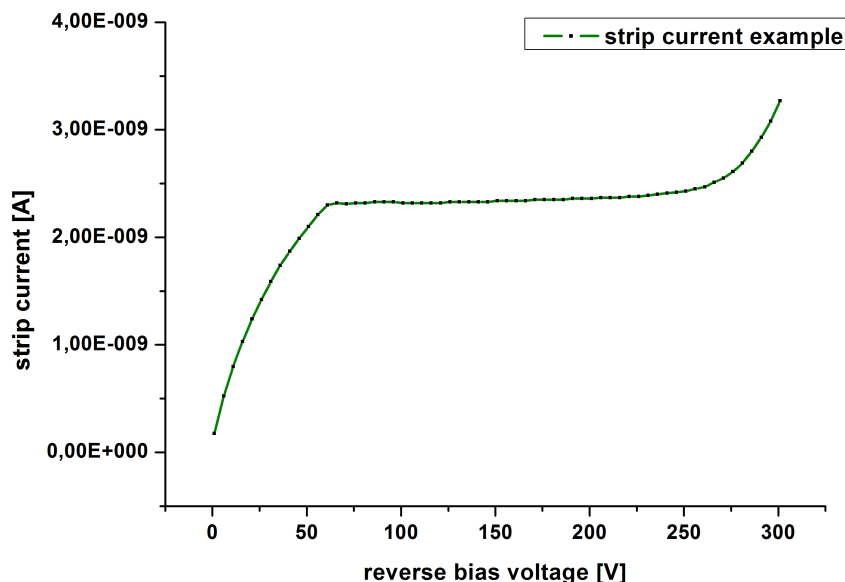


*Figure 6.4: Diode characteristic of an arbitrary strip.*

reached and a constant leakage current flows until breakthrough occurs above 250 V.

An IV curve like that was taken for all or a large number of strips on several Hamamatsu and Micron sensors. The measurement was LabView-run and completely included into the standard stripscan routine. The strip current was measured using the electrometer, while the bias voltage was ramped starting from 0 V to a voltage far beyond depletion, just before the breakdown voltage was reached. The switching configuration was (1,4,4) and (1,1,1). Basically this method can be described as a voltage dependent single strip measurement. At each voltage step, the electrometer returned ten values, out of which an average strip current has been calculated. Additionally, global IV curves also were measured for each bias voltage ramp that was performed. This measurement method appeared to be long term, eventually taking two weeks to be completed on a double sided sensor. Furthermore, for yet unknown reasons, the sensors suffered damage from the excessive bias ramping, resulting in an increasing and unstable detector current. Eventually, the detector was driven into compliance. Consequently, only few sensors

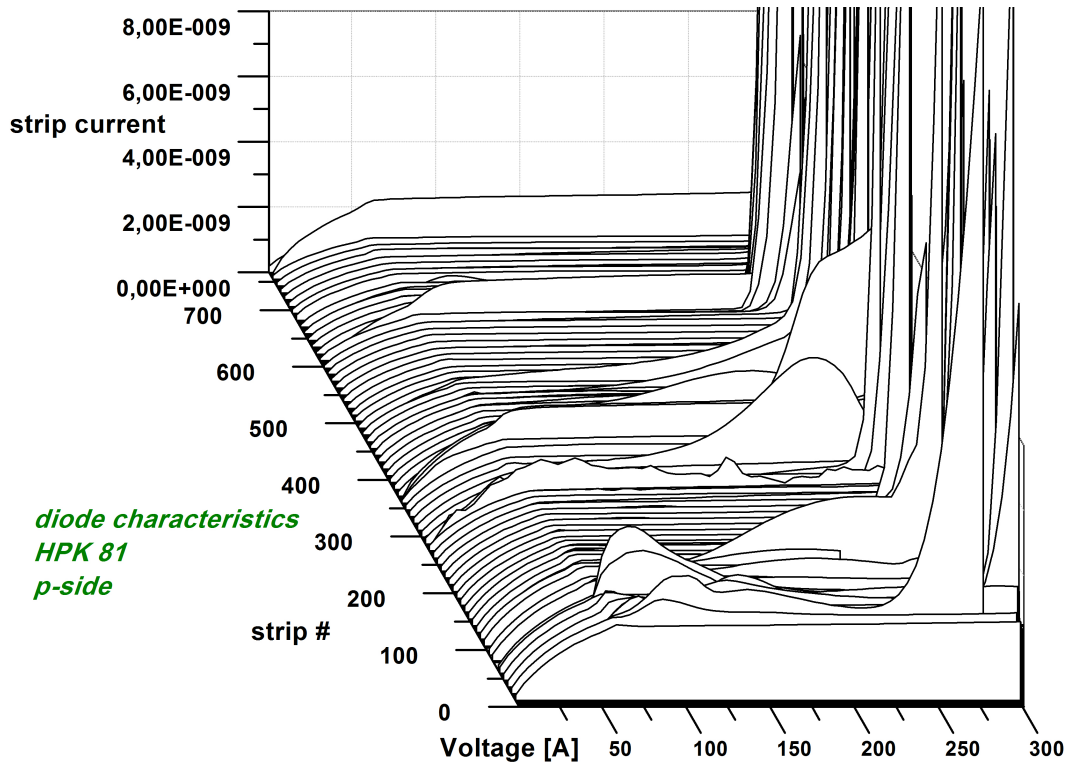


*Figure 6.5: Diode characteristics of Hamamatsu sensor HPK 81, p-side.*

underwent this kind of measurement. The results of one Hamamatsu and one Micron sensor will be outlined in this section. It is assumed that the results are representative for the corresponding batches of the individual sensors.

Figures 6.5 and 6.6 are three dimensional plots of the diode characteristics on p-sides of Hamamatsu sensor HPK 81 and Micron sensor 14, respectively. Some extremely noisy strips were removed afterwards from the plots due to better visibility. For reasons explained above, on the Micron sensor the stripscan was not completed.

Quite obvious, the shapes of the IV curves on the Hamamatsu and the Micron sensor look different. While the diode characteristics of the Hamamatsu sensor look similar to the expected behavior (see figure 6.4), on the Micron sensor there seem to be unstable regions, especially around 100 V. Actually 100 V is the typical bias voltage. The plot in figure 6.6 suggests that a Micron sensor may be operated at higher bias voltages. Furthermore, on the Hamamatsu sensor the breakthrough voltage seems to be lower than on the Micron sensor.

N-side diode characteristics are shown in figures 6.7 and 6.8. Again, on the Micron sensor at a bias voltage of 100 V the IV curves still weren't saturated. Also, the stripscans have not been completed due to the damage the sensors suffered from this type of measurement. Actually, the quality of the shape of the IV curves seems to decrease with increasing strip number. It is assumed that this effect is not sensor related, but instead it seems to be a consequence of the progress of the measurement run. However, this measurement type may only be performed as part of a more detailed investigation of particular sensors and not as part of a typical stripscan. There is a major difference of the shapes of n-side and p-side single strip IV curves at rather low bias voltages. On p-sides, the current starts at around 0 V and then increases constantly, while on n-sides, the strip current below a certain voltage is extremely high and then suddenly drops by at least one order of magnitude. This could be explained by the fact that at this voltage the

6.1. DIODE CHARACTERISTICS

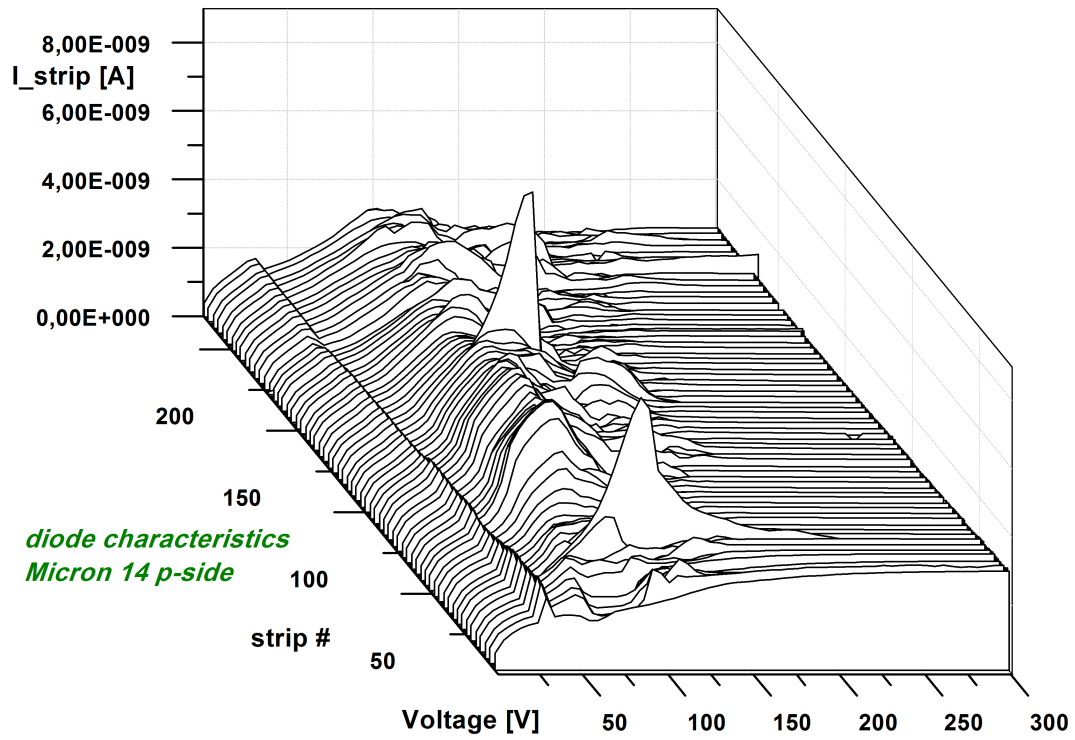


Figure 6.6: Diode characteristics of Micron sensor 14, p-side.

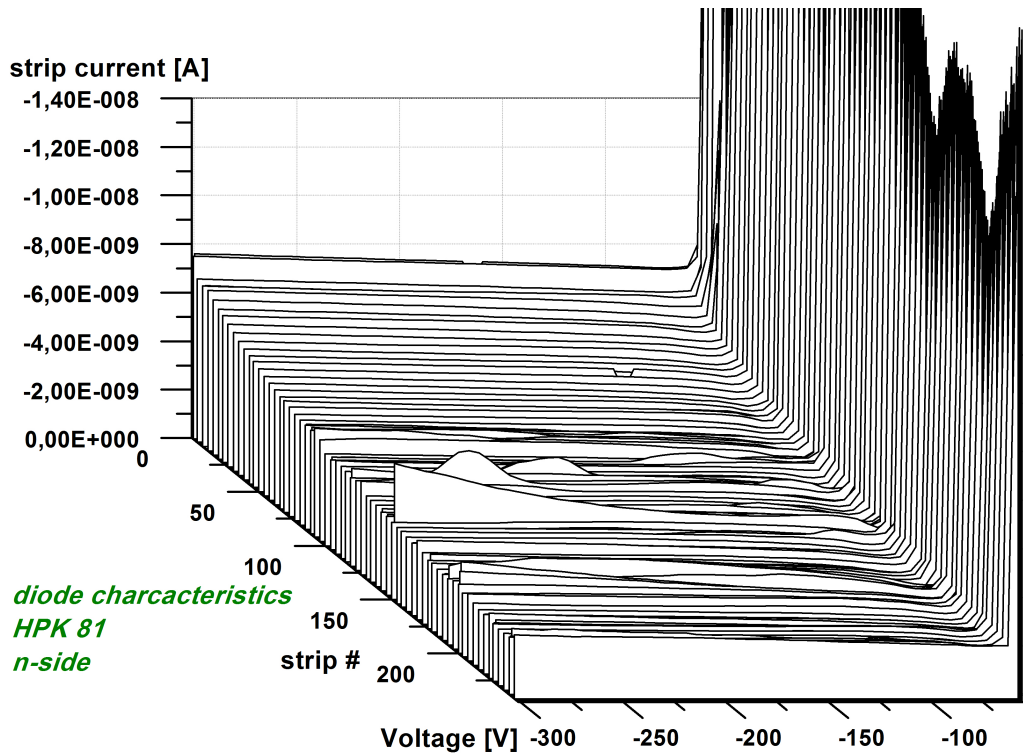


Figure 6.7: Diode characteristics of Hamamatsu sensor 81, n-side.

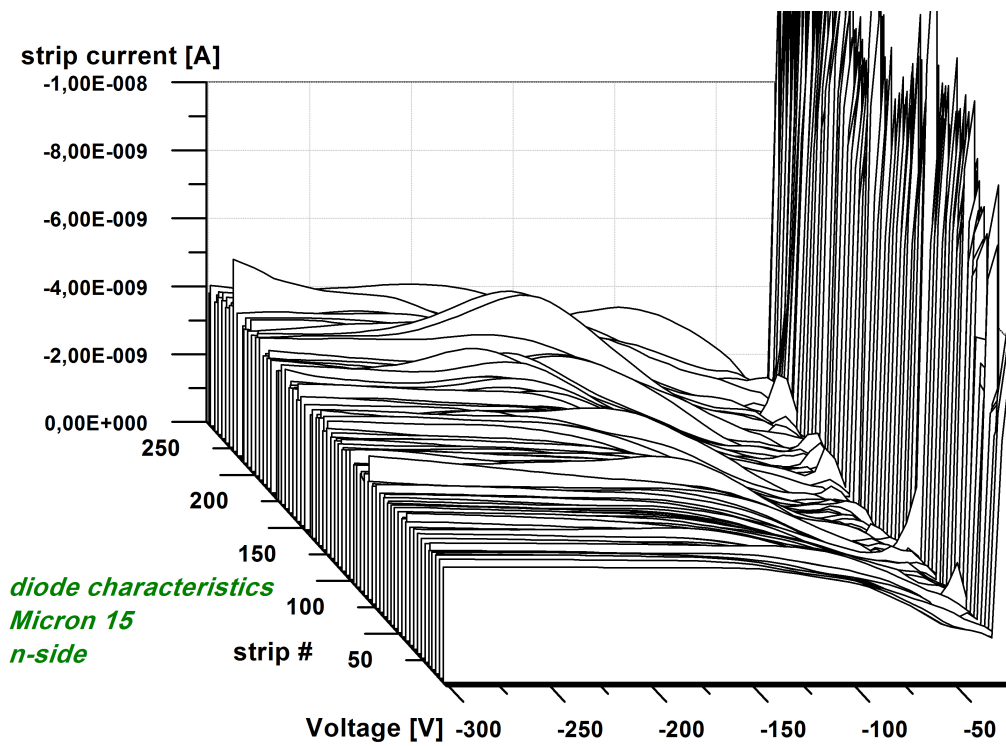


Figure 6.8: Diode characteristics of Micron sensor 15, n-side.

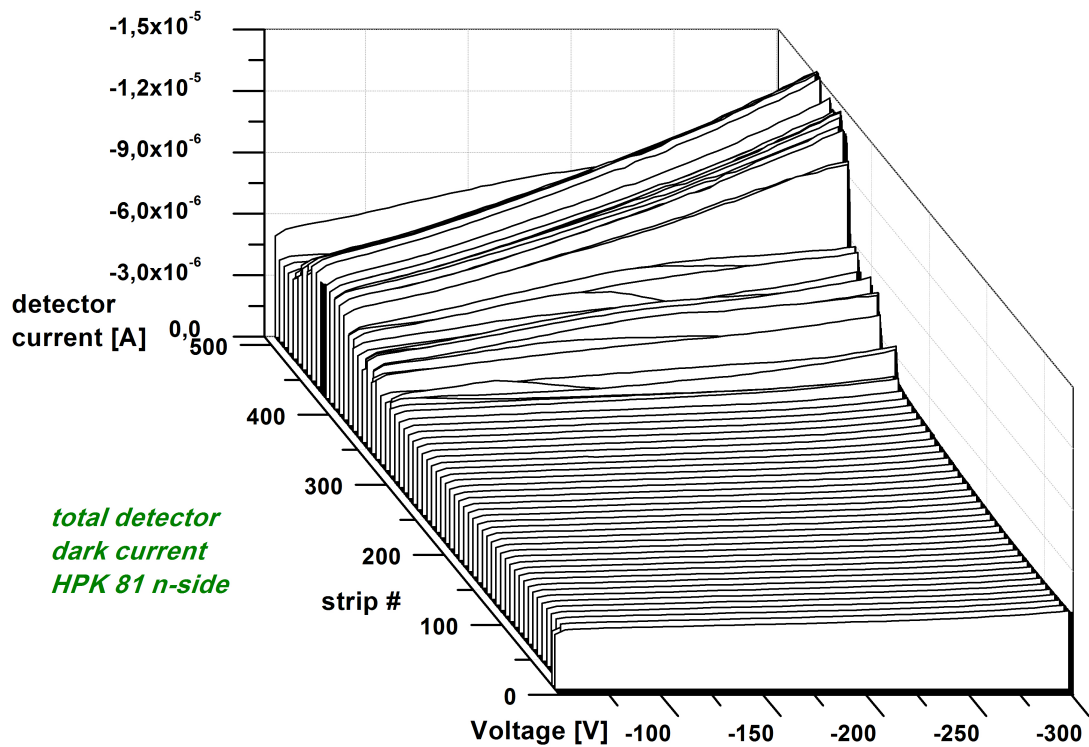


Figure 6.9: Total detector current of Hamamatsu sensor HPK 81, n-side.

## 6.2. INTERSTRIP RESISTANCE MEASUREMENTS

electric field of the depletion zone reaches the implants of the n-side. At lower voltages, this area of the sensor isn't depleted and stronger currents can flow. In order to avoid these high currents, the bias voltage ramps on n-sides were started at higher voltages, usually around -50 Volts.

As described above, also global IV curves were taken at each bias ramp. Figure 6.9 shows a three dimensional plot in the style of the plots of the single strip IV curves of a n-side stripscan on a Hamamatsu sensor. Because the low end of the bias voltage ramp was -51 Volts, mostly the saturated part of the curve is visible only. The IV curves in figure 6.9 indicate the damage the sensor suffered from the measurement. After several hundred strips, the detector current suddenly increases significantly. This damage turned out to be irreversible.

### 6.2 Interstrip Resistance Measurements

At the QTC Vienna, three different methods of measuring the interstrip resistance have been developed and tested on several different sensor types. The goal was not only to determine the exact interstrip resistance, but also to be able to compare the performance of the different methods. Thus, the aim of the results presented in this section is not particularly to give information on the sensors tested, but also to characterize the different measurement methods themselves and point out complications that may disrupt the measurement.

All measurement types basically share the same switching configuration and working principle described at the beginning of this chapter 6. They differ by the voltage that is applied, by the way the electrometer is used and eventually how the resistance is calculated.

#### 6.2.1 Method 1

In the most simple method, the electrometer returns one value for each voltage step. A screenshot of a typical interstrip resistance measurement is shown in figure 6.10. The top IV curve represents the interstrip current, while the bottom curve is the current through the poly resistor. Before the slope can be calculated, the curves are fitted, using the "*Best linear fit*" provided by LabView software. The slopes of the fits then are used to determine the resistance.

Usually four or five voltage steps are performed during the ramp. Considering an interstrip resistance of about 500 G $\Omega$ , which is not an unusual value, this means that there is a current flow of 2 pA/V. If a total voltage of, for example, 2 Volts shouldn't be exceeded, this means that, if four equidistant voltage intervals are used, there is a current of 1 pA per voltage step. Ramping from negative to positive values allows to double the interval sizes without exceeding certain voltage limits. In fact, applying a total voltage of  $\pm 5$  V was found to be unproblematic.

#### Hamamatsu sensors

In figures 6.11 and 6.12, the result of a complete double-sided stripscan on a Hamamatsu sensor is shown. It has to be pointed out, that the overall shape of the plots look similar for all double sided Belle II Hamamatsu sensors, even for different batches. On n-sides, the resistance is constantly increasing with growing strip number. This is believed to be a sensor related effect, not only because observable on all sensors of this type, but also because the result looks very much the same if the direction of the stripscan is inverted. This also holds true for the p-sides. For every measurement the percentage of "*fit ok*" on each side is calculated, see tables 6.1 and 6.2. Tables 6.1 and 6.2 suggest that resistances above 500 G $\Omega$  cannot be measured by the



CHAPTER 6. INTERSTRIP RESISTANCE

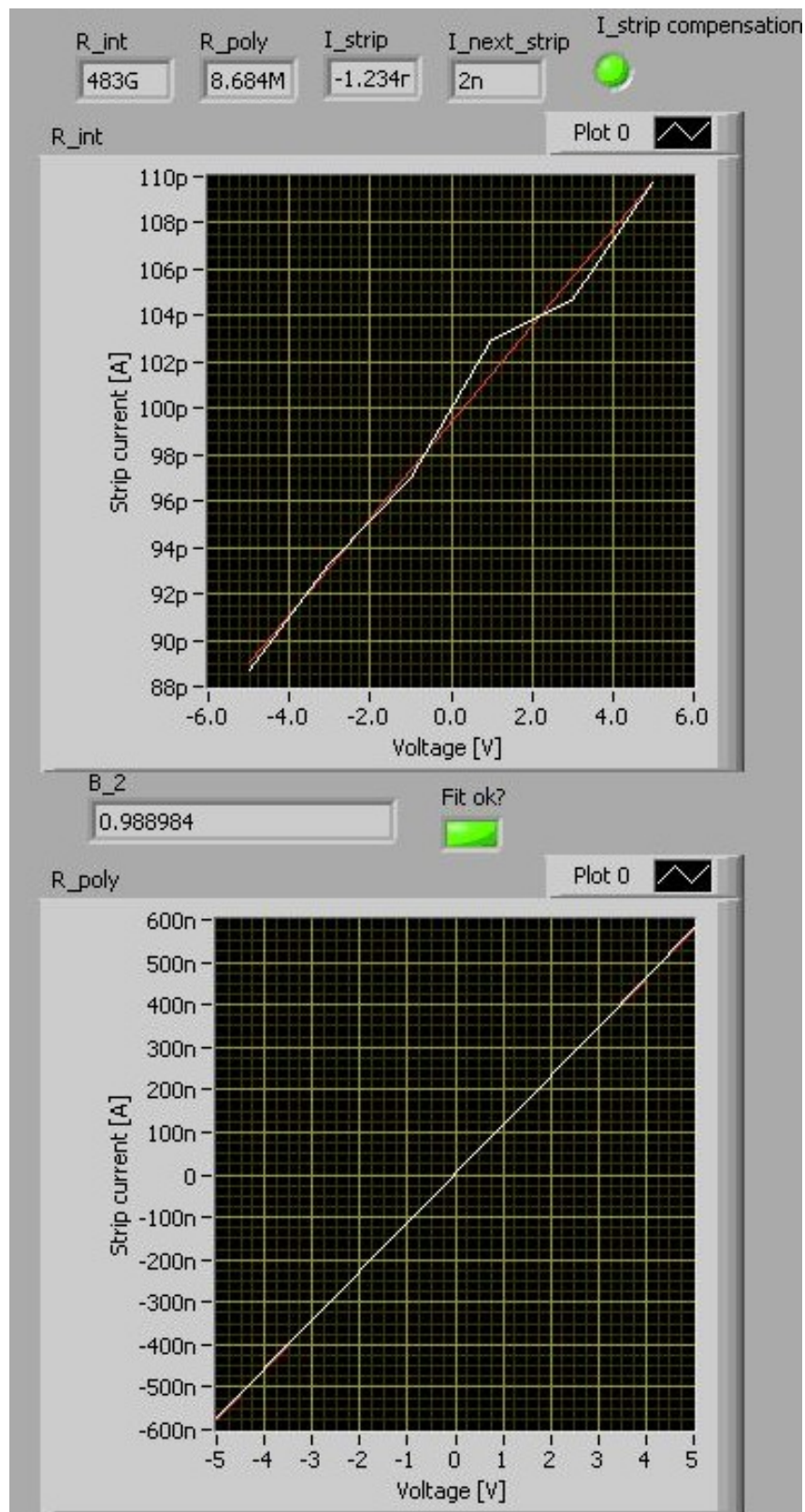


**Figure 6.10:** IV curves of interstrip current (top) and current through poly resistor (bottom). The white lines are the true IV curves, red lines are fits.

6.2. INTERSTRIP RESISTANCE MEASUREMENTS

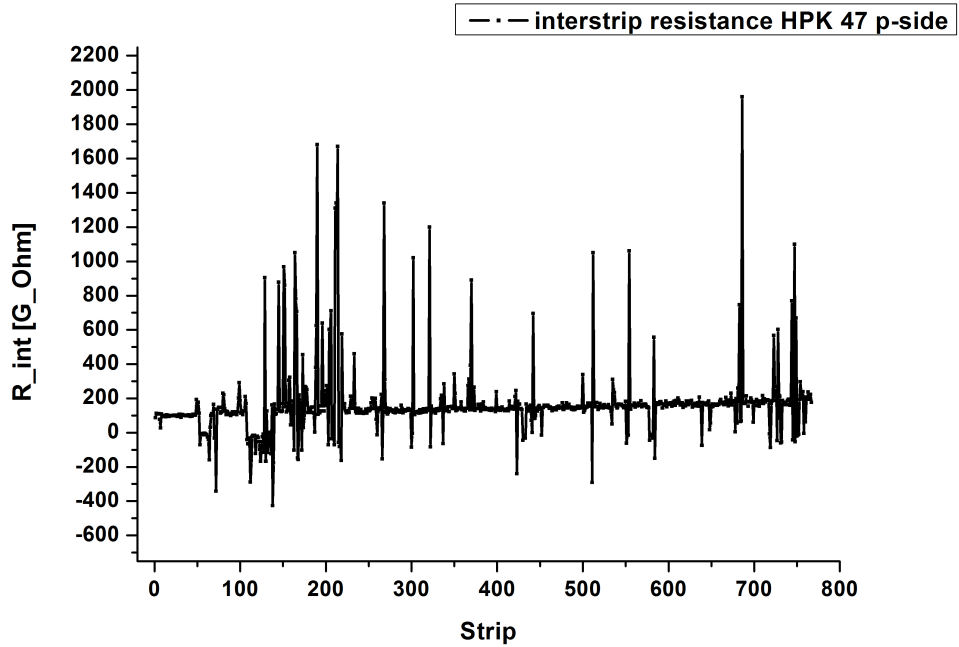


Figure 6.11: Interstrip resistance on p-side of Hamamatsu sensor 47.

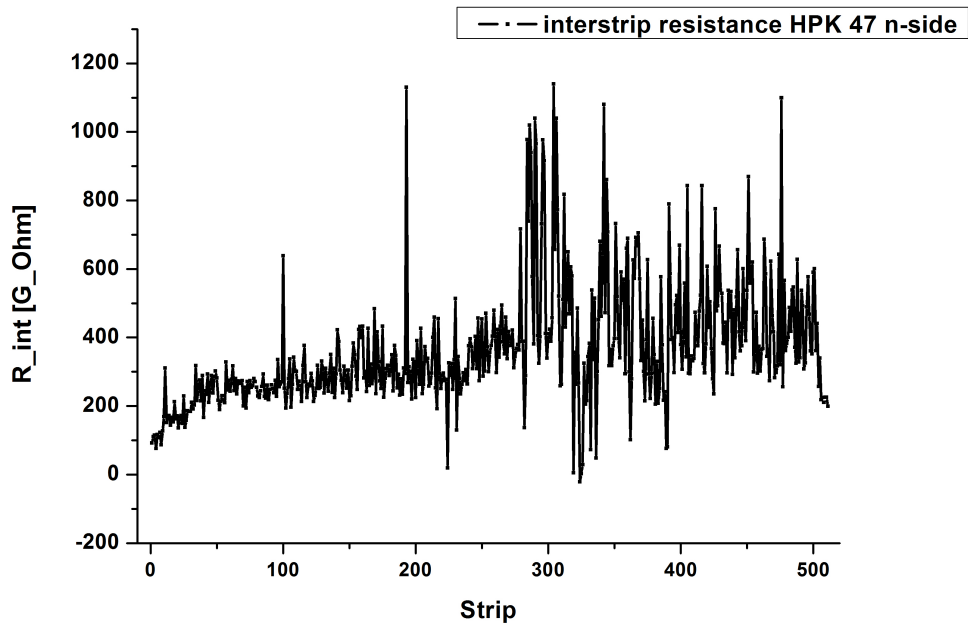


Figure 6.12: Interstrip resistance on n-side of Hamamatsu sensor 47.

CHAPTER 6. INTERSTRIP RESISTANCE

| HPK 47 p-side    | fit ok           | fit failed <sup>1</sup> |
|------------------|------------------|-------------------------|
| mean $R_{int}$   | 150.0 G $\Omega$ | 713.4 G $\Omega$        |
| number of strips | 688              | 100                     |
| fit ok %         | 86.9 %           |                         |

Table 6.1: Interstrip measurement result of HPK 47 p-side

| HPK 47 n-side    | fit ok           | fit failed       |
|------------------|------------------|------------------|
| mean $R_{int}$   | 279.8 G $\Omega$ | 456.1 G $\Omega$ |
| number of strips | 273              | 239              |
| fit ok %         | 53.3 %           |                  |

Table 6.2: Interstrip measurement result of HPK 47 n-side

QTC. However, other measurements showed that resistances even above T $\Omega$  can be measured. Furthermore, the reasons for failed measurements on n- and p-sides seem to be of different nature. This will be discussed in more detail in the next section.

It shall be pointed out here, that on p-sides failed fits most commonly are caused by noisy strips. Many strip scans have shown that the strip leakage currents on n-sides are much more stable than on p-sides. High strip currents also are very unstable themselves and affect the interstrip measurement of both neighboring strips. As discussed in the previous section, stable strip currents are the main premise for the interstrip measurement to work. On p-sides, this condition seems to be fulfilled only up to a smaller degree than on n-sides.

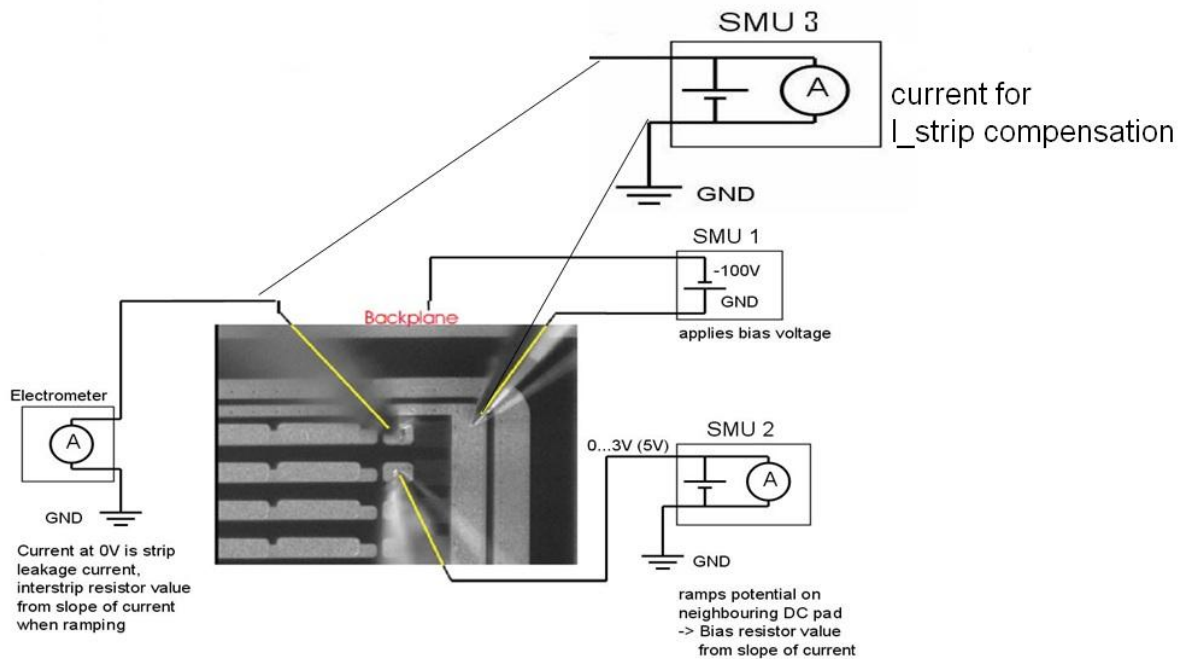


Figure 6.13: Interstrip measurement method involving a third SMU to compensate for the strip leakage current

## 6.2. INTERSTRIP RESISTANCE MEASUREMENTS

### 6.2.2 Method 2

As described at the beginning of section 6, the working principle of the interstrip measurement is to measure the sum of the interstrip current and the strip leakage current. Usually, these two currents differ by three orders of magnitude. Consequently, the aim of this method is to compensate for the offset of the strip leakage current and to only measure the interstrip current. Therefore, a third SMU has been introduced to the measurement setup. The low terminal is connected to the bias line while the high terminal is connected to the DC pad of strip X, see figure 6.13. This configuration allows to compensate for the strip leakage current through the bias resistor. The SMU 3 is connected to the setup in a way that in addition to the connections already used for method 1, (1,4,4), (2,1,4) and (2,4,3), channels (1,4,5) and (2,4,2) have to be closed.

The LabView software has been programmed to basically perform 3 steps when operating the measurement method:

1. measuring the strip leakage current
2. use SMU 3 to compensate for the strip current by applying a current in opposite direction
3. start the usual IV ramp of the interstrip current

This procedure is repeated on each individual strip during a stripscan.

Compared to method 1, the front panel of the measurement Vi was modified and has become multi-functional. Thus, the operator must take care of several parameters. See figure 6.14 for a screenshot of the front panel.

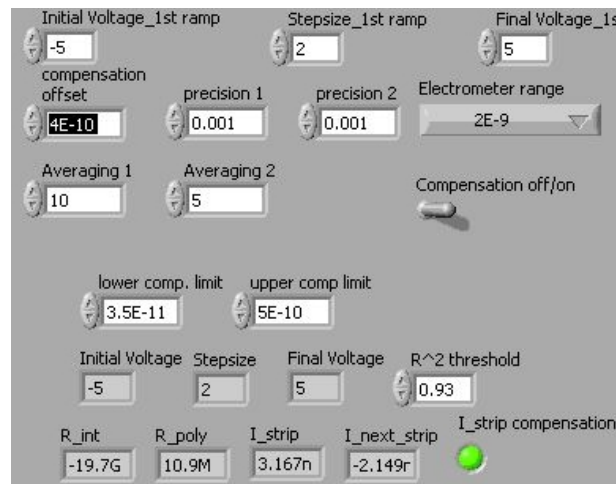


**Figure 6.14:** Front panel of interstrip measurement method involving SMU 3.

- initial voltage, step size, final voltage: The operator can change the voltage intervals during a running strip scan.
- compensation offset: The aim of this method is to compensate for the strip leakage current to be able to run the electrometer within a range that fits the order of the interstrip current. The smallest available ranges of the electrometer are 20 and 200 pA. The operator is free to choose an offset to be left even after compensation. Most measurements were performed at offset currents ranging from 50 to 150 pA. The range limit of the electrometer is 21 and 210 pA. respectively.

- lower/upper compensation limits: the smallest current the Keithley 2410 SMU is able to provide is 50 pA. This means that any range the operator wishes to perform the measurement in can only be "hit" by the electrometer with an accuracy of 50 pA. After the compensation current has been applied in the first place, the software double checks if the current had been compensated successfully. This accounts for the possibility that the strip leakage current can be subject to change after it was measured or that the measurement has been inaccurate. If the remaining current is not within the interval determined by the operator setting "lower" and "upper compensation limits", the software adjusts the compensation current until the current meets this criterion. Together with "compensation offset", this parameters have turned out to be helpful to speed up and stabilize the whole measurement routine. They have been involved for practical reasons.
- precision 1; precision 2: For method 2, the electrometer was configured in a different way. Instead of returning just one current at a time for each voltage step, a loop condition checks if the values being read by the electrometer remain constant to a certain degree. This has proven to be helpful to gain more stable IV curves. Entering a value of 0.01 means that the software starts to read values from the electrometer no sooner until two consecutive current values differ by a maximum of 1 percent. Precision 1 refers to the very first step, precision 2 to the rest of the interval steps of the IV curve. Also, this has been implemented due to practical reasons.
- averaging 1; averaging 2: after the loop that stabilizes the current being read finishes, an array of values is being read by the software out of which an average current is calculated. The operator is free to choose how many values are to be read. Averaging 1 refers to the first step, averaging 2 to the rest of the interval steps.
- Electrometer range: Basically the firmware of the electrometer should be able to switch between different measurement range automatically if necessary. Eventually, this causes problems because sometimes it fails to switch fast enough and as a result error messages are returned. Hence, the operator can adjust the measurement range manually.
- compensation on/off: The operator can switch between method 1 and 2 during a stripscan. If method two is chosen, the indicator " $I_{strip}$  compensation" turns on.

Usually, once the operator has found a set of parameters that work properly, the stripscan can be run automatically. Different sensors may require slightly different sets of parameters.

### Measurements on Hamamatsu sensors

Basically the same sensors tested with method 1 have been measured using method 2 involving strip current compensation. The main results will be presented in this section. The behavior of all the Hamamatsu sensors is quite similar. The results can be regarded as representative for multiple sensors.

As mentioned in the previous section, the electrometer was configured to "wait" until the strip current stabilized itself after each voltage ramp. Nevertheless, all the values returned by the instrument were stored by the software. Moreover, a significant, well reproduceable behavior was found. On Hamamatsu n-sides the interstrip resistance increases with growing strip number. Figure 6.15 showcases the behavior of the current during stabilizing of an arbitrary strip on a Hamamatsu n-side. With growing strip number in Hamamatsu n-sides, this behavior becomes

## 6.2. INTERSTRIP RESISTANCE MEASUREMENTS

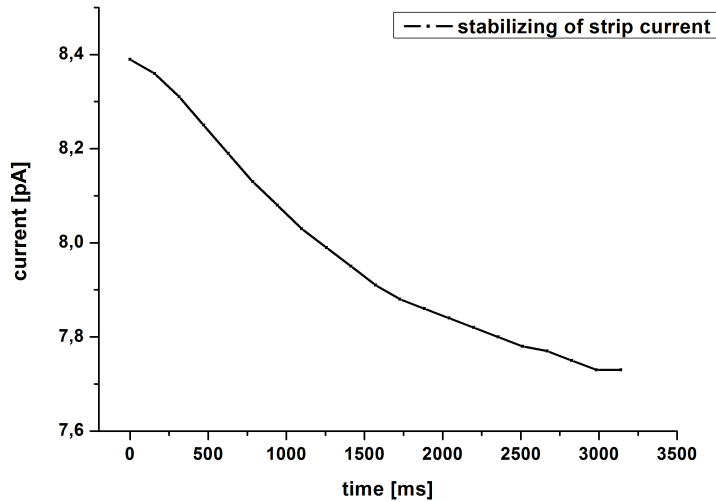


**Figure 6.15:** Current during stabilizing process of an arbitrary strip on a Hamamatsu n-side. The measurement stops if the precision condition 2 is reached (usually 1 "%")

more dominant. At each voltage step the current drops after the voltage has been increased by the SMU 2. In figure 6.15 an overall current drop of approximately 1 pA can be seen. If five voltage steps are performed during the IV ramp, a total or an average drop can be calculated for each strip. In figure 6.16, all average values are plotted over the strip numbers, as well as the interstrip resistance.

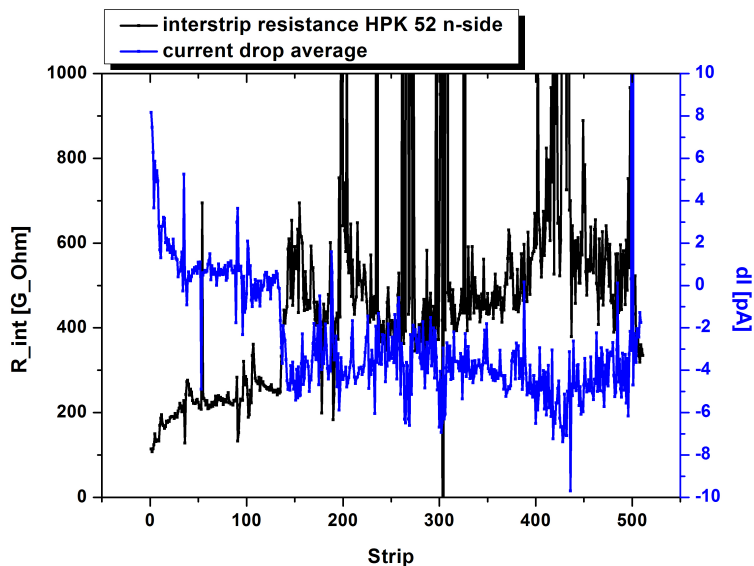


**Figure 6.16:** Interstrip resistance (black) and averaged current drop (blue) of sensor HPK 52.

The data of the plot in figure 6.16 is from a measurement on Hamamatsu sensor 52. The current drop and the increasing interstrip resistance seems to be somehow related. At low strip numbers, the resistance is low and the current drop is positive. This is the opposite case of

## CHAPTER 6. INTERSTRIP RESISTANCE

the situation shown in figure 6.15. Around strip 125 there is a significant rise of the interstrip resistance and the current drop turns negative. Obviously, the overall slope of the IV curve decreases and the current drop is negative and thus the resistance grows. This behavior was found on all Belle II Hamamatsu sensors tested so far but can only be visualized when using method 2. However, on p-sides such a relation was not found.

In figure 6.17, the same plot as in figure 6.16 is shown but the interstrip resistance is inverted.

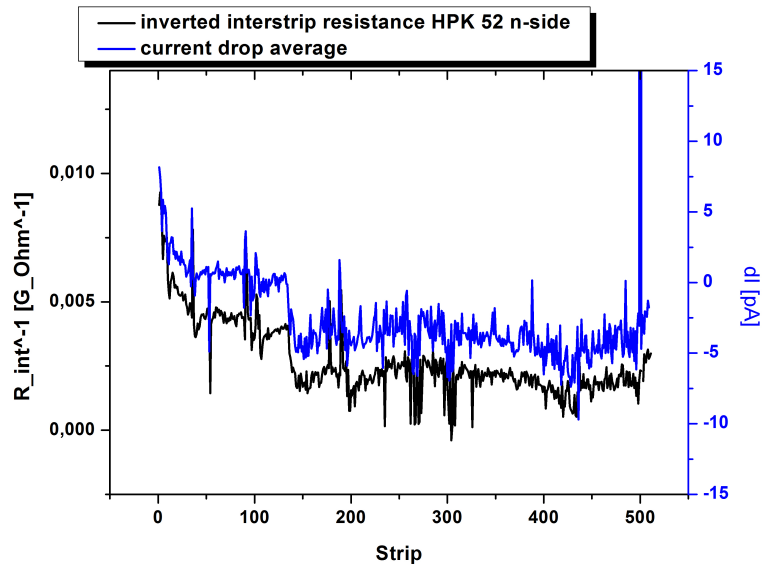


*Figure 6.17: Inverted interstrip resistance and current drop of sensor HPK 52, n-side.*

### Measurements on Micron sensors

On Micron sensor 17 similar measurements have been performed with the following results.

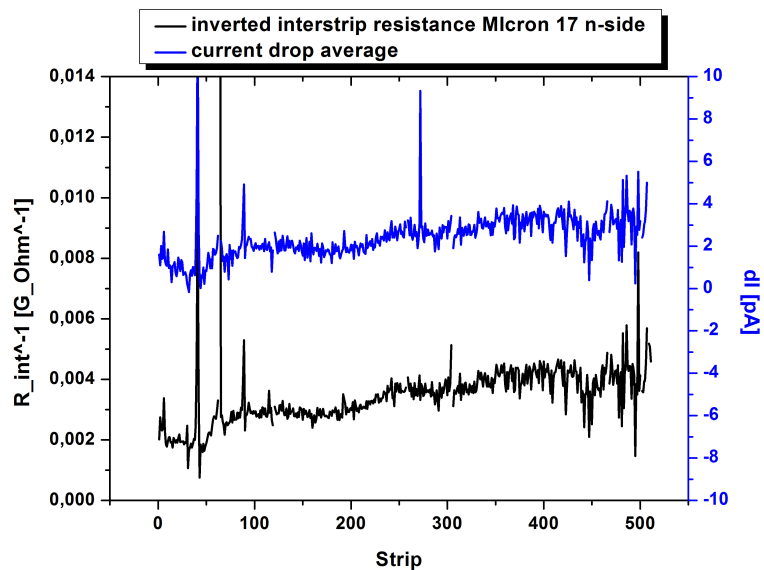


*Figure 6.18: Inverted interstrip resistance and current drop on Micron sensor 17, n-side.*

### 6.2.3 Method 3

The idea of the method is to take into account several effects found during measurements with the other methods and give the operator as much information on the behavior of the strip current and the IV curve as possible.

The concept of reading multiple values from the electrometer was adopted, but a different way of ramping the voltage and calculating the resistance has been developed. The switching configuration is the same as for method 1, hence (1,4,4), (2,1,4) and (2,4,3), although method 2 and 3 can be combined in such a way that the strip leakage current can be compensated for as well when using method 3. The operator has to turn on "I<sub>strip</sub> compensation" on the front panel of the measurement VI shown in figure 6.10.

In figure 6.19 the concept is discussed in more detail. The idea is to ramp the voltage in ascending and descending manner and calculate an average of the measured strip current at each voltage step. Figure 6.19(a) shows the concept of the voltage ramp, in figure 6.19(b) an ideal example of the expected shape of the resulting IV curve is plotted. This is the kind of curve that the operator will get to see on the front panel of the measurement VI. It has to be pointed out that this in fact represents an  $I(t)$  curve, with the voltage steps not shown on a separate axis, but being represented by the sudden skip of the current, indicated on the y-axis. Method 3 has a

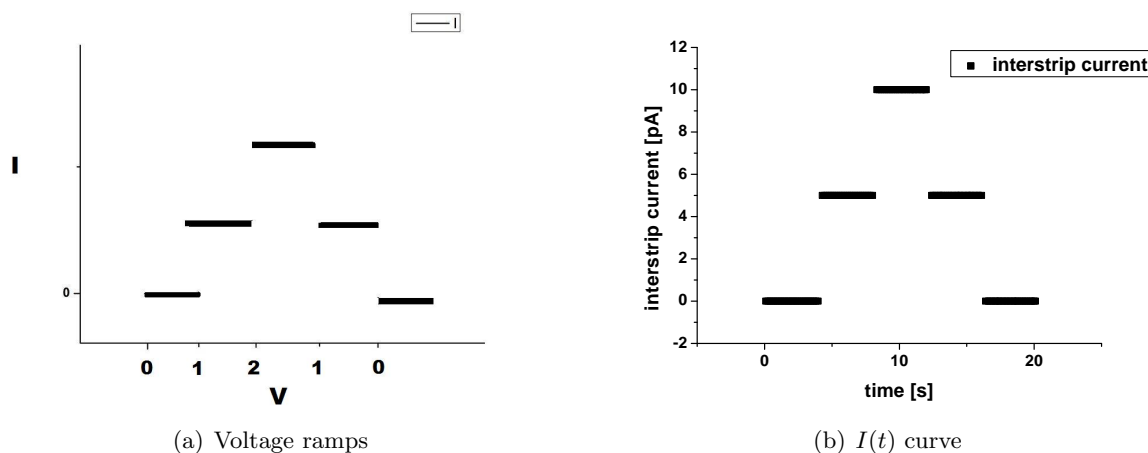


**Figure 6.19:** Voltage ramps (a) and resulting  $I(t)$  curve (b) of Method 3

front panel of its own which pops up as soon as the measurement has been started, see figure 6.20.

The electrometer measures the current of strip X while the SMU 2 ramps a potential on strip X+1. The operator determines how many values the electrometer must return before the SMU 2 continues the ramp and of how many steps the ramp should consist. Currently, the default value for the ramp to start is 0 V, but this may be subject to change. Furthermore, the initial and the final value are the same, by default. The idea is to calculate the interstrip resistance from an array of values that is shaped in a similar way as shown in figure 6.24. Therefore, the average strip current is calculated from the values in between the ramps. Then, using Ohm's law, for each individual step the resistance is calculated, resulting in at least two values (if only one ascending and descending voltage step is performed) yielding an average and a standard deviation. For the example shown in figure 6.20, four steps were performed.

The advantage of this method is that the resulting averaged value compensates for the different slopes of the ascending and descending branches. Similar to the previous methods, the IV curves



## CHAPTER 6. INTERSTRIP RESISTANCE

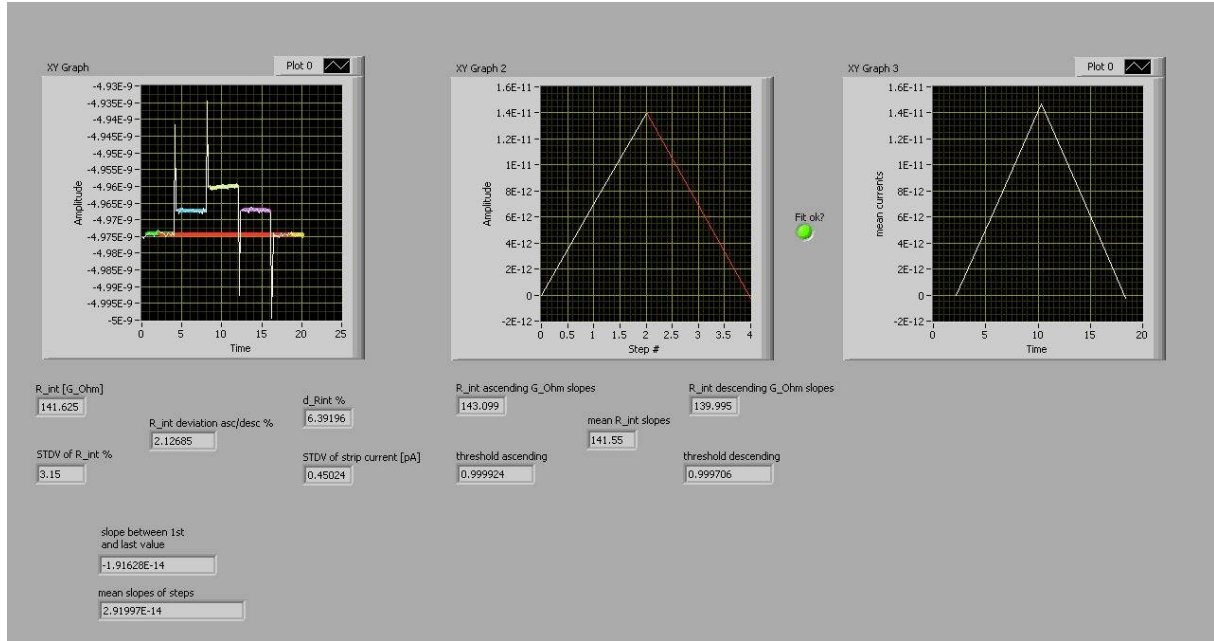


Figure 6.20: Front panel of method 3.

are fitted, but not to determine the slope and the resistance, respectively, but rather to have a "fit ok" or "fit not ok" criterion. The calculation of any resistance only makes sense if the IV curve showcases ohmic behavior to a certain degree.

The indicators on the front panel are as follows:

- Ramp: The strip current during the ramp of SMU 2 is plotted here. The colored lines are fits and indicate which values were taken into account for calculation. The peaks occur each time a GBIP command to continue the ramp is sent to the SMU 2 and are left out of calculation.
- Fits: Indicates the fitted version of "ramp".
- Mean: The averages values between the voltage steps are plotted here. The more similar the shape of "fits" and "mean", the more accurate is the measurement. This is similar to method 1 and 2.
- R<sub>int</sub>: The final value for R<sub>int</sub> is given here.
- stdv of R<sub>int</sub>: Indicates the standard deviation of the multiple R<sub>int</sub> values. The smaller this value is, the more accurate and stable the measurement was.
- stdv of strip current: Standard deviation of the strip current during measurement.
- d<sub>Rint</sub>: Propagation of uncertainty caused by the fluctuations of the strip current. The standard deviation of the strip current is an element of uncertainty for the calculation of the interstrip measurement.
- R<sub>int</sub> deviation: Ratio of resistance of ascending and descending branch. After the stripscan has been completed, the operator has information on the asymmetry of the measurement, hence if a relaxation process as shown in figure 6.24 was dominant over the course of the measurement.

## 6.2. INTERSTRIP RESISTANCE MEASUREMENTS

- slope between first and last value / mean slope of steps: Additionally, the overall slope of the strip current during the measurement is calculated from the colored fits shown in "ramp". In principle, this corresponds to " $R_{int}$  deviation".

Each quantity described above is written to an output file. Furthermore, the operator can activate the "averaging" function of the electrometer. By doing so, the fluctuations of the strip current can be smoothed out. This can be helpful if the detector is particularly noisy or unstable.

### Measurements on Hamamatsu sensors

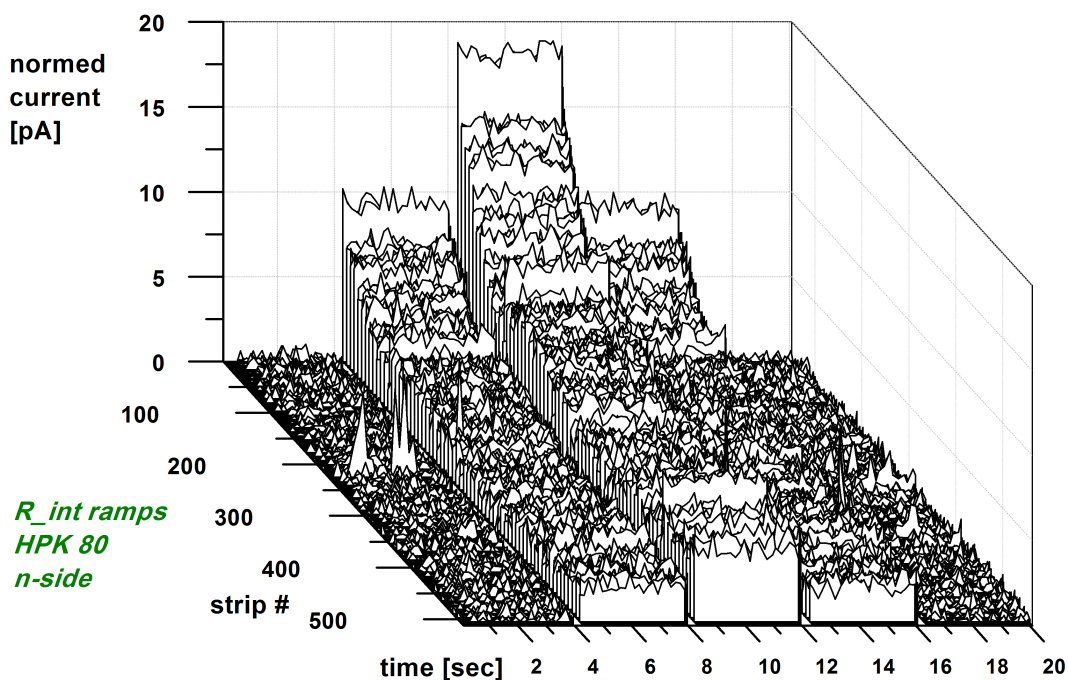


*Figure 6.21:  $R_{int}$  ramps on HPK 80, n-side.*

In figure 6.21 a three dimensional plot of the whole measurement described above is shown. Because each strip has a slightly different strip current and in order to show the relative heights of the ramps only, the strip leakage current was subtracted from each value. The height of the plots and thus the interstrip resistance corresponds to the plot of figure 6.23. The resistance grows with increasing strip numbers. This is the typical behavior of Hamamatsu n-sides. The plot in figure 6.22 shows an average calculated from the single strips plotted in figure 6.21.

### Measurements on Micron sensors

In figure 6.24 the behavior of the strip current during a strip scan and interstrip ramps is shown. This example was taken from measurements on Micron 15 sensor. However, not all sensors show such a behavior, but it is the intention of method 3 to make an accurate interstrip resistance measurement possible even in such cases. It is particularly interesting that there seems to be a relaxation process directly after the DC pad has been contacted by the probe

CHAPTER 6. INTERSTRIP RESISTANCE

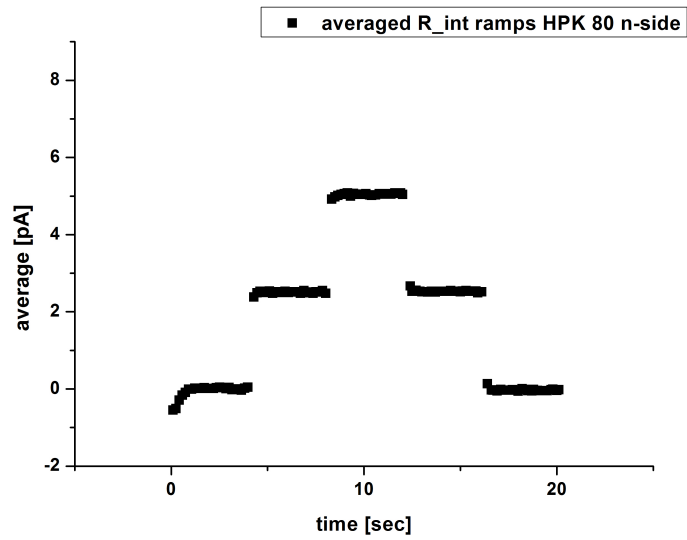


Figure 6.22: Average of all strips of HPK 80 (figure 6.21)

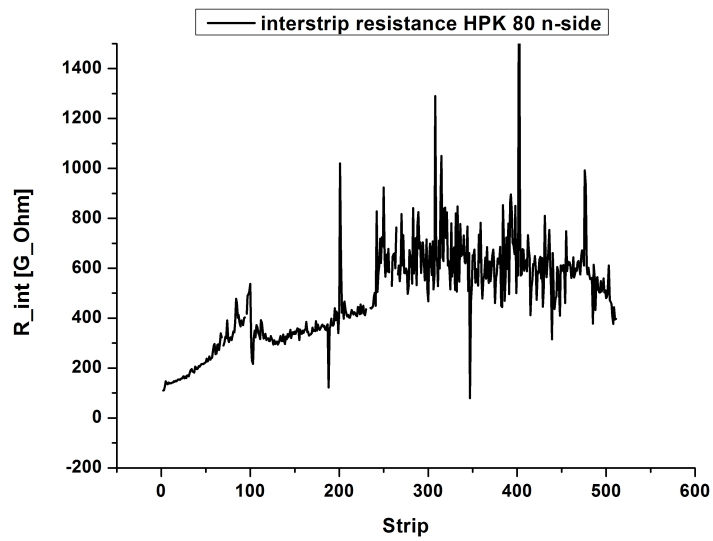
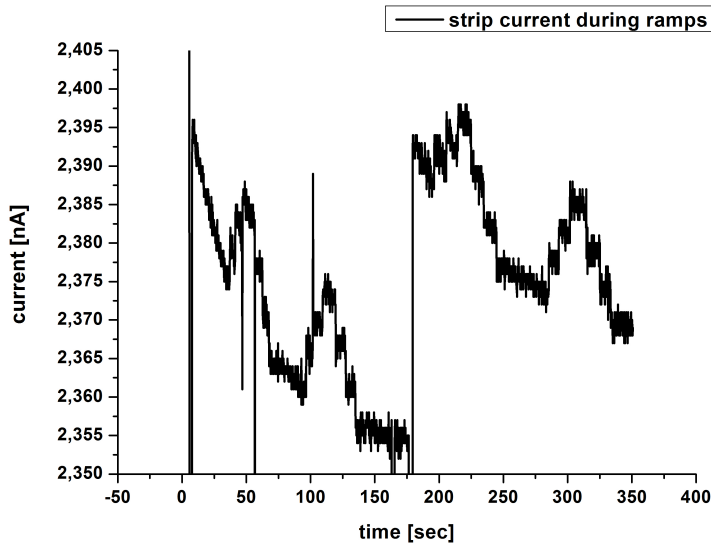


Figure 6.23: Interstrip resistance of HPK 80 n-side.



*Figure 6.24: Behavior of strip current of two consecutive strips during interstrip voltage ramp.*

needle. Consequently, the first ramp is distorted. The ramps consist of three ascending 1 V steps followed by three descending steps of the same size. The second ramp, after approximately 100 seconds, is smoother. One can tell from the shape of the ramps, that the ascending part is likely to yield a higher interstrip resistance than the descending part. Around second 180, the table moves on to the next strip and the measurement is repeated and a similar behavior can be obtained. Furthermore, the fluctuations of the strip current itself are probably high enough to disturb the measurement. Method 3 was designed to take into account such behavior. Figures 6.25 and 6.26 show three dimensional plots of the measurements of n- and p-side on Micron sensor 14. The bias voltage was set to 250 V, taking into account the results of section 6.1. Figures 6.27 and 6.28 show plots of the averages calculated from the single strips and an overall slope can be obtained, with a different sign for each side of the sensor. In figures 6.29 and 6.30 the interstrip resistance, calculated from this measurement using method 3 is plotted over the strip numbers.

## 6.3 Conclusion

Three major findings result from the measurements performed and described in the previous sections:

1. The measurement accuracy is good enough to make possible resistance measurements up to 1 T $\Omega$ . For typical voltages used for the IV ramps, this means that the resolution of the electrometer measuring the current has to be accurate enough to measure 1 pA<sup>2</sup>.
2. Effects causing a failure of the interstrip resistance measurement seem to be sensor related. Since typical interstrip resistances are between 100 G $\Omega$  and 500 G $\Omega$ , this can be deduced from finding 1. Furthermore, especially measurements using method 3 have shown that different sensors display different behavior.

---

<sup>2</sup>1 pA/V = 1 T $\Omega$

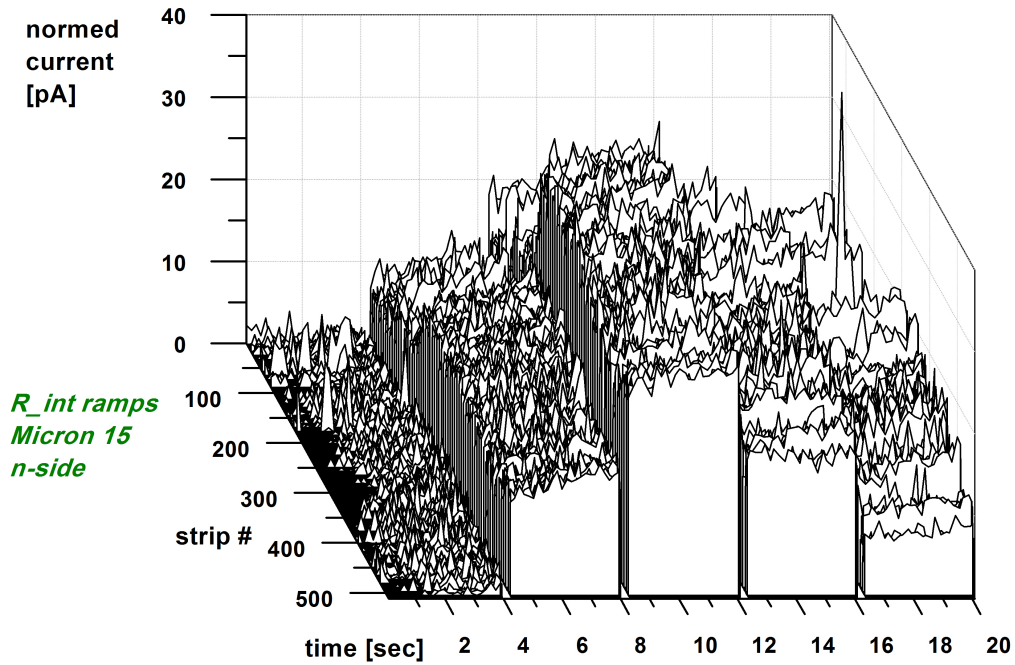


Figure 6.25:  $R_{int}$  ramps on Micron 14 n-side.

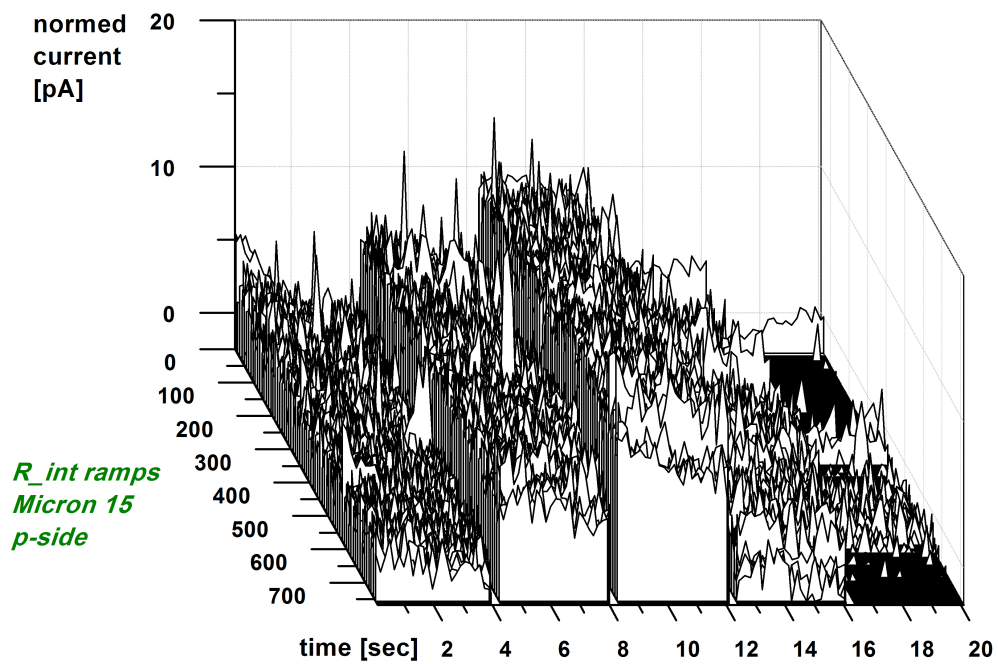


Figure 6.26:  $R_{int}$  ramps on Micron 14 p-side.

6.3. CONCLUSION

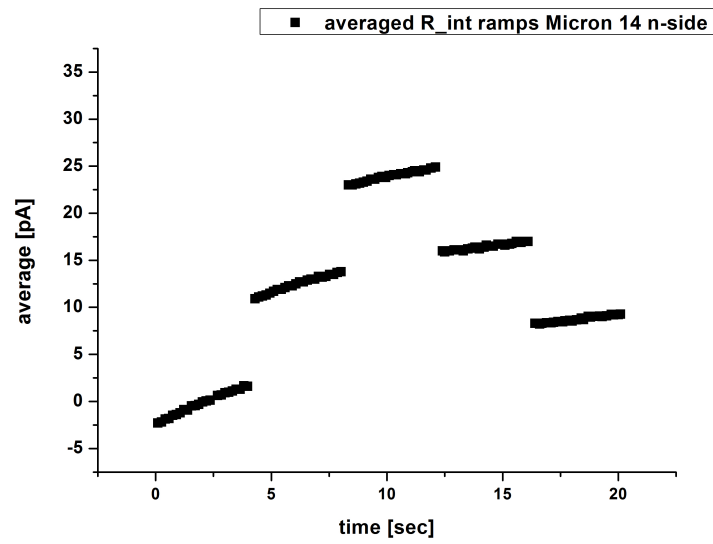


Figure 6.27: Average from single strips of figure 6.24.

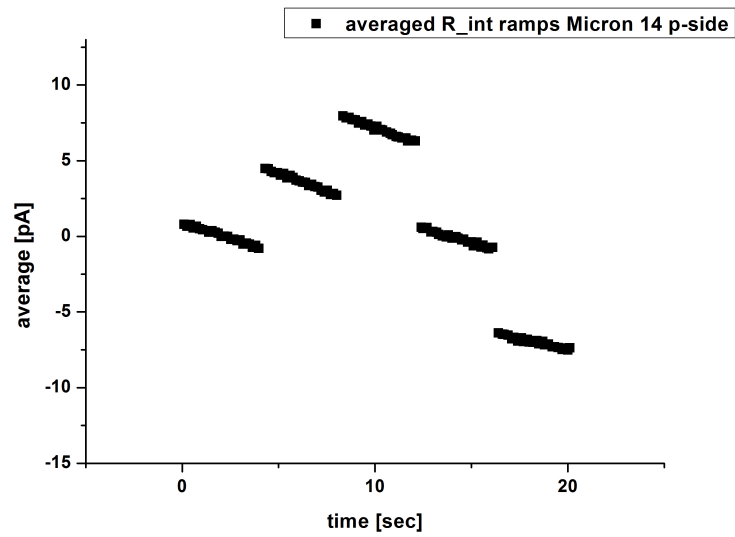


Figure 6.28: Average from single strips of figure 6.25

CHAPTER 6. INTERSTRIP RESISTANCE

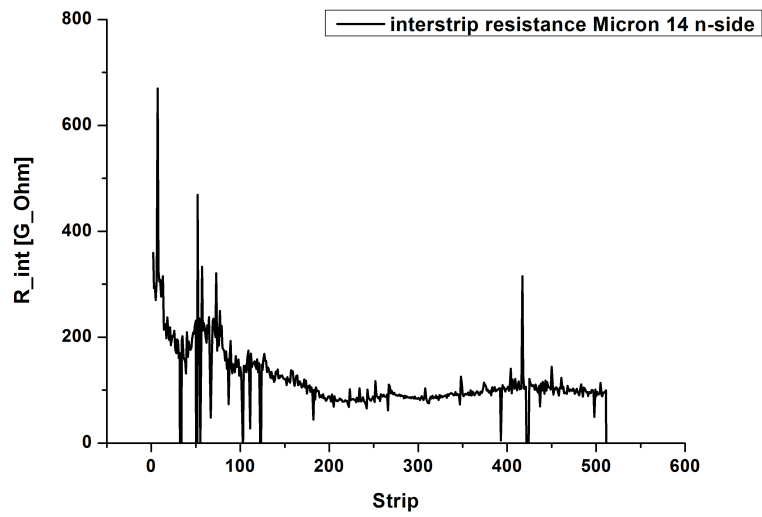


Figure 6.29: Interstrip resistance of Micron 14, n-side.

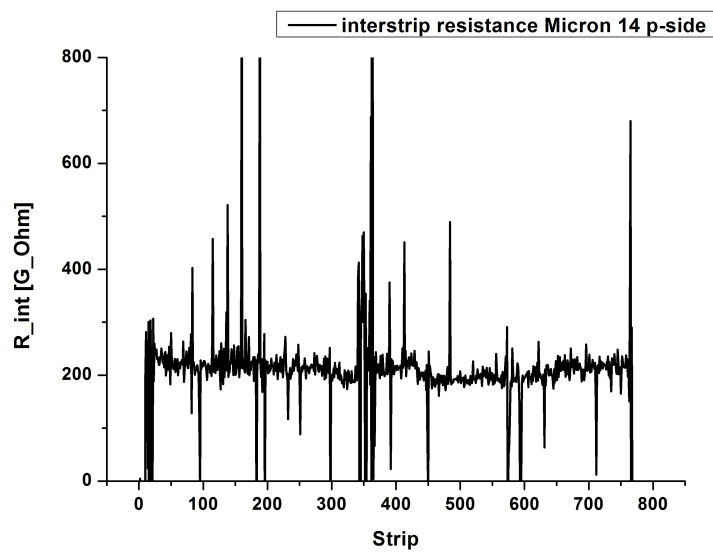


Figure 6.30: Interstrip resistance of Micron 14, p-side.

3. In addition to sensor related effects, there are features that depend on whether the n-side or the p-side of a sensor is measured, as can be seen in figures 6.11 and 6.12.

Besides the sensor related effects, the three different methods that have been developed can lead to slightly different results. Method 3 most likely yields the most accurate, method 1 the least accurate result. The goal of any measurement routine is to be both accurate and fast. However, a compromise depending on the requirements of the operator will have to be made. In case of a sensor that features a stable strip current and that is free of effects as shown in figures 6.27 and 6.28, method 1 will be sufficient.

By developing method 2 and 3, the observation and documentation of different kind of effects have been made possible and the acceptance of the interstrip resistance measurement towards these effect has improved. Further understanding of each of these effects would require simulations and/or better knowledge of the production process of the sensors. Especially for Hamamatsu sensors, the behavior seems to improve with growing batch number. For Micron sensors, only one batch has been available.



## Chapter 7

# Interstrip capacitance

The measurement of the interstrip capacitance is a new method that shall be introduced to the QTC Vienna, together with the interstrip resistance measurement. This section gives an overview on the progress of this method and the most important results obtained so far.

The interstrip capacitance contributes to the electronic noise of the readout system and therefore the measurement of which is desired to be part of the quality assurance. The total capacitance  $C_{tot}$  seen by the readout electronics is

$$C_{tot} = 2 \times C_{int} + C_{back}, \quad (7.1)$$

where  $C_{back}$  denotes the capacitance between the implant and the backplane.

Furthermore, the charge from each strip is capacitively coupled to its neighbor strips, see figure 7.1. After an ionizing particle passes through the detector, the  $e^-h^+$  pairs are close to the original track of the particle. While drifting to the electrodes, diffusion widens the charge carrier distribution. Consequently, the charge cloud is distributed over multiple strips. If analog readout is implemented, the charge center of gravity can be determined and thus a better position resolution can be achieved.

Furthermore, it is not necessary to connect each strip to a readout channel in order to achieve the best position resolution possible. So called *intermediate* - or *non readout strips* can be implemented, the signal of those strips is transferred via capacitive coupling to the readout strips. In doing so, the total number of readout channels and costs can be decreased. The number of intermediate strips may vary depending on the detector type.

## 7.1 Measurement principle

This measurement employs the Agilent 4284A LCR meter. Similarly to the interstrip resistance measurement the DC pads of two neighbouring strips are contacted with probe needles, which are connected to the LCR meter. The switching configuration is (1,4,2) and (2,1,2), connecting the high terminal to "strip X" and the low terminal to "strip X+1". The LCR meter determines the capacitance according to section 4.2.1.

### 7.1.1 Frequency dependent capacitance measurement.

The oscillator voltage levels  $V_{osc}$  used for the measurement of the global detector capacitance and for the coupling capacitance between the metal layer and the implant is 250 mV, while the

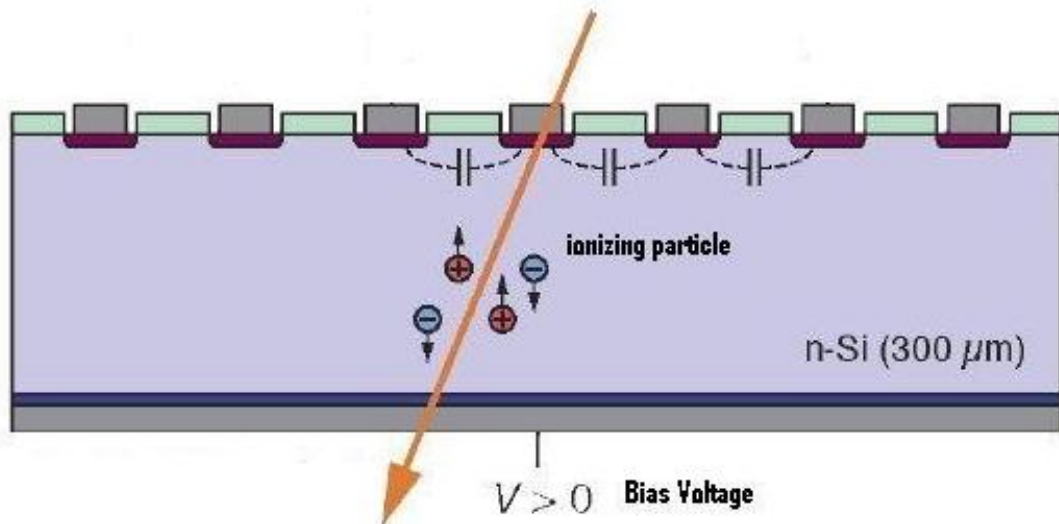


*Figure 7.1: Capacitive coupling between strips. [5]*

frequencies are 1 kHz and 100 Hz, respectively. These are standardized values used during the qualification of the CMS sensors at several QTCs around the world.

The expected values of the interstrip capacitance are several pF [7]. Hence, it is three orders of magnitude smaller than the detector capacitance and 2 orders of magnitude smaller than the coupling capacitance. However, for the determination of the interstrip capacitance, frequency dependent capacitance measurements have been performed, the results of which can be plotted logarithmically.

The quantities measured are the impedance  $Z$  and the phase of the current  $P$ . After choosing an equivalent circuit mode, which is  $C_p - R_p$  for measuring small capacitances, according to the recommendations in the operation manual [13], the LCR meter returns  $C_p$  and  $R_p$ .

## 7.2 Measurements

Due to the frequency dependence of the interstrip capacitance, complete stripscans have not been performed so far.

On AC coupled sensors, the interstrip capacitance between the implants or the capacitance between the metal layers can be taken into consideration. Also a combination of both can be measured. The following results will showcase the behavior of the different capacitances. It has been avoided to perform measurements near the edge regions of the sensor.

### Hamamatsu sensors

Basically, on all double sided Belle II Hamamatsu and Micron sensors the capacitance yields a peak structure when plotted over the frequency, see figure 7.2. The measurements shown in plots 7.2 and 7.3 are from sensor HPK 55 p-side, strip #500.

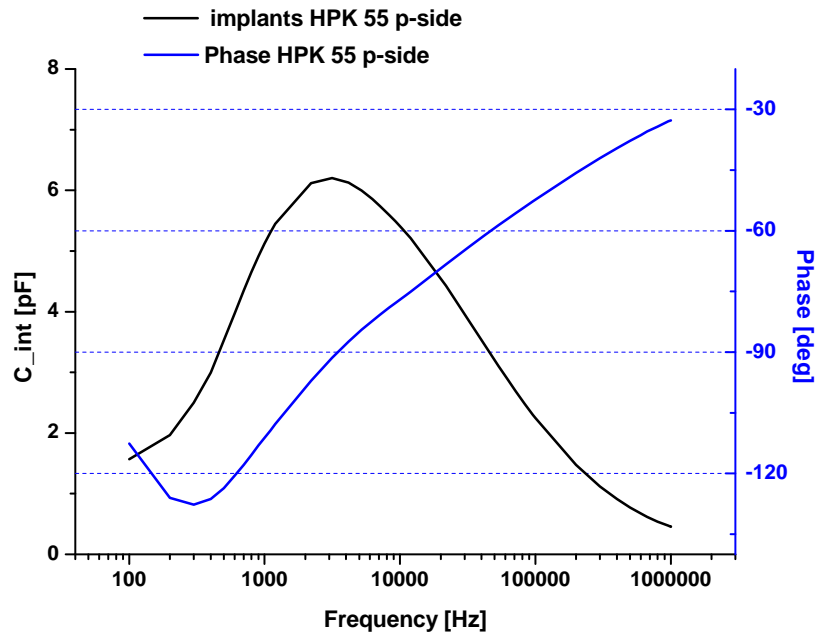


**Figure 7.2:** Frequency dependent interstrip capacitance of implants (black) and phase (blue) on a HPK sensor, p-side.

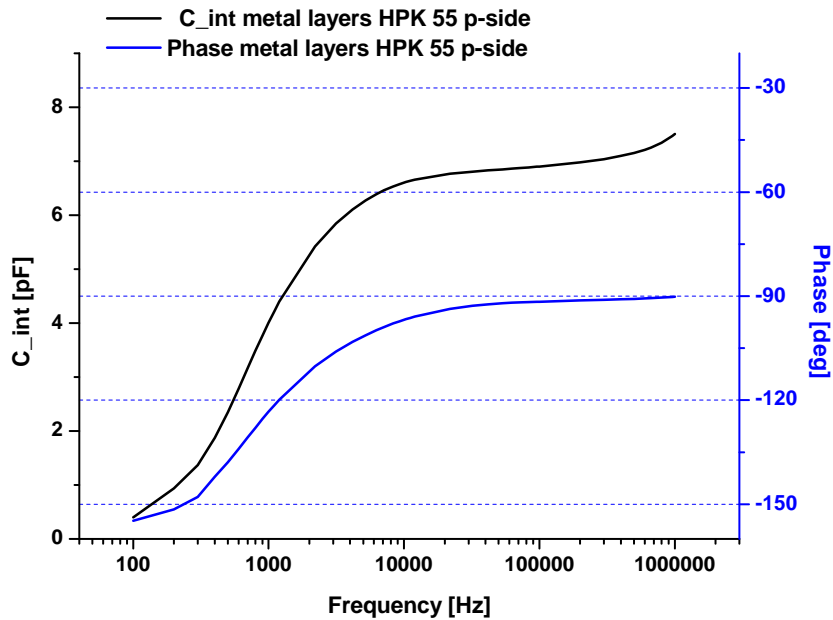


**Figure 7.3:** Frequency dependent interstrip capacitance of metal layers (black) and phase (blue) on a HPK sensor, p-side.

The position of the peak in figure 7.2 is exactly where the phase is  $-90^\circ$  (capacitive behavior). Figure 7.3 shows the frequency dependent interstrip capacitance between the metal layers of two

neighbouring strips. Both phase and capacitance yield different behavior compared to figure 7.2. Actually, the phase reaches  $-90^\circ$  between 100 kHz and 1 MHz. It shall be pointed out here that the upper frequency limit of the Agilent 4284A LCR meter is 1 MHz.

As similar measurement on the n-side of the same sensor is shown in figure 7.4.

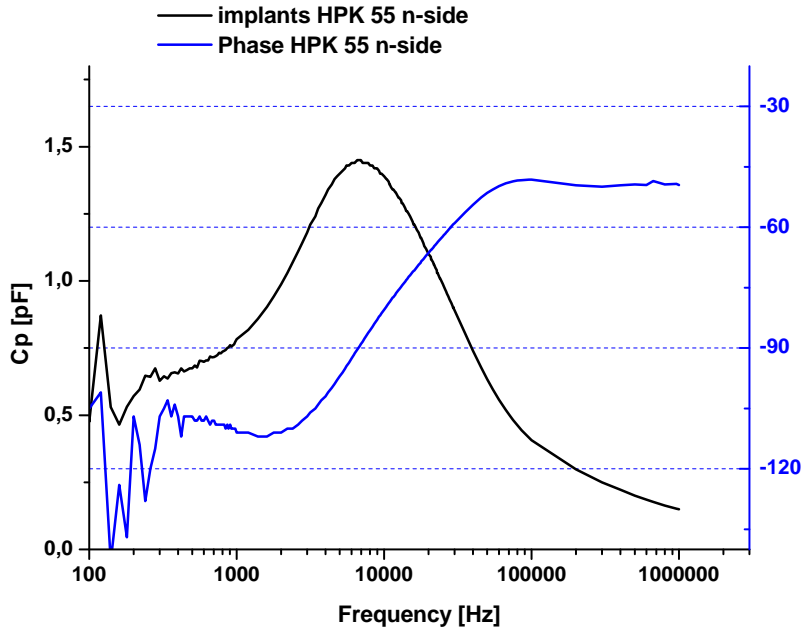


**Figure 7.4:** Frequency dependent interstrip capacitance of implants (black) and phase (blue) on a HPK sensor, n-side.

### Measurements on CMS test structure

Because of the inconsistencies found between single-sided CMS test structures and double-sided BELLE II sensors, more basic investigations are necessary before strip scans determining  $C_{int}$  systematically can be performed. Thus, the same type of measurements have been performed on totally different types of sensors. A CMS test structure was used to obtain reference results. Figures 7.5 and 7.6 show the interstrip capacitances between the implants and between the metal layers, respectively. The phases are plotted as well.

While the behavior of the capacitance between the metal layers is similar on these two different sensor types, the capacitance measurement between the implants yields different results. On the HPK sensor, a much stronger frequency dependence is obtained, concerning not only the capacitance but also the phase.

Additionally, both capacitances have been measured simultaneously. In figure 7.7 the different possibilities of contacting the probe needles for each measurement method is shown. The switching configuration of the matrix card remains the same for each measurement type. When four probe needles are used (green), they have to be switched together by a T-piece adapter. Hence, the high and low terminals of the Agilent 4284A LCR meter are connected to two probe needles each, measuring the sum of capacitances between the implants and the metal layers. "1"

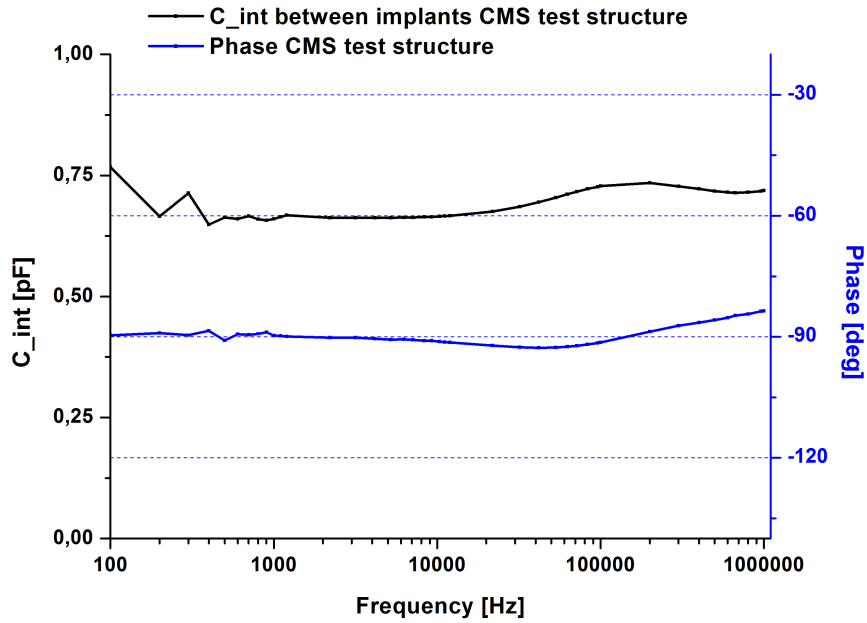


**Figure 7.5:** Frequency dependent interstrip capacitance between implants (black) and phase (blue) on a single sided CMS test structure.

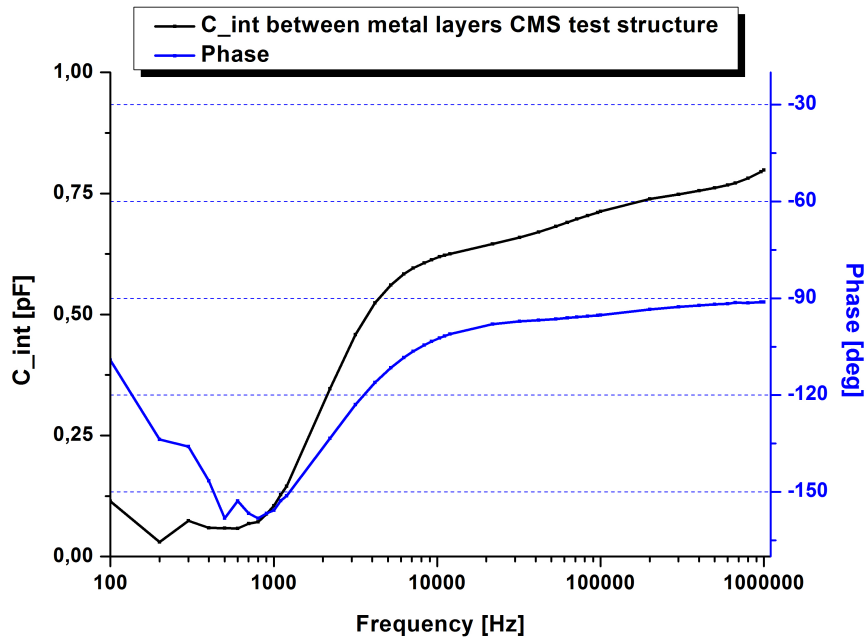


**Figure 7.6:** Frequency dependent interstrip capacitance between metal layers (black) and phase (blue) on a single sided CMS test structure.

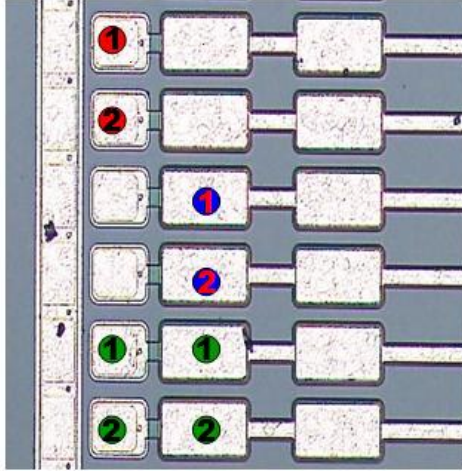


**Figure 7.7:** Possibilities of contacting the probe needles for interstrip capacitance measurement. red: implants only; blue: metal layers only; green: both implants and metal layers;

and "2" denote the low and high terminal of the LCR meter, respectively.

In figures 7.8 and 7.9 the results of all three measurements on a HPK BELLE II p-side and a CMS test structure are shown and compared to each other. Although, as discussed above, the capacitance between the implants and its corresponding phase indicate quite a different behavior on the HPK and the CMS sensor, there are also common features.

On both sensors, at low frequencies both the phase and the capacitance of the implants seems to be dominant. This is indicated by the red and the green lines, which are similarly shaped. At higher frequencies, the green lines seem to follow the behavior of the blue lines, which means that the contributions of the metal layers become dominant.

At low frequencies the capacitance between the metal layers on both sensors is quite low and the phase is clearly below  $-90^\circ$ . In each case at about 100 kHz the phase of the metal layers becomes  $-90^\circ$ , the capacitance saturates and the metal layers seem to become the dominant factor. On the Hamamatsu p-side this is even more explicit, because the red line indicating the capacitance decreases drastically. This is most likely explained by the strip length. At higher frequencies, the total length of the implant contributing to the measurement decreases. Thus, the capacitance is reduced [14]. The strip length of the HPK sensor used for this measurement is approximately 12 cm, while the strip length of the CMS test structure is only 1 cm. Hence, this effect is not seen in figure 7.9. Still, on the CMS structure, at high frequencies the capacitance between the metal layers seems to be dominant.

The behavior of the metal layers is outlined in figure 7.10. The plot shows the frequency dependent capacitances between the metal layers different sensor types. A high pass filter results from the low frequencies being shunted to ground [14] through the poly resistors.

### Measurements on DC coupled structures

All of the sensors were AC-coupled structures, see section 3.4.4, with the implants being grounded through a poly resistor connecting it to the bias line. This is the common configuration for BELLE II sensors. However, to obtain reference results, DC coupled structures were used to perform the same kind of measurements that have been discussed in the section above.

For this measurements a multi geometry sensor of Hamamatsu Photonics, designed by the SiLC collaboration was used. It consists of 256 strips, grouped into 16 zones. For each zone the strip

CHAPTER 7. INTERSTRIP CAPACITANCE

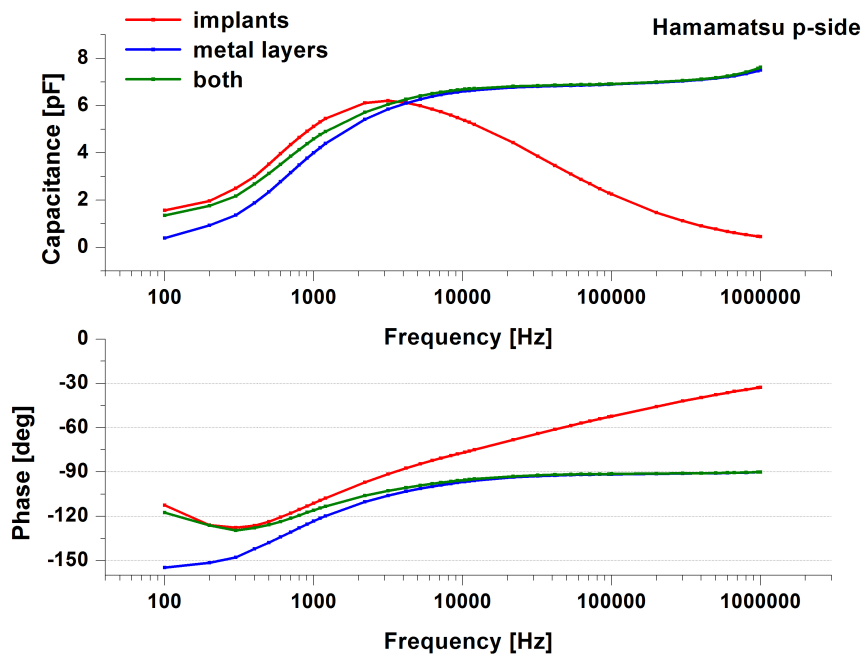


Figure 7.8: Capacitances and phases of 3 different measurement types according to figure 7.7 on a HPK p-side.

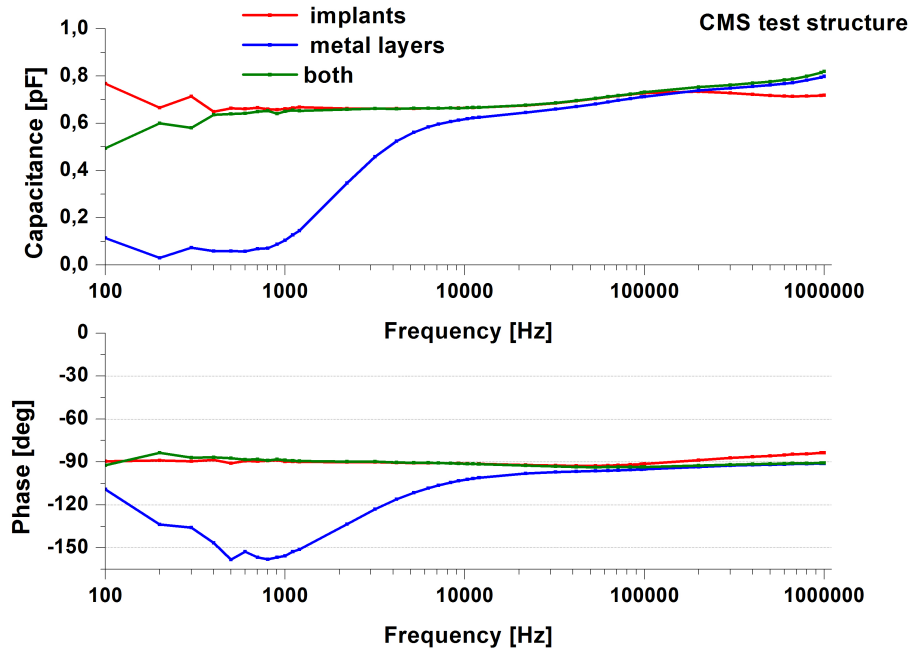
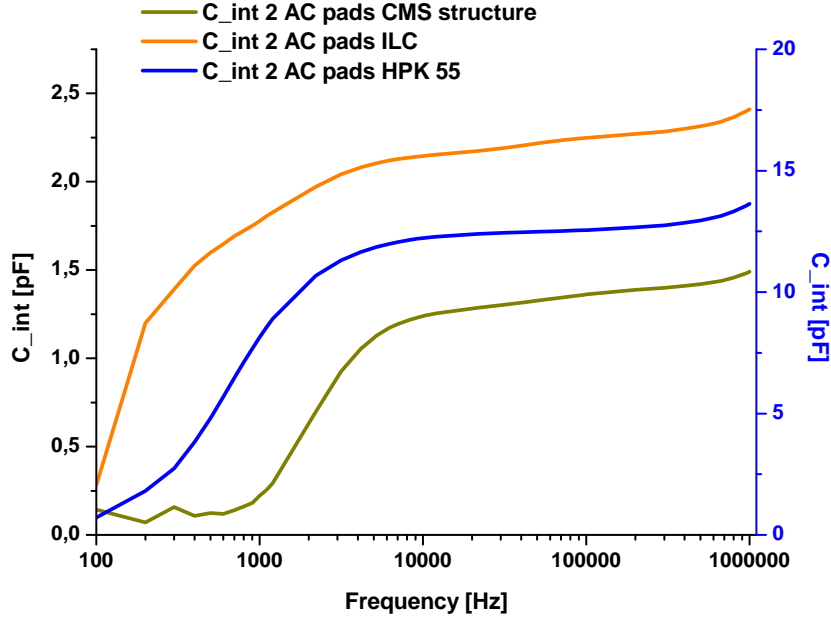


Figure 7.9: Capacitances and phases of 3 different measurement types according to figure 7.7 on a CMS test structure.



**Figure 7.10:** Frequency dependent interstrip capacitance between metal layers with different poly resistors. The blue line corresponds to the blue ordinate.

width and the number of intermediate strips vary, resulting in a different interstrip capacitance [15]. On a DC coupled structure, there is no oxide layer between the implant and the metal layer, nor a poly resistor. However, also an AC coupled version of this sensor was available and the results from frequency dependent interstrip capacitance measurements will be presented and compared in this section.

Figures 7.11 and 7.12 show the interstrip capacitances and corresponding phases on the DC coupled structure for different strip widths. In figures 7.13 and 7.14, the results on an AC coupled structure of the same type are shown. From figures 7.11 and 7.13 the influence of the strip width becomes obvious. The capacitance grows with increasing strip width. Furthermore, the results of the DC coupled structure are quite different than the results of the AC coupled structure. While the latter are similar to the results of the BELLE II HPK sensors in figures 7.2 and 7.4, the interstrip capacitance looks different on the DC coupled structures. There is no peak and the phase remains constant at  $-90^\circ$  over a large frequency interval. The fact that the interstrip capacitance on the DC couples structure remains constant also at high frequencies can be understood by the absence of the oxide layer between the implant and the metal layer. Since the metal layer has a very low resistivity, the whole length of the implant can still contribute to the capacitance at high frequencies.

The measurements of plots 7.11 to 7.14 all have been performed by contacting the implants via the DC pads, according to figure 7.7. A comparison of AC and DC coupled structures when AC contacted is given in figure 7.15. Again, on the DC coupled structure the results differ from the results on the DC coupled structure. Phase and capacitance on the AC coupled device look similar to the behavior of the BELLE II sensors. The DC coupled structure features none of the effects seen on AC coupled sensors. These findings suggest that the behavior observed on the BELLE II sensors (and on the AC coupled ILC structure) result from an interplay of the poly resistor, the coupling capacitance and the interstrip capacitance.



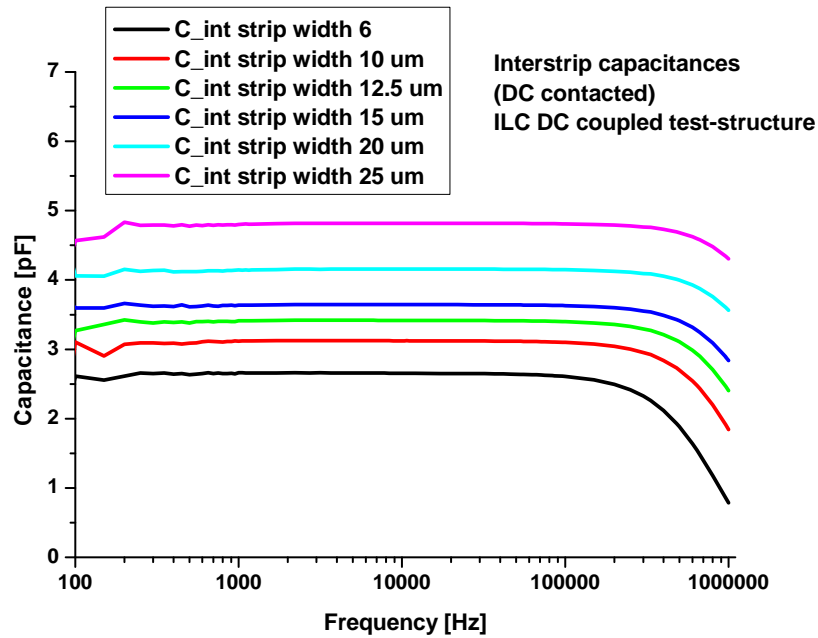


Figure 7.11: Interstrip capacitances (DC contacted) on a DC coupled ILC structure for different strip widths.

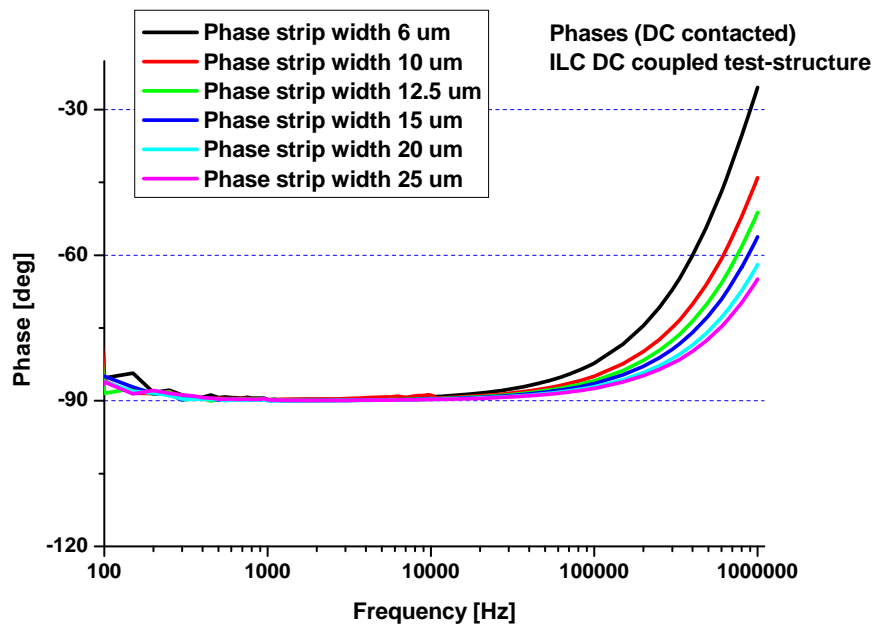
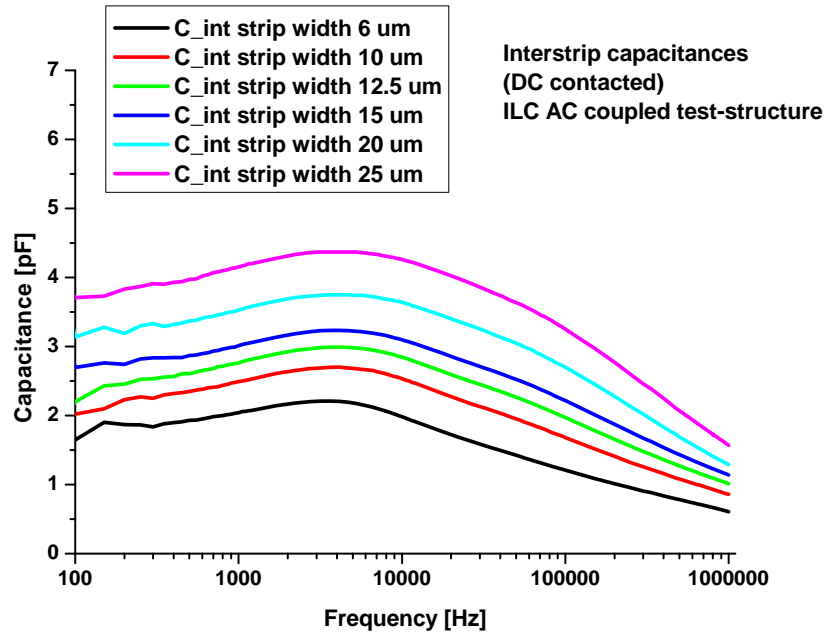
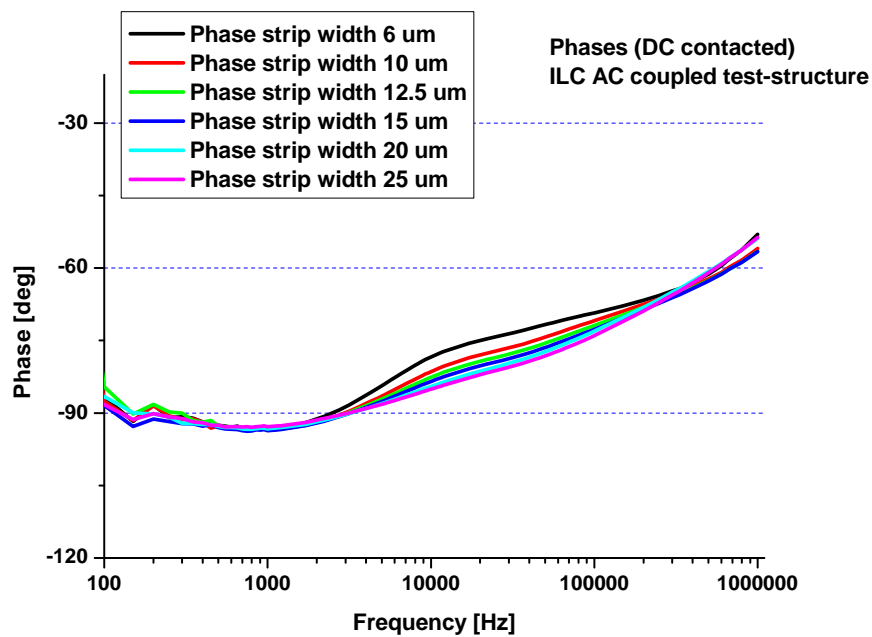


Figure 7.12: Phases (DC contacted) on a DC coupled ILC structure for different strip widths.



**Figure 7.13:** Interstrip capacitances (DC contacted) on an AC coupled ILC structure for different strip widths.



**Figure 7.14:** Phases (DC contacted) on an AC coupled ILC structure for different strip widths.

CHAPTER 7. INTERSTRIP CAPACITANCE

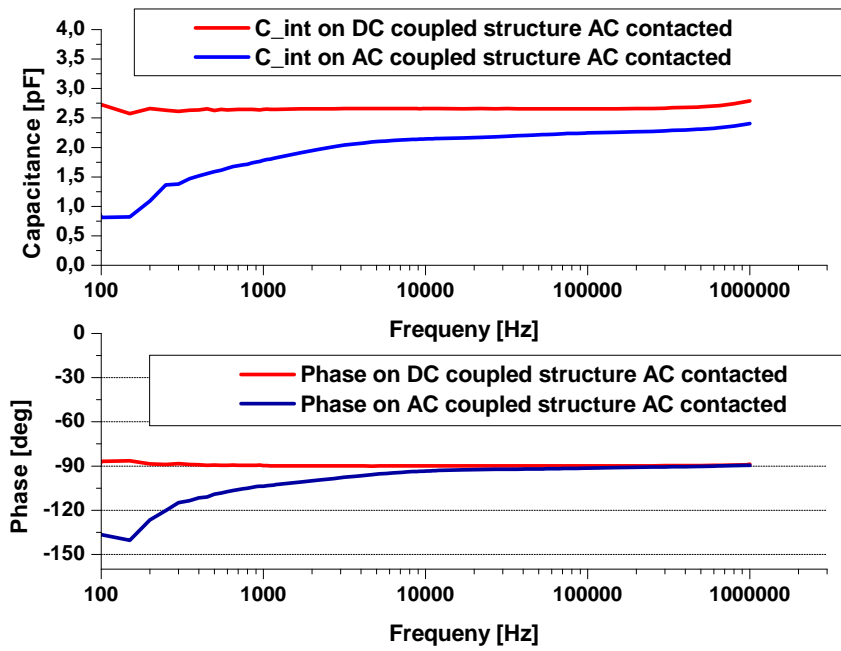


**Figure 7.15:** Interstrip capacitances (top) and phases (bottom) of AC contacted measurements on a DC coupled (red) and an AC coupled structure (blue).

At this point, simulations of the whole network, eventually taking into consideration neighboring strips, are demanded for further understanding.

## 7.2. MEASUREMENTS

## Chapter 8

# Summary and Outlook

In this thesis, the interstrip parameters of silicon sensors designed for the BELLE II Silicon Vertex Detector have been investigated. For this purpose, the Quality Test Center (QTC) at the HEPHY Vienna has been used. The task was also to develop new measurement routines, designed specifically to be introduced to the already existing measurement setup and include interstrip measurement methods into the standard quality assurance scheme of the QTC Vienna. Interstrip parameters of interest for quality assurance are the intersrip resistance and the interstrip capacitance.

Mainly double sided silicon sensors from two vendors (Hamamatsu and Micron) have been measured, but also a few single sided test structures. The majority of the measurements performed were interstrip resistance measurements. The reason for this is that it was difficult to obtain reproducible results due to sensor related effects. Consequently, these effects have been investigated and classified. Furthermore, measurement routines have been developed that take into account sensor related effects that disrupt the interstrip resistance measurement. The aim was to create a measurement method that doesn't slow down the overall quality assurance process too much. Since sensor effects cause the measurement to slow down, a compromise has to be made between accuracy and speed. All in all 3 measurement methods have been developed.

For measuring the interstrip capacitance, frequency dependent capacitance measurements have been performed. The main result was that the interstrip capacitance depends on the measurement frequency to a high degree. A future measurement method that yet has to be developed must take into account for that. The results have been cross checked with an already existing paper[14].

Concerning the interstrip resistance as well as the interstrip capacitance measurements, some results are not conclusive yet and may cannot be understood by measurements only. Mainly they are time dependent behavior of currents during the interstrip resistance measurement and the low frequency behavior of the interstrip capacitance. At the current progress of investigation, a more theoretical approach including simulations is recommended for better understanding of these effects.



## Appendix A

# Stripscans of section 5

### A.1 Hamamatsu 2nd batch

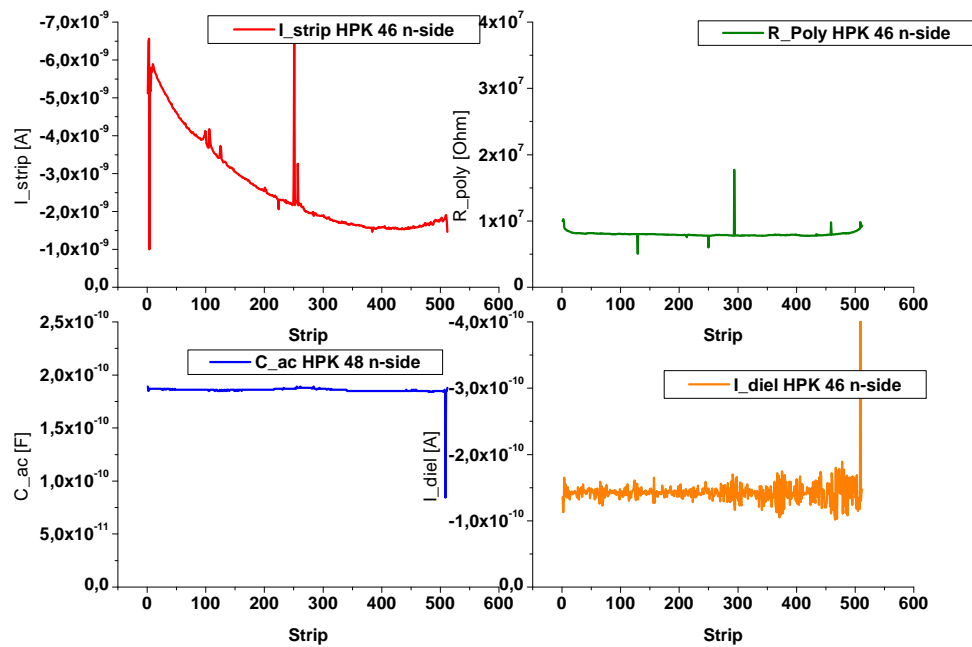


Figure A.1: Stripscan of HPK 46 n-side

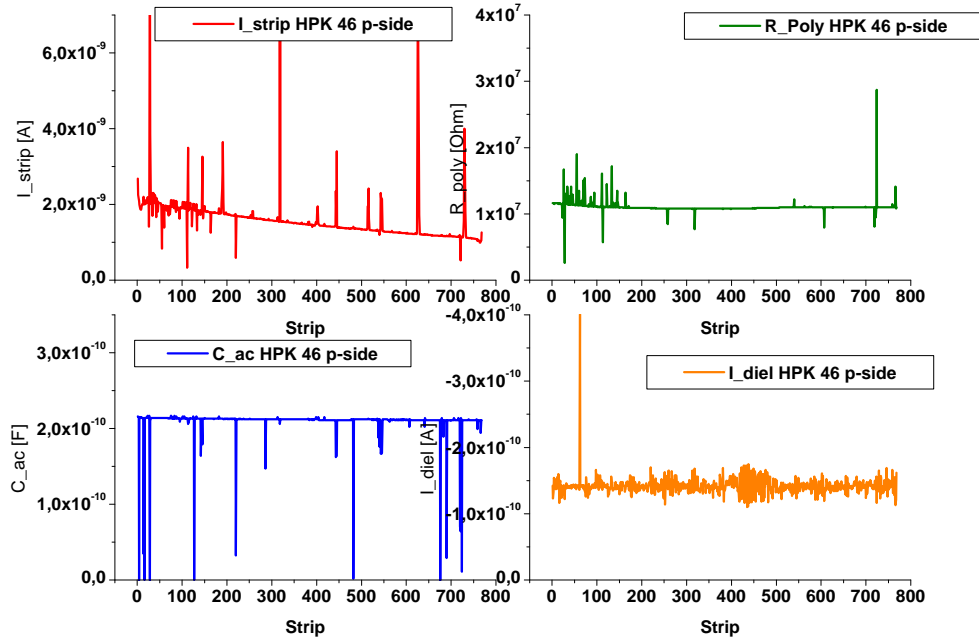


Figure A.2: Strips can of HPK 46 p-side

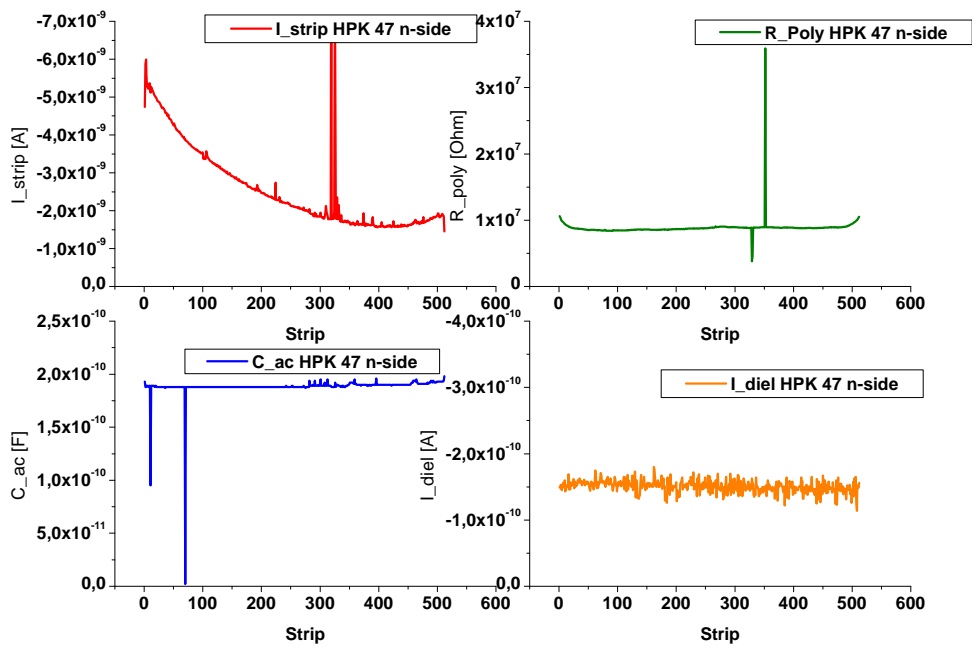


Figure A.3: Strips can of HPK 47 n-side



APPENDIX A. STRIPSCANS OF SECTION ??

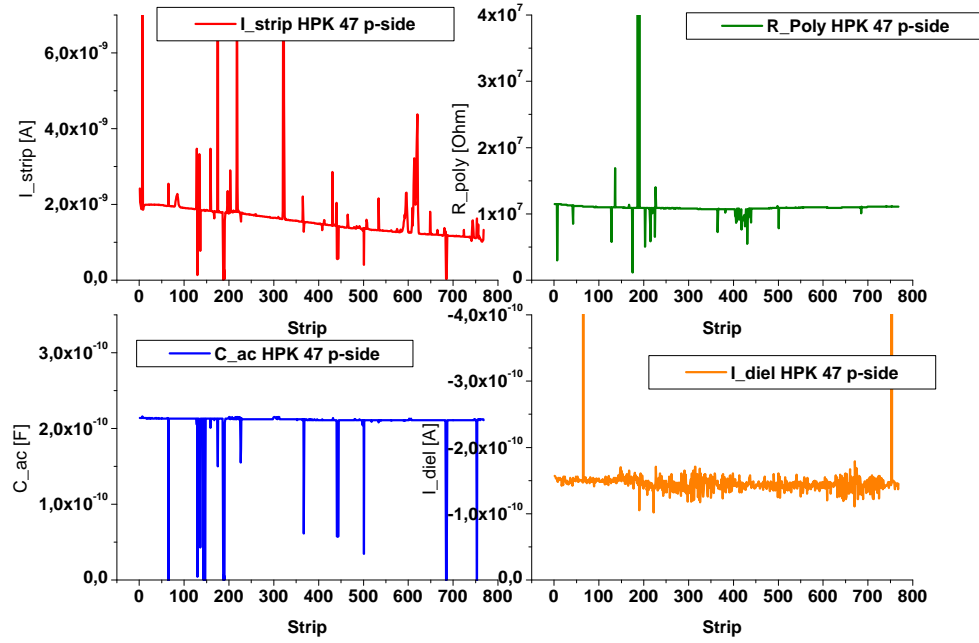


Figure A.4: Stripscan of HPK 47 p-side

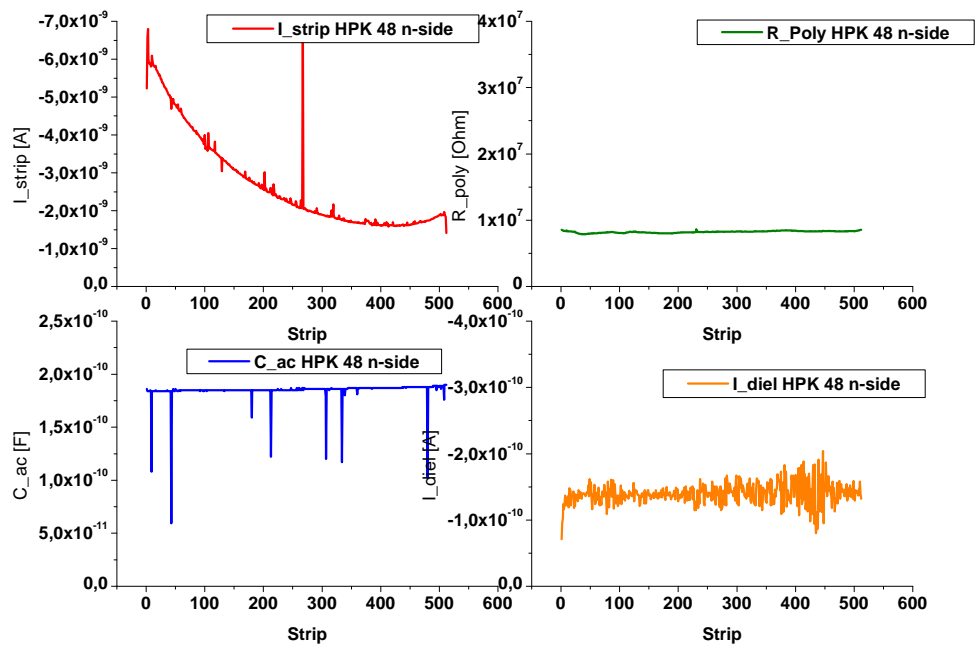


Figure A.5: Stripscan of HPK 48 n-side

A.1. HAMAMATSU 2ND BATCH

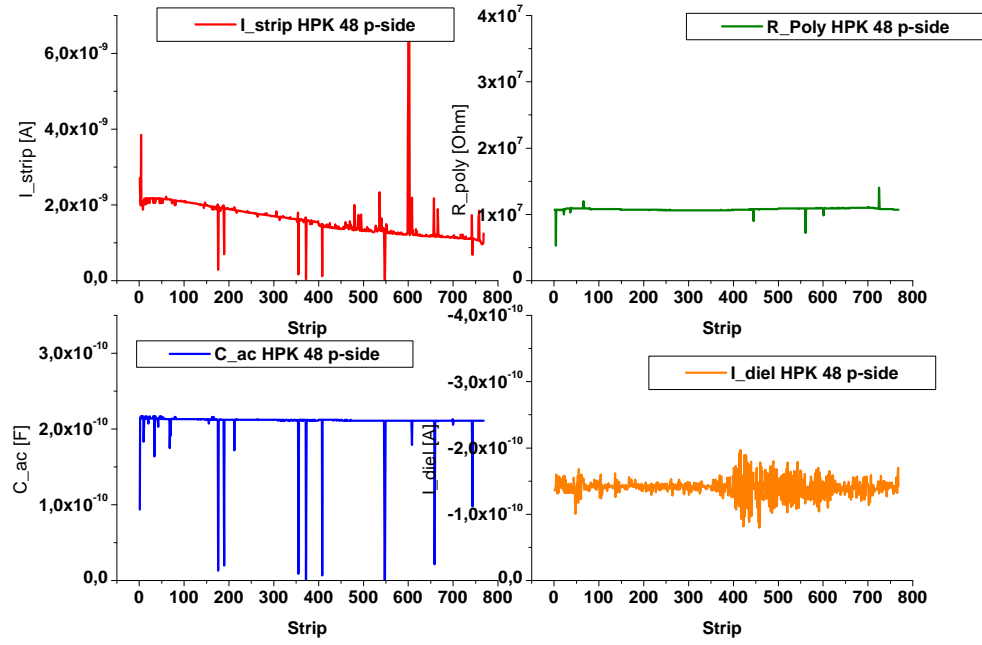


Figure A.6: Stripscan of HPK 48 p-side

## A.2 Micron 1st batch

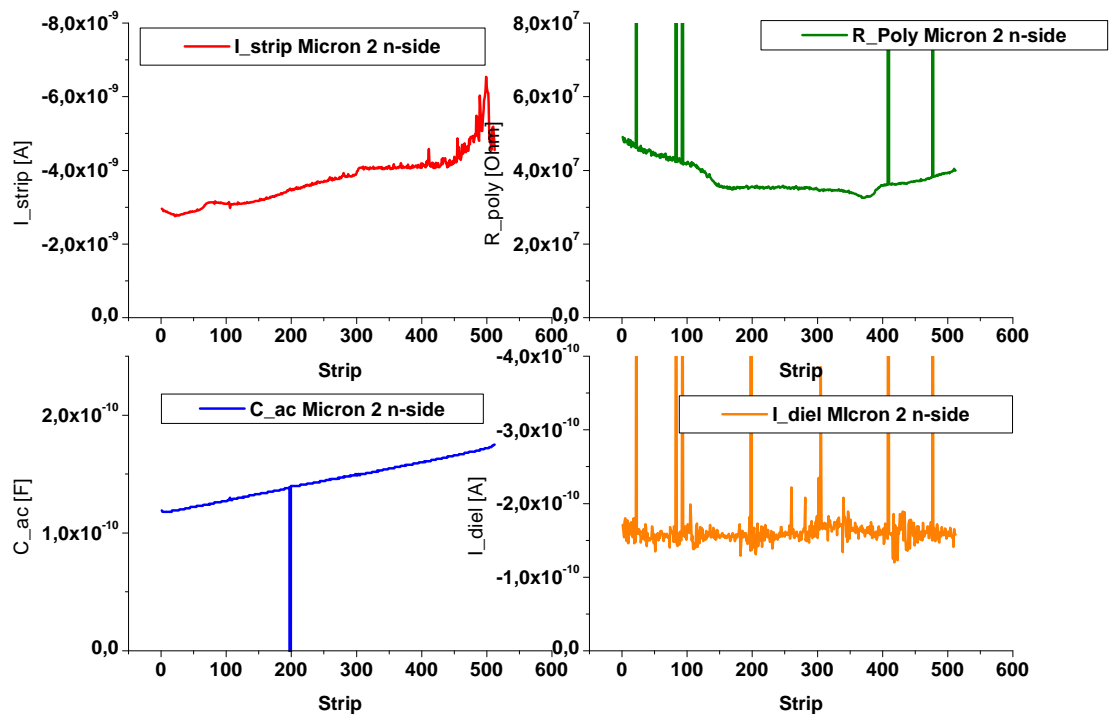


Figure A.7: Stripscan of Micron 2 n-side

A.2. MICRON 1ST BATCH

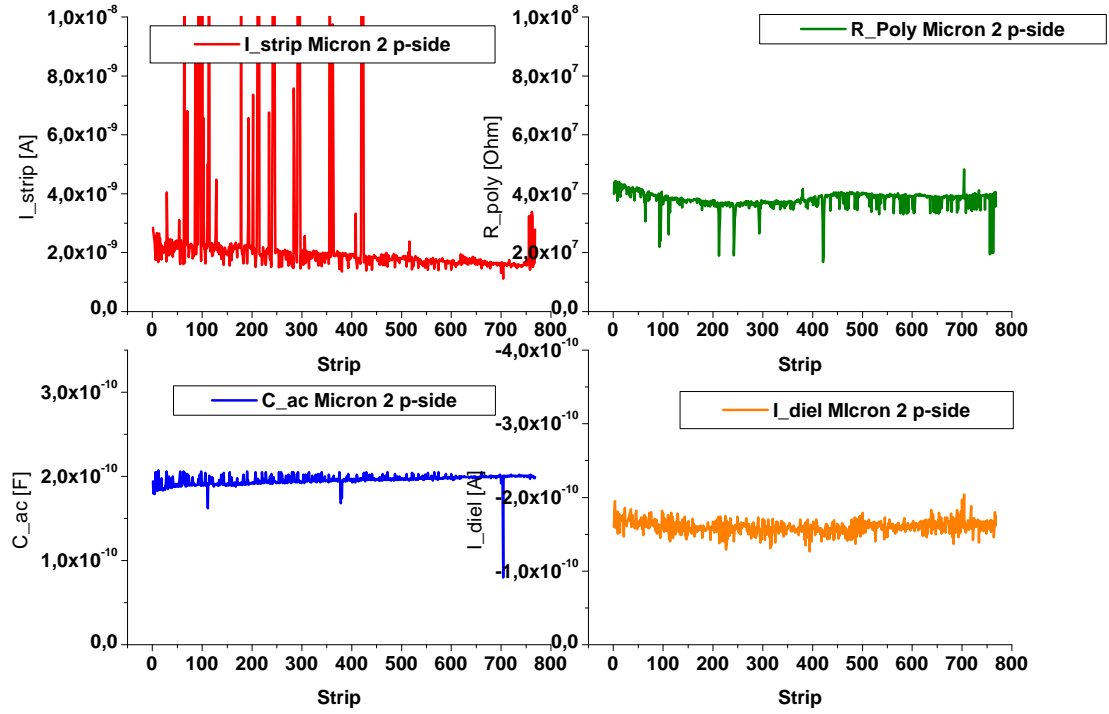


Figure A.8: Stripsan of Micron 2 p-side

APPENDIX A. STRIPSCANS OF SECTION ??

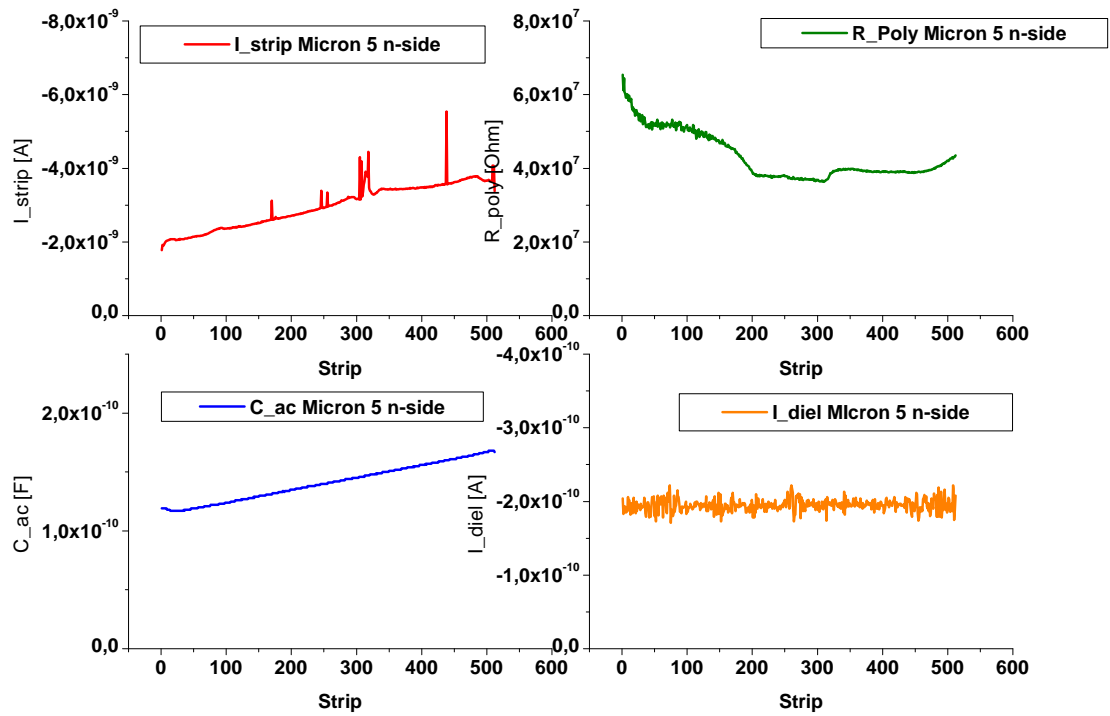


Figure A.9: Stripskan of Micron 5 n-side

A.2. MICRON 1ST BATCH

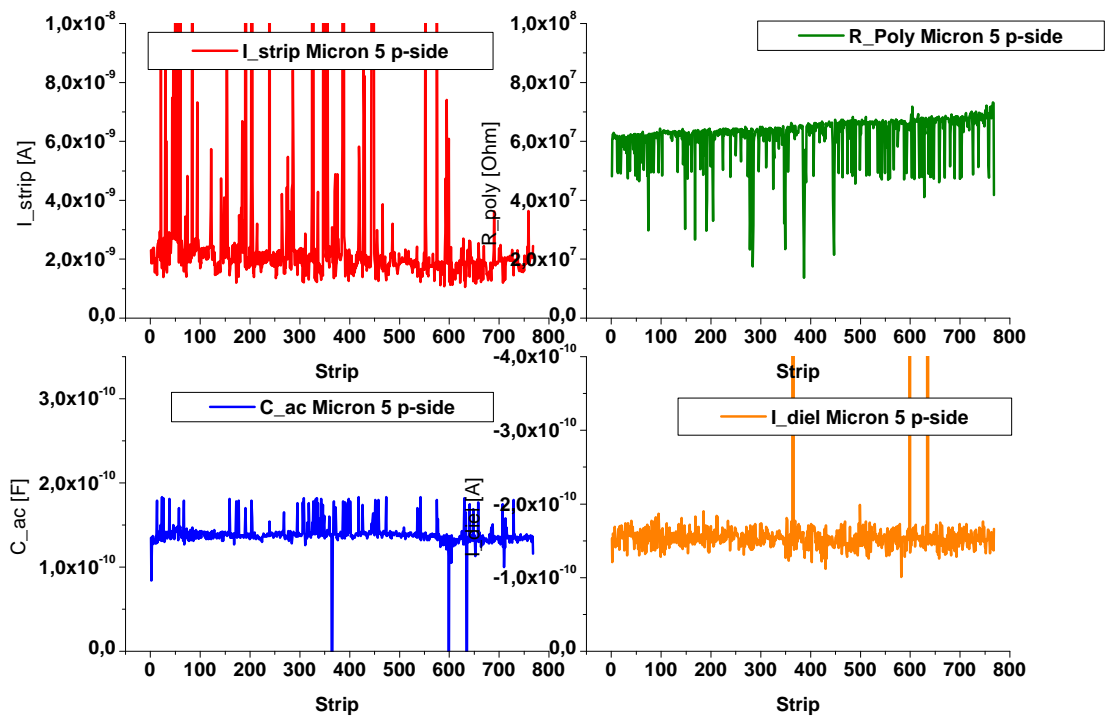


Figure A.10: Stripsan of Micron 5 p-side

APPENDIX A. STRIPSCANS OF SECTION ??

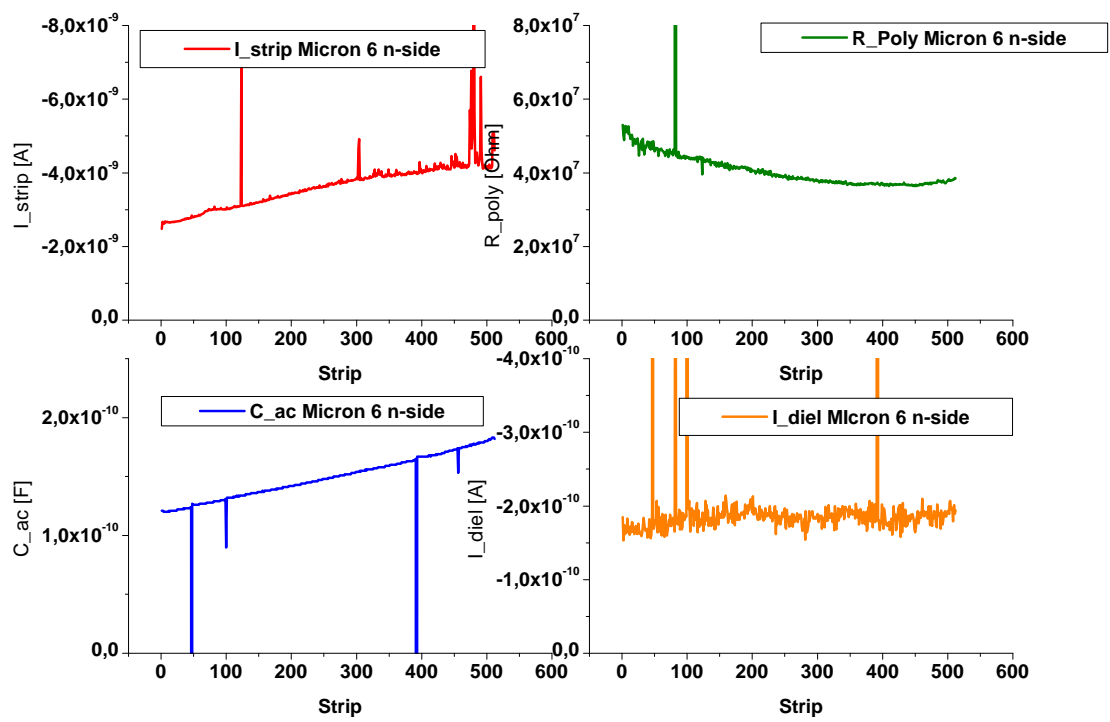


Figure A.11: Stripscan of Micron 6 n-side

A.2. MICRON 1ST BATCH

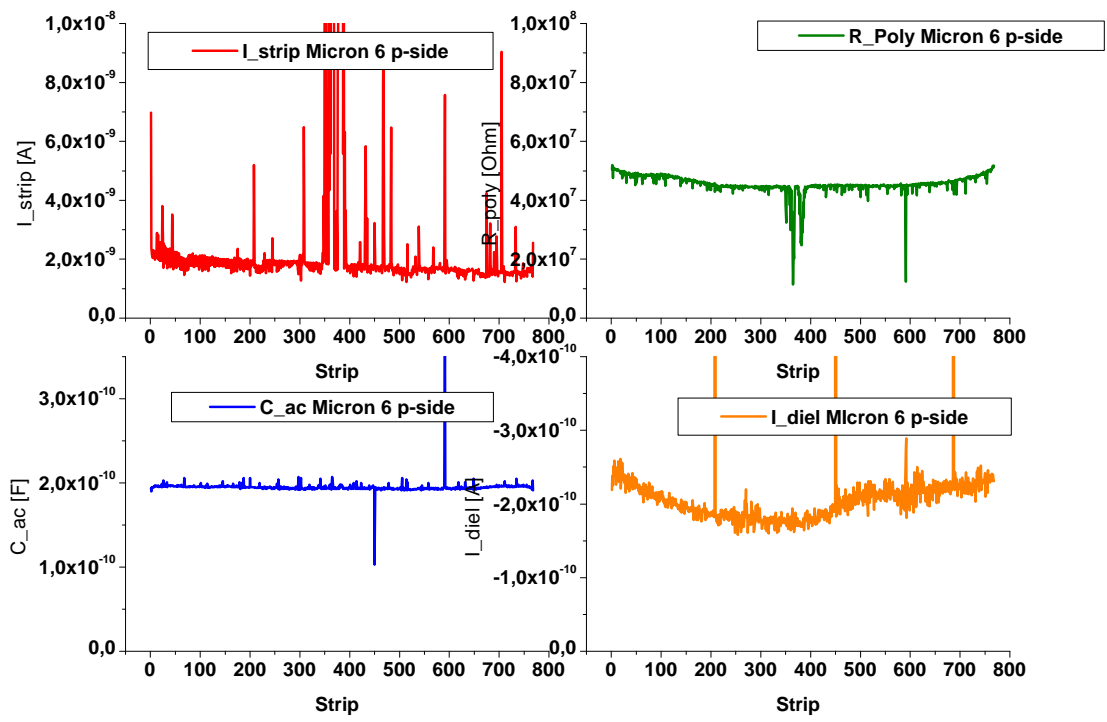


Figure A.12: Strips-scan of Micron 6 p-side



APPENDIX A. STRIPSCANS OF SECTION ??

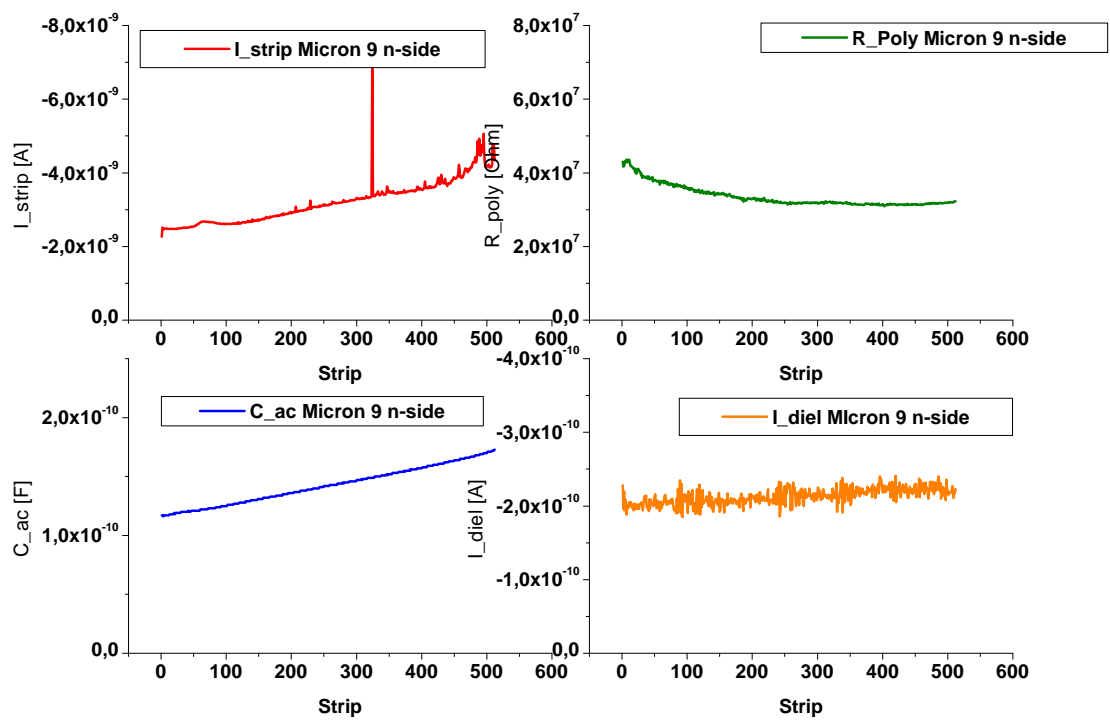


Figure A.13: Stripscan of Micron 9 n-side

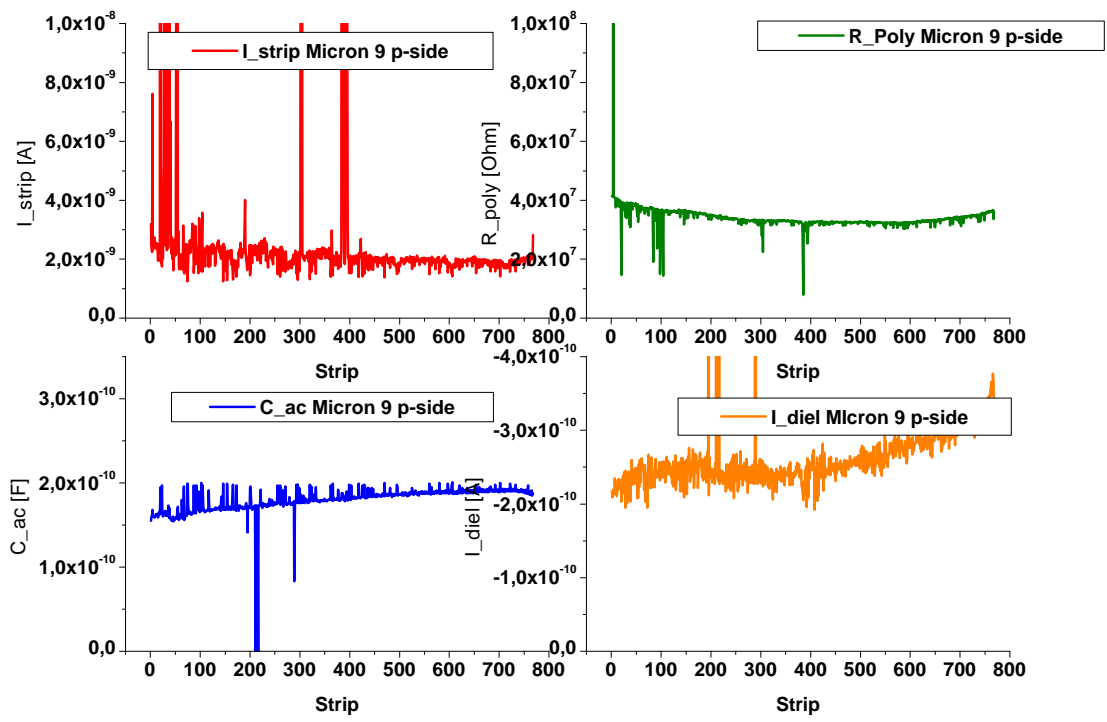


Figure A.14: Stripscan of Micron 9 p-side

APPENDIX A. STRIPSCANS OF SECTION ??

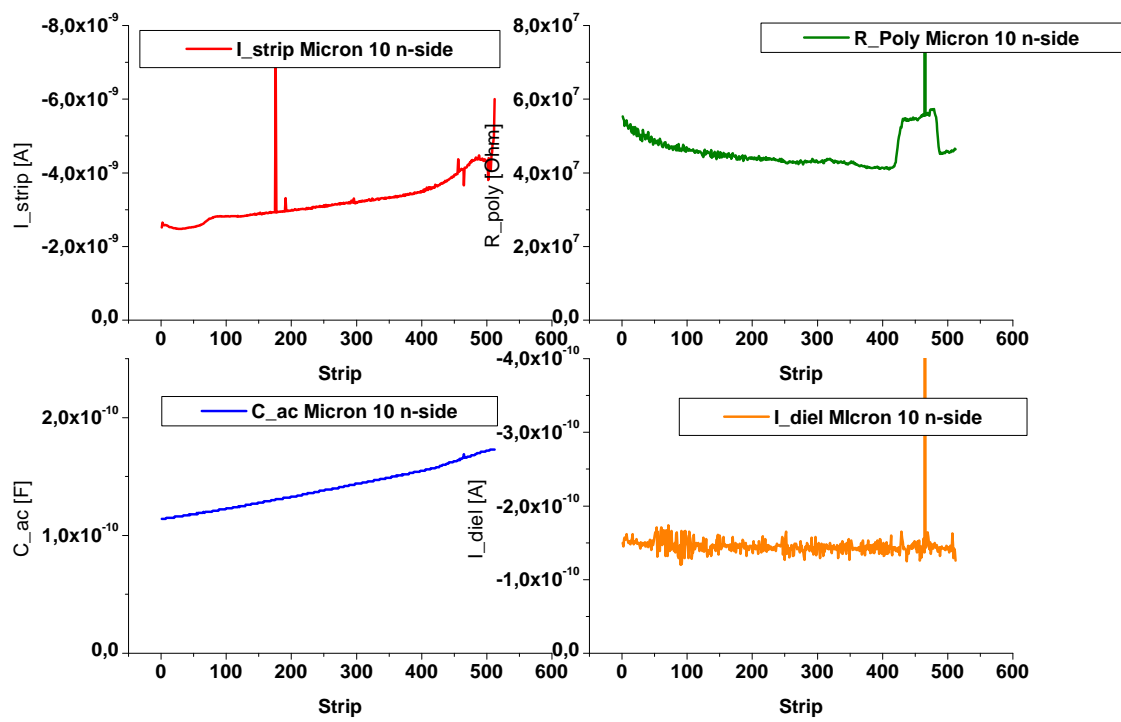


Figure A.15: Stripscan of Micron 10 n-side

A.2. MICRON 1ST BATCH

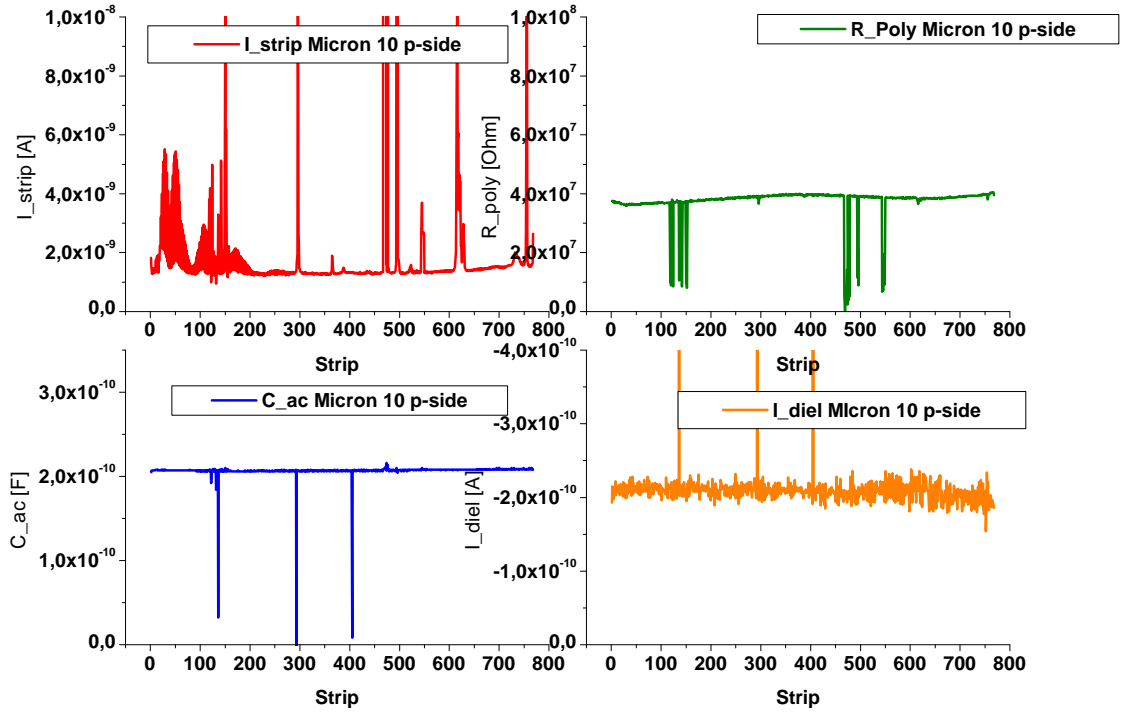


Figure A.16: Stripsan of Micron 10 p-side

APPENDIX A. STRIPSCANS OF SECTION ??

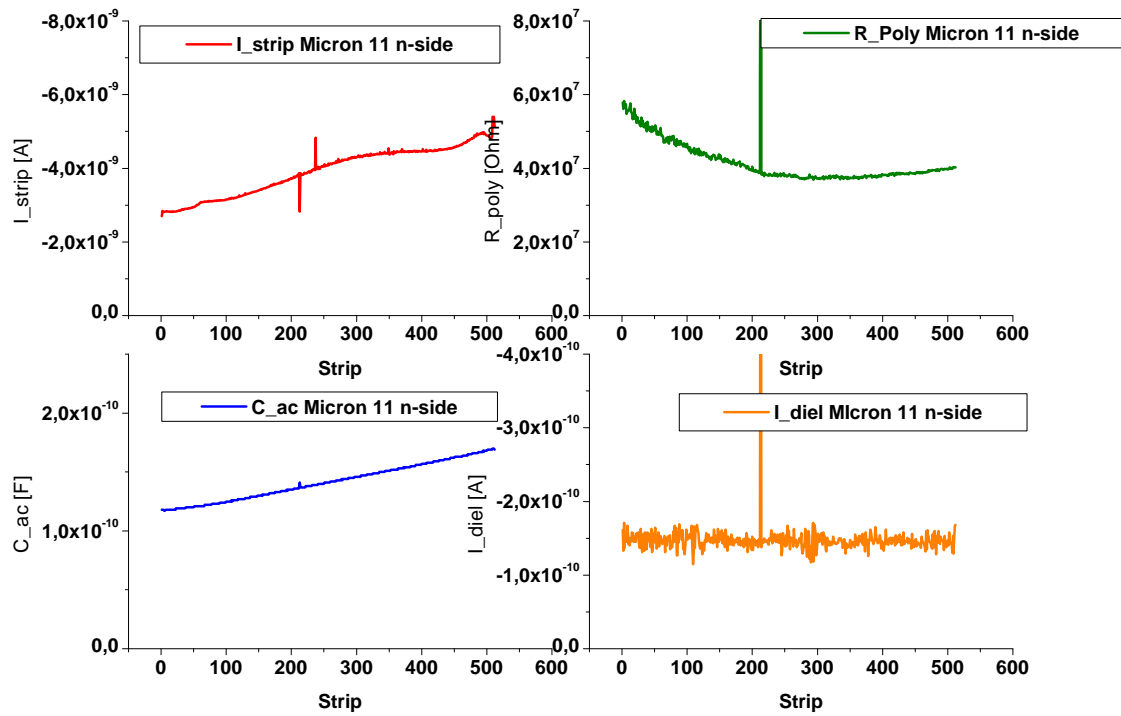


Figure A.17: Stripsan of Micron 11 n-side

A.2. MICRON 1ST BATCH

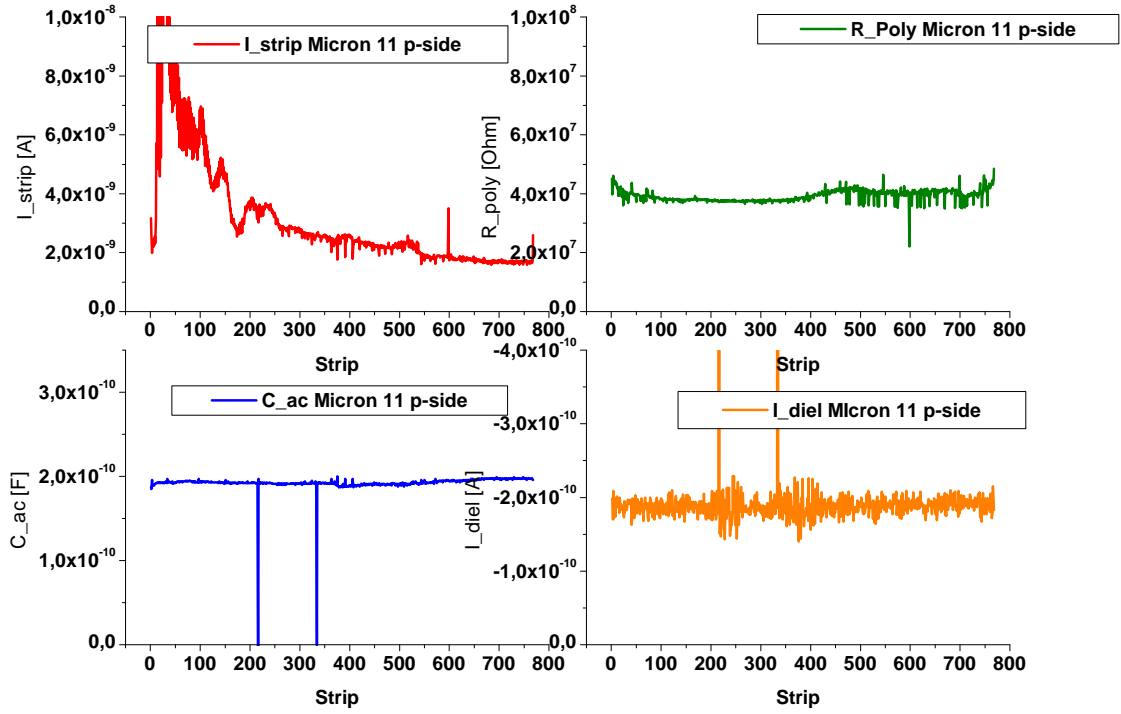


Figure A.18: Stripsan of Micron 11 p-side

APPENDIX A. STRIPSCANS OF SECTION ??

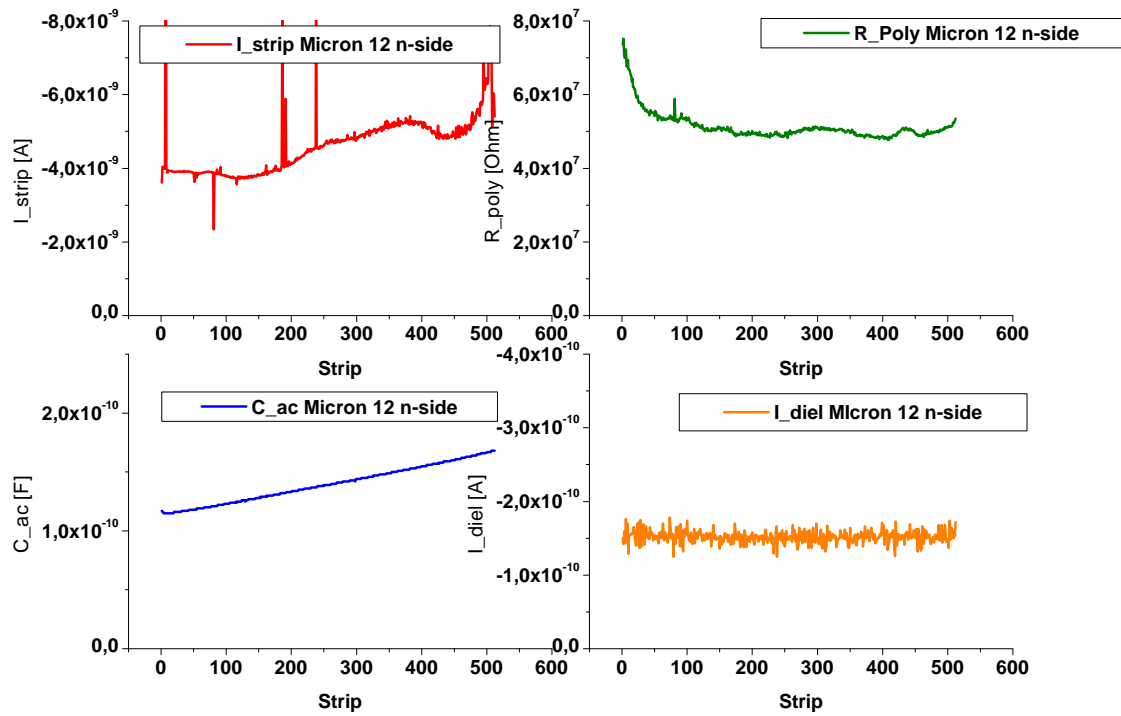


Figure A.19: Stripscan of Micron 12 n-side

A.2. MICRON 1ST BATCH

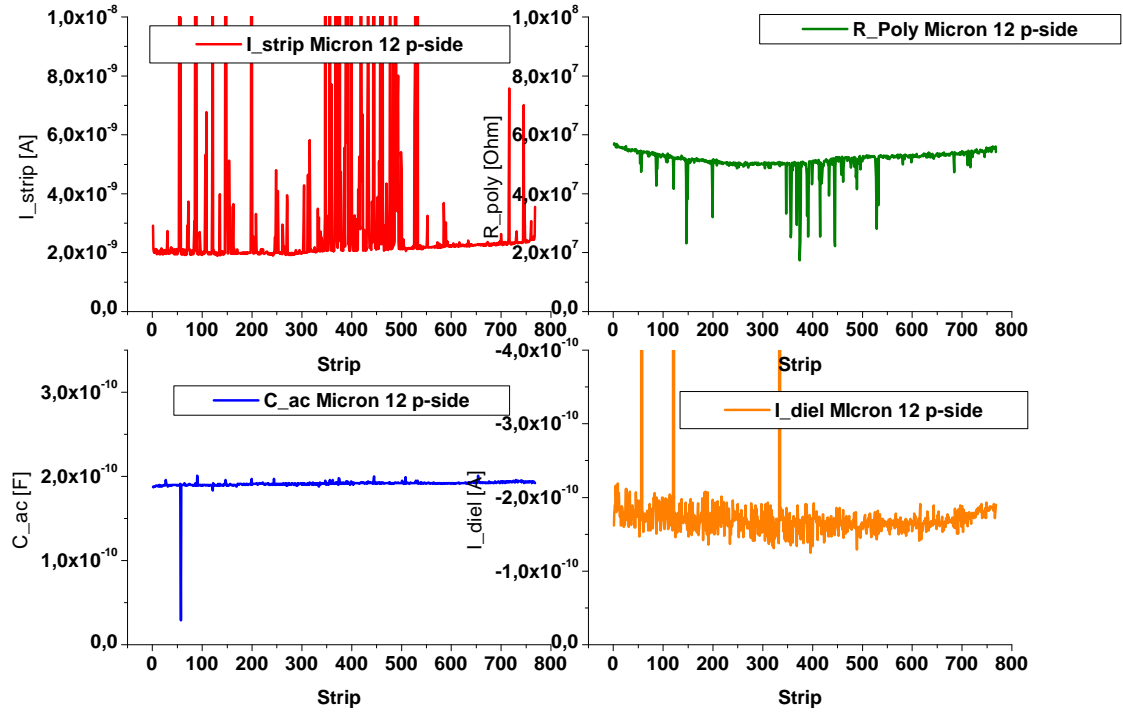


Figure A.20: Stripsan of Micron 12 p-side



APPENDIX A. STRIPSCANS OF SECTION ??

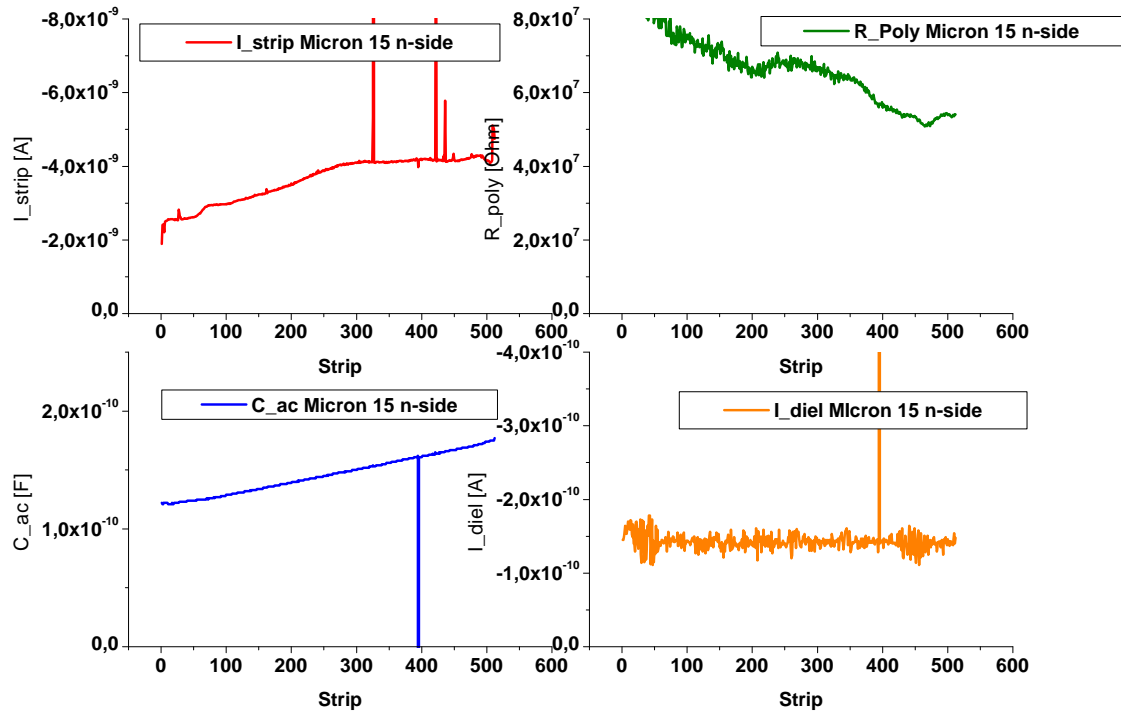


Figure A.21: Stripsan of Micron 15 n-side

A.2. MICRON 1ST BATCH

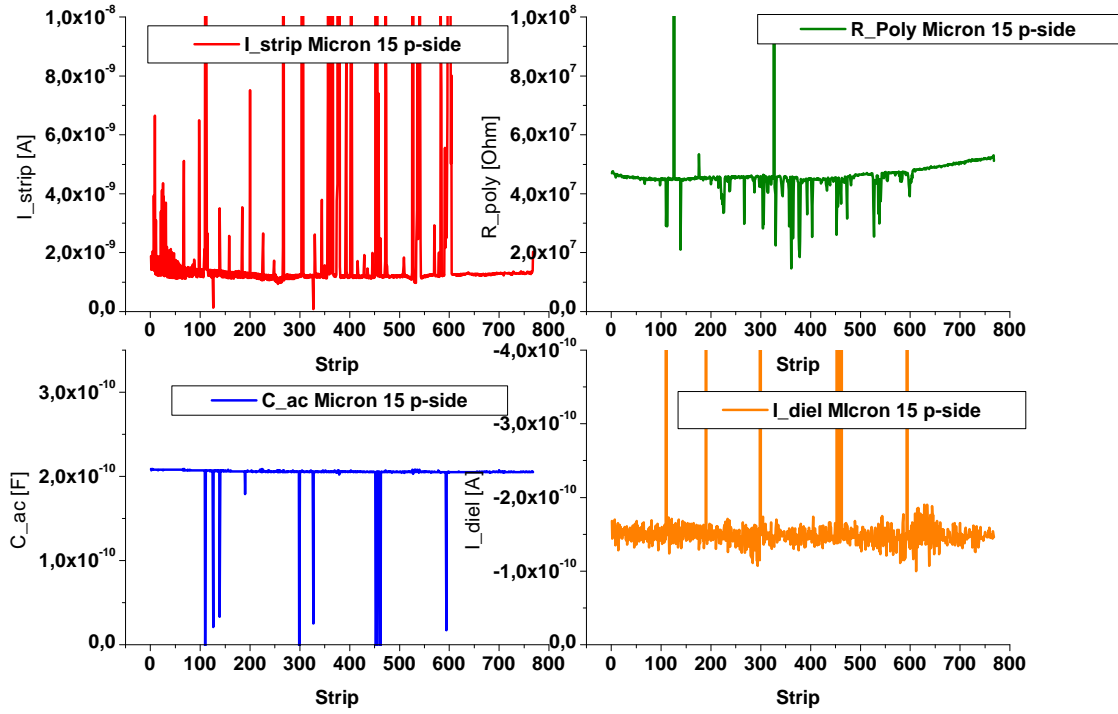


Figure A.22: Stripsan of Micron 15 p-side

APPENDIX A. STRIPSCANS OF SECTION ??

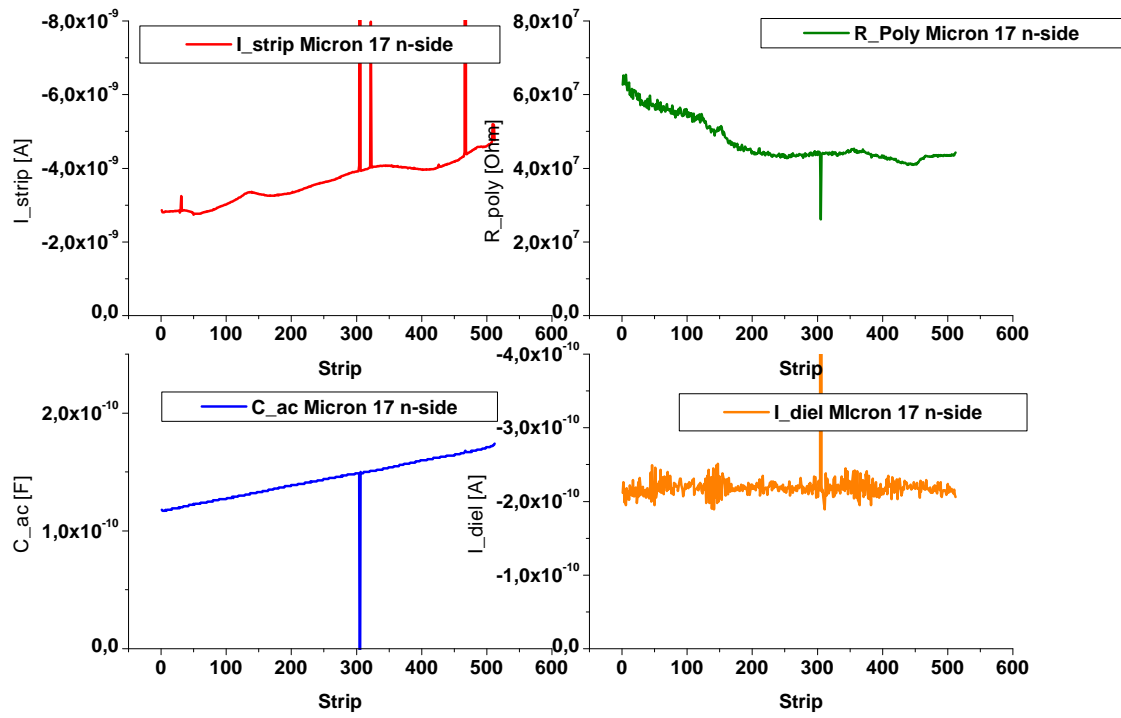


Figure A.23: Stripsan of Micron 17 n-side

A.2. MICRON 1ST BATCH

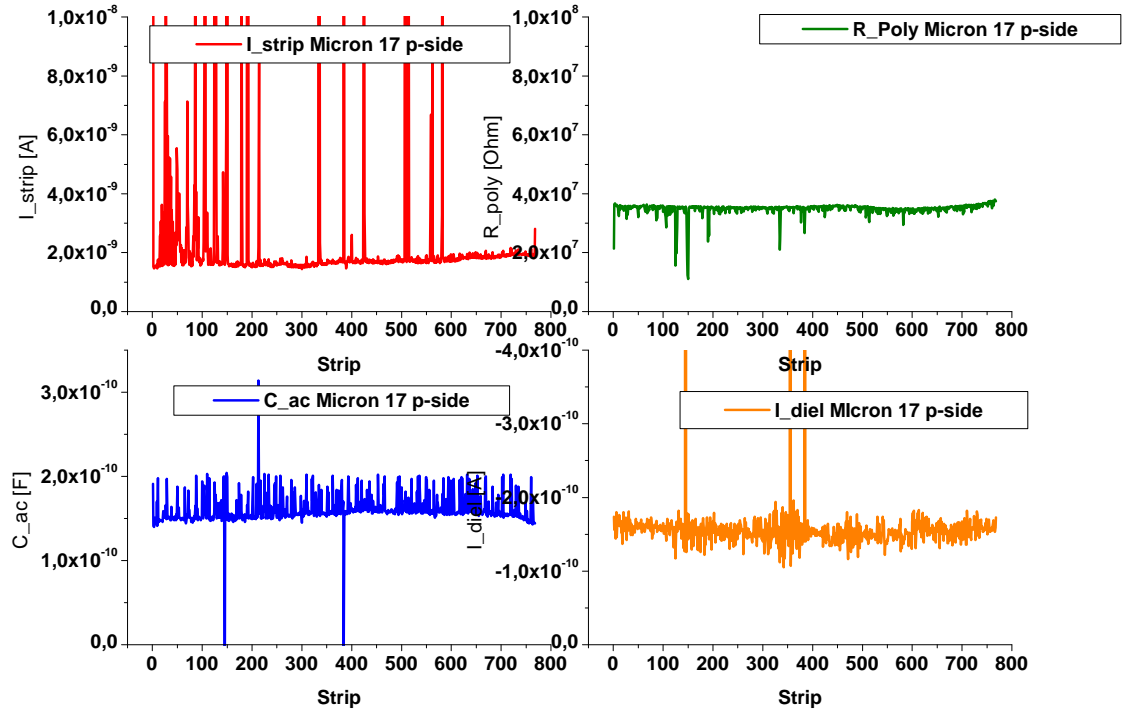


Figure A.24: Stripsan of Micron 17 p-side

APPENDIX A. STRIPSCANS OF SECTION ??

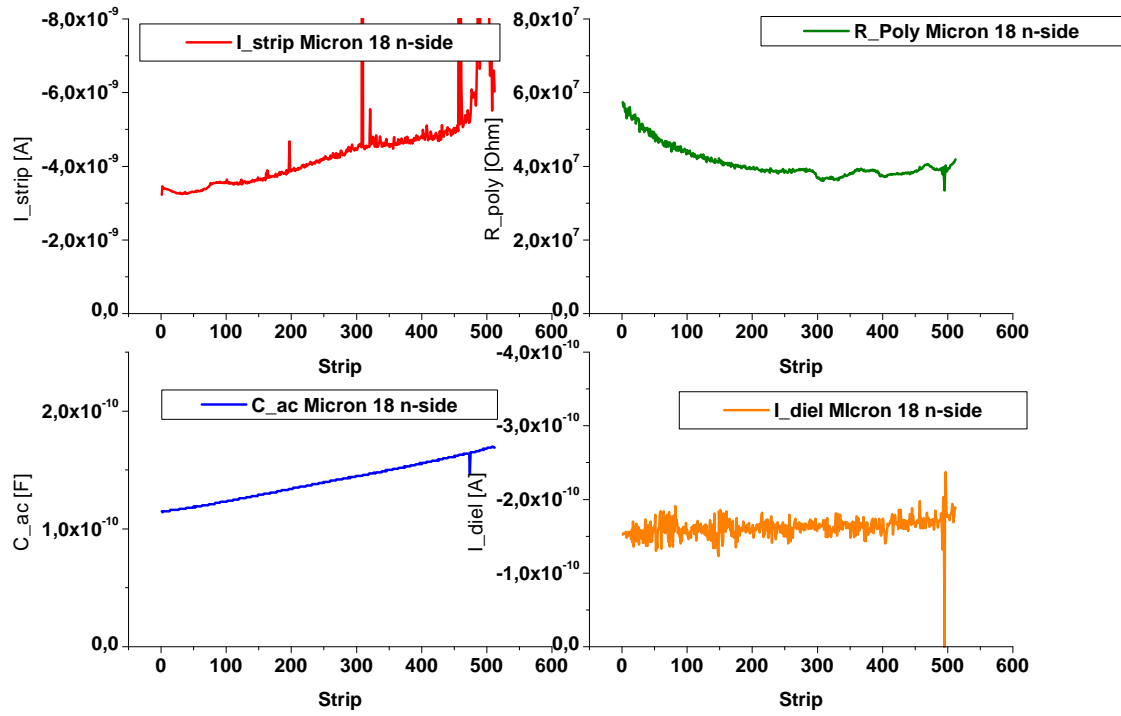


Figure A.25: Stripsan of Micron 18 n-side

A.2. MICRON 1ST BATCH

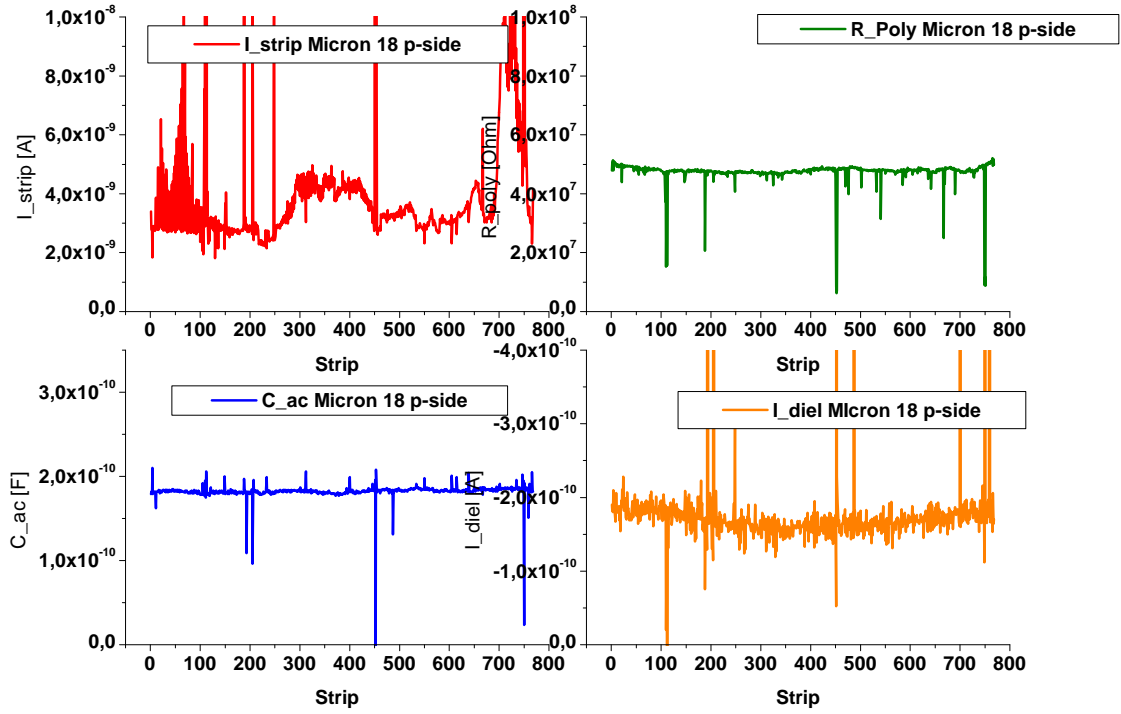


Figure A.26: Stripsan of Micron 18 p-side

APPENDIX A. STRIPSCANS OF SECTION ??

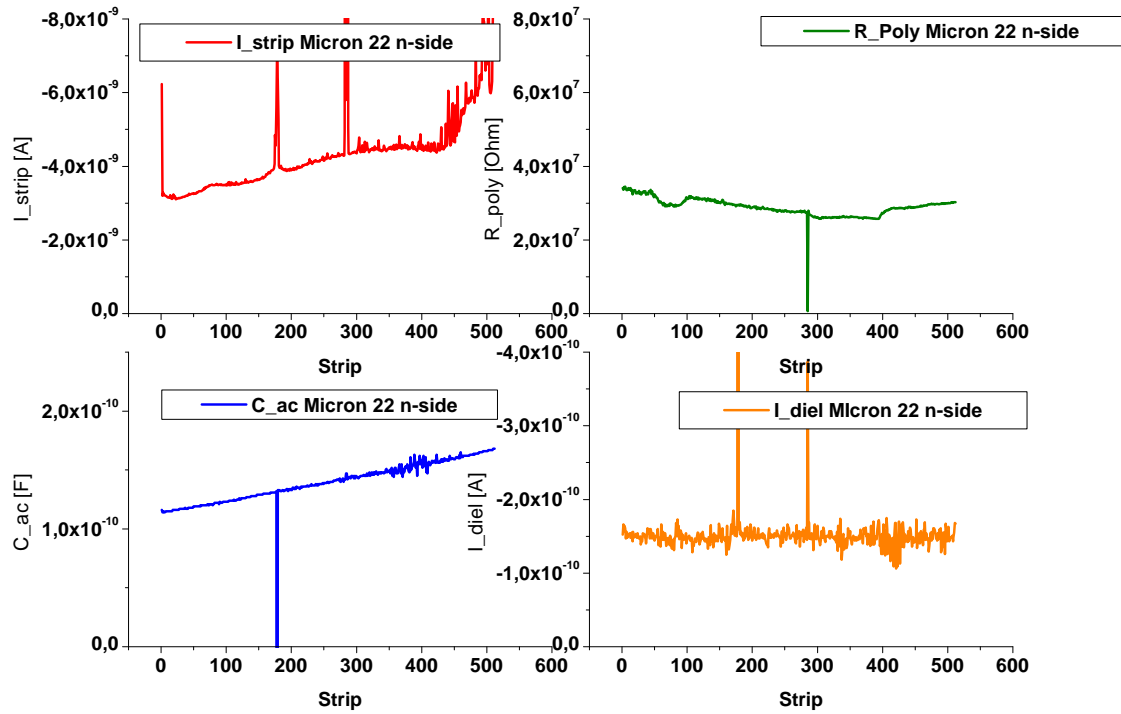


Figure A.27: Stripscan of Micron 22 n-side

A.2. MICRON 1ST BATCH

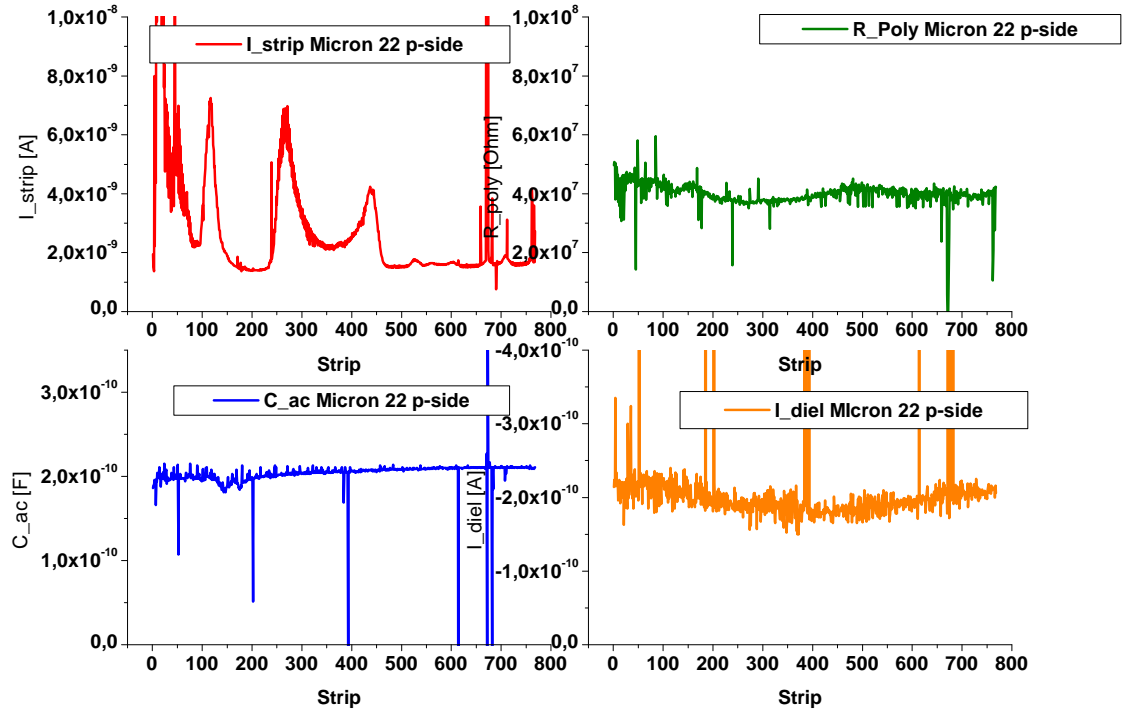


Figure A.28: Stripsan of Micron 22 p-side



APPENDIX A. STRIPSCANS OF SECTION ??

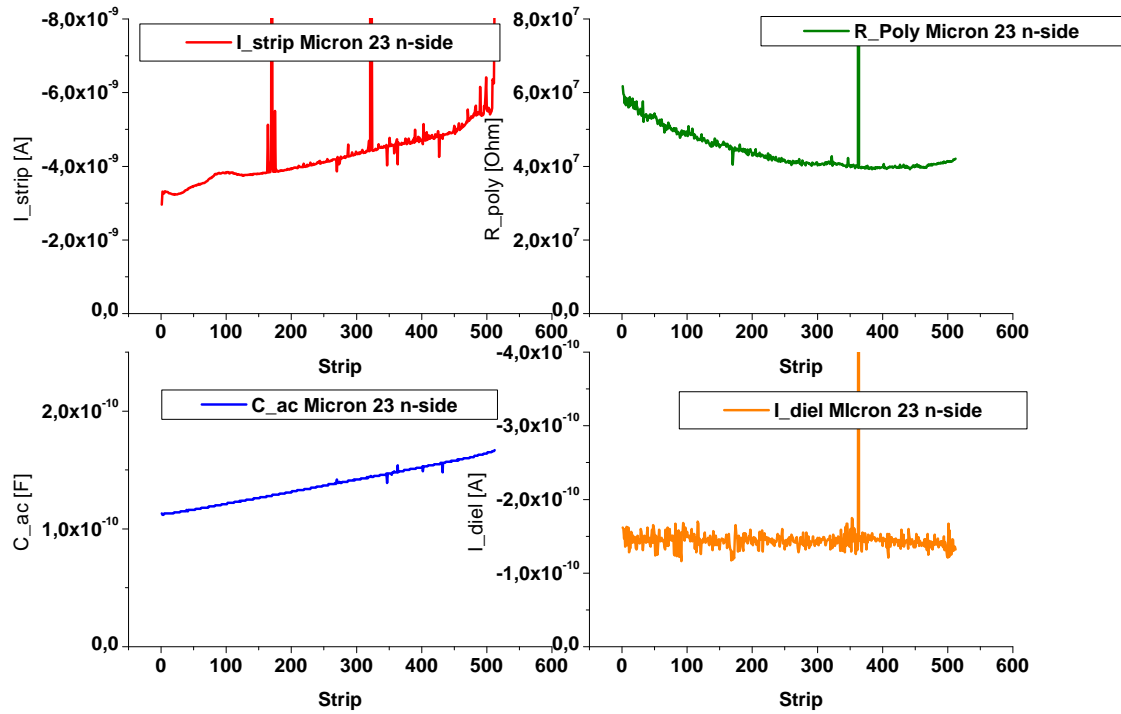


Figure A.29: Stripsan of Micron 23 n-side

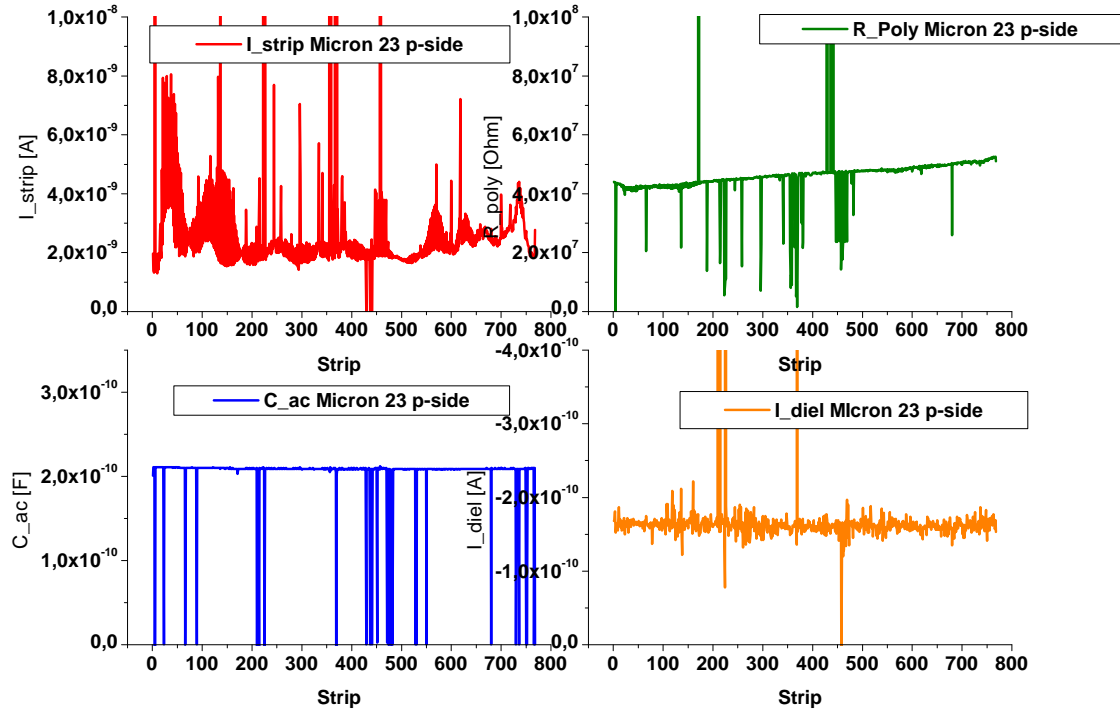


Figure A.30: Stripsan of Micron 23 p-side

APPENDIX A. STRIPSCANS OF SECTION ??

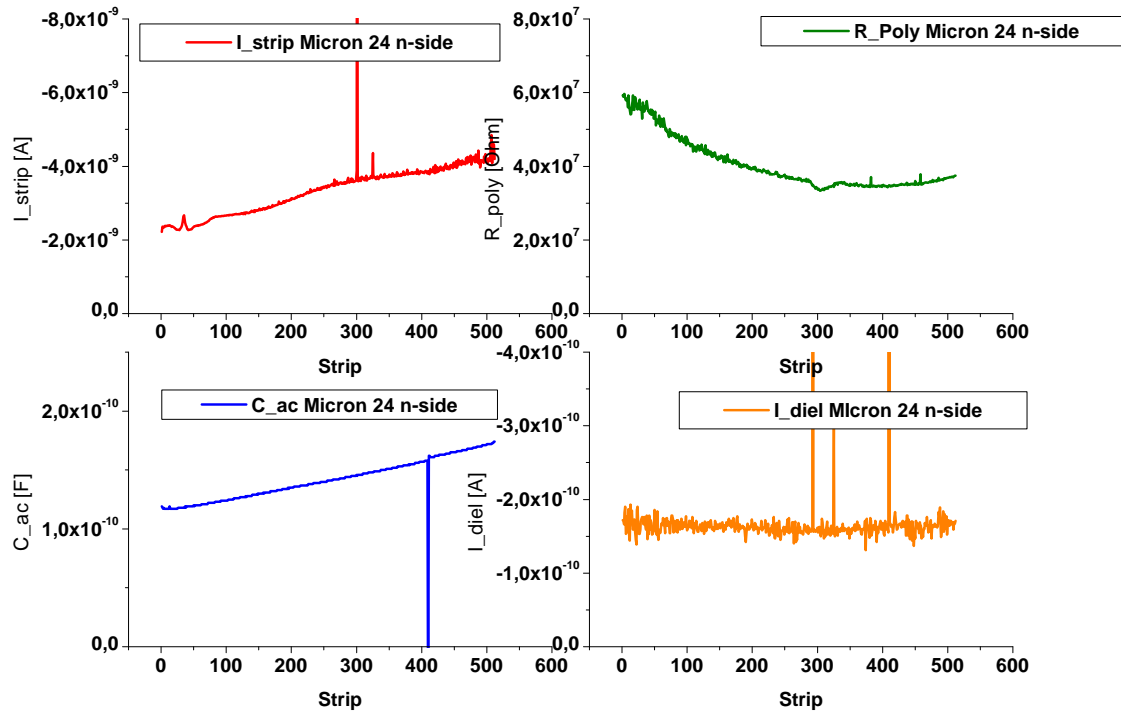


Figure A.31: Stripsan of Micron 24 n-side

A.2. MICRON 1ST BATCH

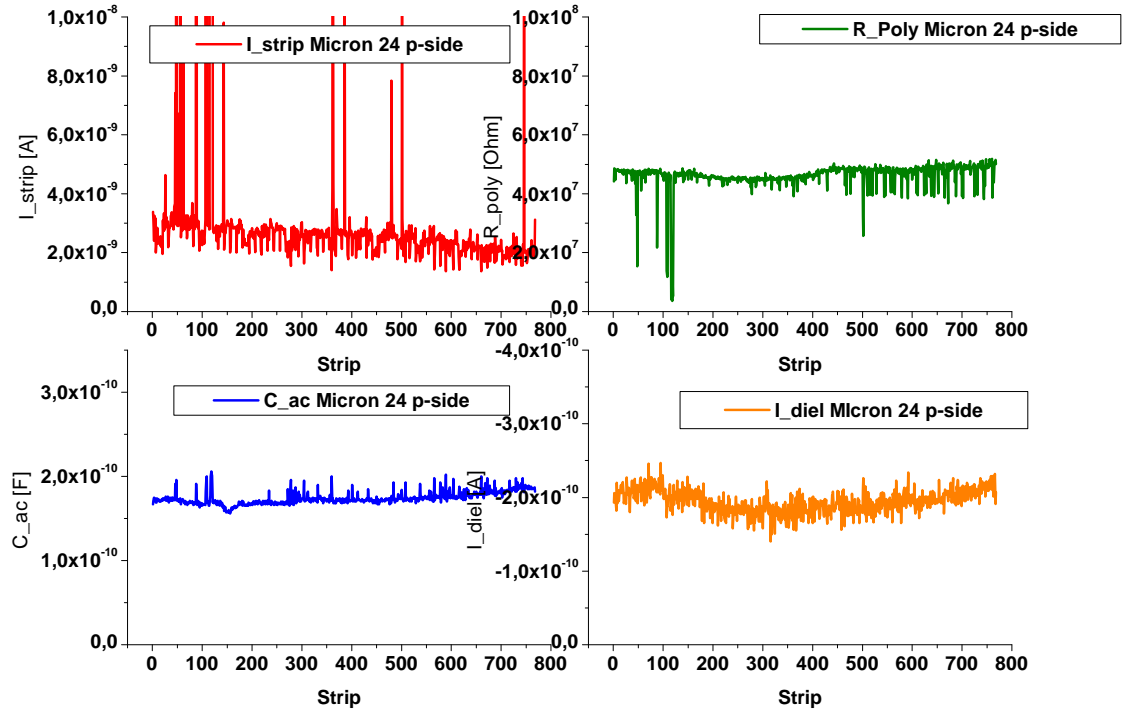


Figure A.32: Stripsan of Micron 24 p-side

# Bibliography

- [1] *Belle II Technical Design Report*
- [2] J. H. Christenson, J. W. Cronin, V. L. Fitch, and R. Turlay†. *Evidence for the  $2\pi$  Decay of the  $K^0$  Meson*, Phys. Rev. Lett. 13, 138–140 (1964)
- [3] Makoto Kobayashi and Toshihide Maskawa. *CP-Violation in the Renormalizable Theory of Weak Interaction*, Prog. Theor. Phys. Vol. 49 No. 2 (1973) pp. 652-657
- [4] G. Lutz. *Semiconductor Radiation Detectors: Device Physics*. Springer, Berlin, 2007. ISBN: 3540716785. 15, 17, 27, 31
- [5] M. Krammer, *VO Grundlagen der Teilchendetektoren* <http://www.hephy.at/lehre/>
- [6] T. Bergauer, *Design, Construction and Commissioning of the CMS Tracker at CERN and Proposed Improvements for Detectors at the Future International Linear Collider*. PhD thesis, TU Wien, 2008.
- [7] European Organisation for Nuclear Research, *Supply of Silicon Micro-Strip Sensors for The CMS Silicon Strip Tracker (SST)*, Nov. 2000
- [8] M. Dragicevic, *The New Silicon Strip Detectors for the CMS Tracker Upgrade*, PhD thesis, TU Wien, 2010.
- [9] S.M. Sze, *Semiconductor Devices*, J. Wiley & Sons, 1985
- [10] M. Friedl, *The CMS Silicon Strip Tracker and Its Electronic Readout*, PhD thesis, TU Wien, 2001
- [11] L. Borrello, A. Messineo, E. Focardi, and A. Macchiolo, *Sensor design for the CMS Silicon Strip Tracker*, CMS Note 2003/020, 2000.
- [12] M. Friedl, *TRHX Temperature and Humidity Measurement System Project*, 2001. <http://www.hephy.at/project/electronic2/ELEC2/index.html>
- [13] *Agilent 4284A Precision LCR Meter Operation Manual*, Japan, January 2000.
- [14] E. Barberis et al., *Capacitances in silicon microstrip detectors*, Nuclear Instruments and Methods in Physics Research A 342 (1994) 90-95
- [15] T.Bergauer et. al, *Resolution studies on silicon strip sensors with fine pitch*, EUDET-Memo-2008-15, <http://www.eudet.org/e26/e28/e615/e782/EUDET-Memo-2008-15.pdf>